VORTEX CONFIGURATIONS OF BOSONS IN ROTATING OPTICAL LATTICES

A Dissertation

Presented to the Faculty of the Graduate School

of Cornell University

in Partial Fulfillment of the Requirements for the Degree of

Doctor of Philosophy

by

Daniel Simon Goldbaum

January 2009

VORTEX CONFIGURATIONS OF BOSONS IN ROTATING OPTICAL LATTICES

Daniel Simon Goldbaum, Ph.D.

Cornell University 2009

Atomic clouds in a rotating optical lattice are at the intellectual intersection of several major paradigms of condensed matter physics. An optical lattice simulates the periodic potential ubiquitous in solid state physics, while rotation probes the superfluid character of these cold atomic gases by driving the formation of quantized vortices. Here we explore the theory of vortices in an optical lattice.

We first provide a detailed introduction section aimed at providing the reader with the information necessary to understand and appreciate the research presented in later chapters.

Next we study an infinite square lattice configuration of vortices in a rotating optical lattice near the superfluid–Mott-insulator transition. We find a series of abrupt structural phase transitions where vortices are pinned with their cores only on plaquettes or only on sites. We discuss connections between these vortex structures and the Hofstadter-butterfly spectrum of free particles on a rotating lattice.

We then investigate vortex configurations within a harmonically trapped Bose-Einstein condensate in a rotating optical lattice. We find that proximity to the Mott insulating state dramatically affects the vortex structures. To illustrate we give examples in which the vortices: (i) all sit at a fixed distance from the center of the trap, forming a ring, or (ii) coalesce at the center of the trap,

forming a giant vortex. We model time-of-flight expansion to demonstrate the experimental observability of our predictions.

Finally for a trapped gas far from the Mott regime, the competition between vortex-vortex interactions and pinning to the optical lattice results in a complicated energy landscape, which leads to hysteretic evolution. The qualitative structure of the vortex configurations depends on the commensurability between the vortex density and the site density – with regular lattices when these are commensurate, and concentric rings when they are not. Again we model the imaging of these structures by calculating time-of-flight column densities. As in the absence of the optical lattice, the vortices are much more easily observed in a time-of-flight image than *in-situ*.

BIOGRAPHICAL SKETCH

Daniel Simon (Dan) Goldbaum was born on June 14, 1978 at Grant Hospital in Columbus, Ohio. He first remembers living in a big white house on the corner of East Dunedin and Fredonia in the city's Clintonville neighborhood.

Dan remembers attending Berwick Alternative Elementary School, after being selected through a registration lottery. The curriculum at Berwick emphasized science, mathematics and computers. Dan can vividly remember a project where he was to chart star positions over the course of a few weeks. The night before the project was due, Dan was terrified because he realized that he hadn't done much star charting, but was relieved to find that his Dad, Don Goldbaum, had been charting all along, while they watched the cosmos together. Another fond memory was participation in the science fair at Berwick. For first grade, Dan and Dad made a display on optical illusions – Did you know that Abraham Lincoln's famous hat was as wide as it was tall? In second grade, Dan and Dad presented what is still considered *the* authoritative poster board display on Owls. Somewhere during that time Dan's family acquired their first home computer. (Thank you, Grandma and Grandpa Greenstone!) Dan put that Apple IIc to good use through the end of high school.

During this time Dan got a baby brother, Jay. On the day Jay was born, Dan refused to leave the public library and had to be carried out by a male librarian. On Jay's 2nd birthday, Dan thought it would be a good idea to put Jay in the bottom drawer of a dresser, and of course, the dresser tipped over and a television landed on Jay. But he was okay; Jay was a tough little guy! Years later Dan apologized to Jay for torturing him so much during childhood, but Jay merely shrugged it off by saying that other younger brothers had it much worse. However, Jay did mention thinking it was pretty funny that he stuck

a compass into Dan's hand when Dan was once, as he said, "raging at him." Despite all this tough brotherly love, or perhaps *because* of it, Jay has grown up to be a real *mensch*, and Dan looks forward to being the best man at his wedding on May 23, 2009.

Back in the summer of 1986, Dan's parents, Don and Abby Goldbaum, planned a move to the nearby suburb of Worthington. This was really only a few miles from their home in Clintonville, but for an eight-year old boy it meant a new school and a new neighborhood, and seemed rather like moving to Mars! But Dan's parents did not realize that he had hatched an ingenious plan to halt the move! However, when moving day came, Dan was distracted by toys, sugary snacks and huge trucks, and he forgot all about forming his body into an unbreakable seal around the metal railing in front of the old house.

Fortunately, the new house had a basketball hoop in the driveway, so new friends were not hard to come by. Among those new friends were Vic and Paul Reehal, who lived across the street. Vic and Paul were both ahead of Dan in school, Vic by three years and Paul five years. So in addition to becoming fast friends, Dan looked up to the Reehal boys, and emulated many of their traits, which was a good thing. Vic and Paul were outstanding students and athletes and stayed away from trouble. Also, their love for soccer made a big impression on Dan, and that game has become one of his life's passions. Dan, Vic and Paul remain close friends.

Dan graduated from Thomas Worthington High School in 1996. In his senior year there he began to develop his love for physics. His plan to become a professional soccer player was not panning out, and he needed something else exciting to pursue. Dan had always excelled at science and mathematics in school, but never really explored taking things further. He could have taken

advanced placement physics in his junior year, but that sounded difficult and stressful, so he took something easier, and then only took physics (and not the advanced placement kind) in his senior year. This physics course, taught by Mr. Guitry, required a book report (due before the Winter Break), and at this point Dan's Mom suggested a book that would have a lasting impact. Dan read and wrote a report on *Genius*, a biography of Richard Feynman by James Gleick. The way that Feynman took such pleasure in his science, and the creative way he went about his investigations inspired Dan to try physics in college.

In August 1996, Dan attended Ohio Wesleyan University on a full-tuition Presidential Scholarship, and an F. Sherwood Rowland and Hall Research Prize from the Chemistry Department. At first, the physics and math courses were very difficult for him. He found himself competing against students who had done "A-levels" or "I.B.," and initially they knew a lot more than he did. But he stuck with it, and eventually came up to speed.

A significant turning point in Dan's career at Ohio Wesleyan was taking his first course in quantum mechanics, taught Fall Semester 1998 by Professor Brad Trees. For Dan, taking this course felt like waking up one morning to a find a new and beautiful world. Quantum mechanics seemed to be the perfect synthesis of mathematics and science, where unexpected results were often the norm. Dan liked it so much that he continued to study quantum mechanics during the Winter Break. (His friends still tease him for bringing his quantum mechanics book to an all-night New Year's Eve party.) In the spring he undertook an independent study of quantum mechanics with Dr. Trees. The next year, again under the direction of Dr. Trees, he completed an honors project in physics titled "Elements of Many-body Theory: A Calculation of Nuclear Spin-Lattice Relaxation Rate in a Metal."

In May 2000, Dan graduated Summa Cum Laude from Ohio Wesleyan, with majors in physics and mathematics, and a minor in chemistry. After graduation, he accepted a Fowler Fellowship to begin graduate study in physics at The Ohio State University. He stayed there for one enjoyable year in the group of Professor John Wilkins. Dr. Wilkins was a very supportive supervisor, and, among other things, he helped Dan win a three-year graduate fellowship from the United States Department of Defense (DoD). Armed with a fellowship that could be used at any school, Dan decided to see what life was like at a traditional physics "powerhouse," so he transferred into the Ph.D. program at Cornell University. This move would not have been possible without the DoD fellowship gained with the help of Dr. Wilkins, who has always been very gracious to Dan even though Dan bolted with the fellowship money acquired under his tutelage!

Life at Cornell was very difficult at first. For the first time Dan was living farther than 30 miles from his birthplace, and Ithaca did not seem to have a lot in common with suburban Columbus. When Dan first moved to Ithaca there were no Starbucks, Borders, Barnes and Noble, Best Buy, Walmart, and so forth. Things closed earlier. It was darker and colder, and the buildings were shorter. Dan can recall one Sunday early on, when his parents had arrived in Ithaca with items from home. They needed a certain size nut and bolt to connect his bed and its headboard. He remembers having to drive around central New York for a long time before acquiring these items. At that point Ithaca seemed very small and desolate! However, things eventually improved. Being so far away from home, Dan had to learn to organize his life and take care of himself. And along the way Dan grew quite fond of the natural beauty and unique flavor of life in Ithaca.

On the physics side of life, Dan found that he was most interested in quan-

tum theory applied to many-body systems, but was having trouble fitting in with any of the existing research groups in Cornell's Condensed Matter Theory Department. He found himself spending a lot of time on the Internet looking at the work of different physics groups outside Cornell. He eventually landed on the home page of Erich Mueller, who was then a postdoctoral research associate with Jason Ho at The Ohio State University. Dan was dazzled by Erich's research, and remembers thinking, "I wish I could work with THIS guy!" Dan noticed that Erich was scheduled to give a seminar at Cornell. Dan emailed Erich and asked if they could meet at Cornell and if Erich could suggest some reading to help him get started in the field of ultracold atoms. Upon meeting, Erich presented Dan with a very nice handwritten bibliography on cold atoms, which Dan still has.

It turned out that Erich was at Cornell interviewing for a faculty position. As an assistant professor in August 2003, he hired Dan to be his first thesis student. On November 4, 2008, Dan successfully defended his Ph.D. thesis. This date will forever be remembered as the day when the United States elected its first black president, Barack Obama. Dan will never forget that day. Dan realizes that his personal accomplishment was so very small compared to the step forward taken by the United States of America. However, he cannot help but see parallels between those events, and the feelings that they inspired in him – most strikingly, the feeling of accomplishing a goal that seemed distant and improbable, and then waking up the next morning, not having fully digested what happened the day before, but realizing that the world seemed new and full of exciting possibilities.

After graduation Dan will be a postdoctoral research associate in the group of Professor Pierre Meystre at The University of Arizona.

This thesis is dedicated to my Mom and Dad. Without their help and support I would have never made it through graduate school. Their humor, understanding, patience, and love is my most valuable resource.

ACKNOWLEDGEMENTS

First and most importantly, I must acknowledge the help and support of my parents, Don and Abby Goldbaum. My Mother and Father are both extraordinary people, and they have always enthusiastically supported my interest in physics. Whenever I was upset, I could always count on them for patient sympathy, robust encouragement, and carefully thought out advice. And at all times they made sure I knew that they loved me and were proud of me. Perhaps it is impossible for me to ever express proper thanks for all they have done for me, but I hope that I can honor them by emulating their example of kindness, understanding and good humor, and by passing this example on to my children.

I would also like to thank my Brother, Jay Goldbaum. When I began graduate school, he was beginning college. Now he is an attorney, working at a prominent Detroit law firm, and preparing to marry his wonderful fiance, Kristen! Although we have often been separated by many miles, we have grown much closer through frequent phone calls and visits. He has always lent an understanding ear when I needed it. In many ways, he knows me better than anyone and is my best friend. Furthermore, I am very proud of all his achievements and his development as a person during this time.

I have been profoundly influenced by many great teachers at all levels of schooling. I give special thanks to Professor Brad Trees at Ohio Wesleyan University. Professor Trees supervised my departmental honors thesis, which consisted of an entire year of work together: learning the basics of quantum many-body theory, performing a calculation, and then writing a thesis. In addition, he supervised my independent study in quantum mechanics, when no second course was offered. Furthermore, during this independent study I completed almost all the problems in the second half of Griffiths' quantum mechanics text,

and Professor Trees carefully marked them all!

I also thank Professor John Wilkins at The Ohio State University. After graduating from Ohio Wesleyan, I spent one year in the graduate program at Ohio State. Professor Wilkins welcomed me into his group, and provided all sorts of useful advice and support. He supported my successful application for a Department of Defense fellowship. Then, when I decided to leave Ohio State (and take that fellowship with me), he was very kind in helping me gain admission to Cornell.

A large factor in the success of any graduate student career is the thesis advisor. I was fortunate to do my graduate work under the supervision of Professor Erich Mueller. He has been very patient and helpful throughout our time together. So many times we have sat for hours discussing physics, or working on manuscripts together. Those are priceless learning experiences that not every graduate student is fortunate enough to have.

Besides my thesis advisor, Professor Veit Elser has been by far the most influential faculty member during my graduate career. I always felt comfortable entrusting Veit with any question or concern. His patient friendship and experienced mentorship were invaluable to me. Veit also welcomed me as something of a surrogate member of his group, and on numerous occasions I enjoyed tasty cookouts at his home.

It would be impossible to properly thank all of my classmates who have helped me out along the path to the Ph.D., but I will try. I thank (in no particular order): Andreja Cobeljic, Jim van Howe, Jay Hubisz, Kristen (Lantz) Reichenbach, Ben Shlaer, Louis Leblond, Ferdinand Kuemmeth, Arne Kirchheim, Pierre Thibault, Kaden Hazzard, Sophie Rittner, Vassiliki Kanellopolous, Stefan Baur, Sourish Basu, Carlos-Ruiz Vargas, Tudor Marian, Stefan Natu, Bryan Daniels,

Pete Zweber, Matt van Adelsberg, Isaac Rabinowitz, Jack Sankey, Nadia Adam, Kiran Thadani, Sufei Shi, Ethan Bernard, Andrew Fefferman, Tchefor Ndukum, Johannes Lischner, Duane Loh, Niranjan Nagaranjan, Tibi Tomitsa, Cristina Patron, Radu Murgescu, Sumiran Pujari, David Wacker, Gil Paz, Sammy Rosenblatt, Meisha Morelli, Praveen Gowtham, Steve Hicks, Joern Kupferschmidt, Shaffique Adam, Stefan Braig, Radu Rugina (former professor), and Johannes Heinonen. Cornell, because of its world class reputation for academics and because of the compact nature of the Ithaca community, is a great place to meet people of different backgrounds and personalities. I feel that this aspect really helped me to grow as a person. I am so grateful to have met you all! If there is anyone I missed...sorry, I need to finish this document!

Special mention goes to Jack Sankey, who became my best friend forever (BFF) during our last few years together at Cornell. I often stopped by his office for a snack and some irreverent conversation to clear my brain before getting back to physics. Also, we had a lot of great nights hanging out, watching movies, playing video games, and generally fooling around and having a good time. Hey Jack, it's time you knew the truth....I AM JOUST WILLIAMS. Blue fire! Red fire! Blue Fire! Red Fire!

Another special person in my life is Tory Browers. We met on New Year's eve in 2006, and we have been together ever since. Tory is so wonderful. She is beautiful, kind, talented, fun, tough, determined, and many other positive things. I have never had such a kind and understanding relationship with a woman. I am blessed to have met her, and blessed that she has chosen to brighten and enrich my life for almost two years now!

I should also mention that in my last couple of years I developed a close relationship with Kaden Hazzard (also BFF). I am very grateful to Kaden for

always being eager to listen to my physics problems, and for often providing useful insights. More importantly, Kaden is also from central Ohio, and is thus a huge Buckeye fan, like me ("O-H!!!"). We had a lot of fun watching those games on fall Saturdays ("I-O!!!"), but not quite as much fun watching them in January. (But second place ain't bad!) In any case, I think that Kaden will make it in physics if he doesn't die of cholera or the plague due to living in his apartment.

Also, between Kaden, Stefan Baur and I, we spent many hours doing physics, eating the best cuisine that Collegetown had to offer, and insulting each other's Mothers (all in good fun). Once, a week or so after Kaden's parent's house had burned down, Kaden was giving Stefan an awful lot of grief. Stefan eventually had had enough, and then reminded Kaden that "at least my Mother lives in a house that is not burned down!!" (After this insult I gave Stefan a five minute standing ovation, and the next day presented him with a plaque commemorating the occasion. Thinking back, that ceremony was the only time during graduate school when I wore a suit.)

A big part of my recreation during grad school was based around playing soccer. There are so many people that deserve thanks for the wonderful experiences I had in the Ithaca soccer community. I cannot possibly do justice to all the great friends I have made through playing soccer there – good luck and thank you all! In particular I want to thank Martin Wiedmann for organizing the "Biradicals" coed soccer team, and inviting me to play. The Biradicals were always a fun team made up of a lot of nice people and good soccer players, and we had many enjoyable games at Cass Park, Union Field, and The Field. Perhaps the biggest soccer thanks should go out to Rich Parker, Jano Para and Ibe Ibeike-Jonah. (Sorry if I left out someone of equal importance.) Without their

efforts Ithacans would not have had such a great soccer league to play in.

Lastly, I acknowledge my funding sources during my Ph.D. work at Cornell. From August 2001 to August 2004, I was supported by the Department of Defense (DoD) through the National Defense Science and Engineering Graduate Fellowship (NDSEG) Program. From August 2004 to August 2006 I was funded by the "Graduate Assistance in Areas of National Need (GAANN) Progam" (Department of Education, grant number P200A030111), administered through the laboratory of atomic and solid state physics at Cornell. From August 2006 to December 2006 I was supported through funds from the National Science Foundation under grant PHY-0456261. Further support for the work presented in this dissertation was provided by the National Science Foundation through grant No. PHY-0758104.

TABLE OF CONTENTS

LIST OF TABLES

LIST OF FIGURES

CHAPTER 1

OPTICAL LATTICES AND THE BOSE-HUBBARD HAMILTONIAN

1.1 Introduction

Modern atomic trapping and cooling techniques allow unprecedented control over ultracold atomic gases. Using these systems, experimentalists can now investigate a wide variety of many-body systems with properties (such as interaction strength, impurity potential, and geometry) that can be precisely adjusted [1, 2]. Cold atomic systems also show excellent potential for performing precision measurements: for example improved atomic clocks, fine-structure constant measurements, and quantum-limited interferometry [3]. Also, trapped cold-atom systems play a crucial role in several proposed schemes for quantum computation [2, 4], as well as in the analysis of complex materials [2, 5].

I perform a theoretical study of ultracold atomic systems in a regime where deep optical-lattice potentials and rotation produce exotic ground states. Unlike previous theoretical studies of vortex structures in ultracold atomic gases, which are restricted to a weakly-interacting limit (e.g, [6, 7, 8]), I will explore the strongly-interacting regime. Technically, this means that instead of studying the Gross-Pitaevsii equation, I will model the system by a Bose-Hubbard model. This model, based upon a tight-binding approximation, is very accurate, describing both superfluid and insulating phases, and their coexistence [9]. My calculations use a variational approach to numerically solve the Bose-Hubbard model. Unlike most other treatments, I do not make a local-density approximation, and can therefore describe short length-scale structures which will be the dominant feature of experiments.

1.2 Optical Lattices

This dissertation investigates systems of neutral bosonic atoms trapped in rotating optical lattices. The following subsection provides some background information on optical lattice trapping.

1.2.1 Trapping Ultracold Atoms in Optical Lattices

An optical lattice potential is a a periodic array of potential wells generated by interfering laser beams [10]. The most common optical lattice setup consists of counterpropagating laser beams, which, when placed in orthogonal directions, generate 1-, 2- or 3-dimensional periodic potentials with a square-lattice geometry. We focus on this setup. However, different laser configurations may be used to produce optical lattices with a wide variety of geometries [11].

In one spatial dimension the simplest optical lattice is a sinusoidal standing wave pattern created by the interference of two counter-propagating laser beams. The two beams must be phase locked. If the phase difference changes, then the position of the standing wave changes accordingly. The phase locking is typically achieved by using a single laser, and generating the two beams with a mirror or beam splitter. In two dimensions a square lattice is formed by two such (orthogonally directed) standing waves, and a three-dimensional cubic lattice is formed in the same fashion with three standing waves. In the above setup, the lattice spacing d is half the wavelength of the laser light, λ. It will be shown later how this is an important limitation. In order to adjust the lattice spacing without changing λ one can instead engineer a setup where the optical

lattice is produced by interfering laser beams that propagate at a relative angle θ. In this setup the lattice spacing is then given by

$$d = \frac{\lambda}{2\sin(\theta/2)}\,. \tag{1.1}$$

The above description does give a physical picture of the geometry of an optical lattice potential, but leaves us with the important question of how an optical standing wave traps ultracold atoms. I closely follow the treatment of Pethick and Smith ([10], pp. 67-74) in describing this effect.

1.2.2 Interaction of a Neutral Atom with Laser Light

There are two main ways a neutral atom interacts with laser light. One is the shift in atomic energy levels that can be considered semiclassically, using virtual transitions (second-order perturbation theory). The second is radiation pressure due to real transitions that correspond to absorption and emission of a single photon. These real transitions can be accounted for by giving a finite lifetime to the atom's excited states. For the purpose of trapping cold atoms we wish to take advantage of the shift of the atomic ground state, and seek to minimize the effect of real transitions. Next I present some fundamentals of these effects.

First consider the interaction between a neutral atom and a real, time-dependent electric field. In the dipole approximation, where we assume that the wavelength of the radiation is much greater than the atomic scale, the perturbation is given by

$$H' = -\vec{\boldsymbol{d}} \cdot \vec{\mathrm{E}} \tag{1.2}$$

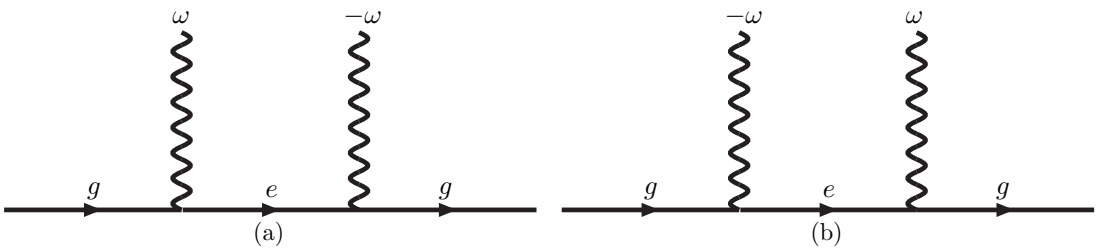

Figure 1.1: **Diagrammatic representation of the AC Stark effect**. Diagrammatic representation of the virtual transitions that cause the ground state energy shift. We add the terms represented by each diagram together to get the total shift. 'e' denotes the excited state, and 'g' denotes the bare ground state. The straight line represents atom propagation and the wavy line represents interaction with the electric field.

where $\vec{\boldsymbol{d}}$ is the atomic dipole moment and $\vec{\mathsf{E}}$ is the electric field defined by

$$\vec{\mathsf{E}} = \hat{\varepsilon}\left(\mathsf{E}_{\omega}\exp\left(-i\omega t\right) + \mathsf{E}_{-\omega}\exp\left(i\omega t\right)\right), \tag{1.3}$$

where $\hat{\varepsilon}$ is the polarization direction, and ω is the angular frequency of the radiation. The $\mathsf{E}_{\omega}\exp\left(-i\omega t\right)$ term represents absorption of a photon of frequency ω, and the $\mathsf{E}_{-\omega}\exp\left(i\omega t\right)$ term represents stimulated emission of a frequency ω photon. And, since the electric field is real, then $\mathsf{E}_{-\omega} = \mathsf{E}_{\omega}^{*}$. We can now write the energy shift of the ground state to second order using diagrammatic perturbation theory as shown in Figure 1.1.

In Figure 1.1(a) the atom begins in its ground state, $|g\rangle$. At the intersection of the straight and wavy line labeled by "ω" the atom absorbs a photon of frequency ω, and makes a transition to an excited state, $|e\rangle$. Next, at the intersection of the the straight line labeled by "e" (we call this the propagator for the excited state), and the wavy line labeled by "$-\omega$" the atom emits a photon of frequency ω and returns to its original ground state. We may translate this diagram into a mathematical expression by associating a factor with each "interaction vertex"

(that is, where the straight and wavy lines meet), and with the propagator for the excited state. In Figure 1.1(a), the interaction vortex for absorption gives $\langle e| - \vec{\boldsymbol{d}} \cdot \vec{\mathsf{E}}_\omega |g\rangle$, the vertex for stimulated emission gives $\langle g| - \vec{\boldsymbol{d}} \cdot \vec{\mathsf{E}}^*_\omega |e\rangle$, and the propagator for excited state gives $(\omega - (E_e - E_g))^{-1}$. Note that E_e is the energy of the unperturbed excited state labeled by the index "e", and E_g is the energy of the unperturbed ground state. Now, using the same translation method, the diagram in Figure 1.1(b) gives a similar term. Adding these terms and summing over all possible excited states we find an expression for the atomic ground state energy shift, ΔE_g,

$$\begin{aligned} \Delta E_g &= \sum_e |\langle e| - \vec{\boldsymbol{d}} \cdot \hat{\varepsilon} |g\rangle|^2 \left(\frac{1}{\hbar\omega - (E_e - E_g)} + \frac{1}{-\hbar\omega - (E_e - E_g)} \right) |\mathsf{E}_\omega|^2 \\ &= -\frac{1}{2} \alpha(\omega) \langle \mathsf{E}^2(\mathbf{r}, t) \rangle_t \,, \end{aligned} \tag{1.4}$$

where we have introduced the dynamic atomic polarizability, $\alpha(\omega)$, and $\langle \mathsf{E}^2(\mathbf{r}, t) \rangle_t = 2|\mathsf{E}_\omega|^2$ is a time average. We can then identify the atomic polarizability as

$$\alpha(\omega) = \sum_e \frac{2(E_e - E_g) |\langle e| \vec{\boldsymbol{d}} \cdot \hat{\varepsilon} |g\rangle|^2}{(E_e - E_g)^2 - (\hbar\omega)^2} \,. \tag{1.5}$$

Now, by considering the atomic length and energy scales ($\sim$ bohr radius, eV) we see that each term in $\alpha(\omega)$ is very small unless ω is very close to a transition frequency, $\omega_{eg} = (E_e - E_g)/\hbar$. So if we work close to some ω_{eg} then the corresponding term in the sum for $\alpha(\omega)$ dominates all other terms in the sum, and we make the approximation

$$\alpha(\omega) \approx \frac{|\langle e| \vec{\boldsymbol{d}} \cdot \hat{\varepsilon} |g\rangle|^2}{E_e - E_g - \hbar\omega} \,. \tag{1.6}$$

The above polarizability accounts for the shift in atomic ground state energy due to virtual transitions, but does not account for the radiation pressure on the atom from real transitions due to spontaneous emission of excited states. This is

because we started with a classical radiation field, and spontaneous emission is a purely quantum phenomenon. Effectively we take this into account by letting the excited state energy be complex, which can be explained by considering the standard time-dependent amplitude oscillation of a quantum mechanical stationary state, that is, $\exp(-iE_e t/\hbar)$. For spontaneous emission to occur the excited state must have a finite lifetime, that is, the state's amplitude must decay over time. It follows that E_e must have an imaginary part. If we label the lifetime of the state $1/\Gamma_e$, then

$$E_e \rightarrow E_e - i\frac{\hbar\Gamma_e}{2}\,, \tag{1.7}$$

where E_e is now the real part of the excited state energy. By substituting equation (1.7) into equation (1.6) we find that the ground state energy perturbation is now complex as well, that is,

$$\Delta E_g = V_g - i\frac{\hbar\Gamma_g}{2}\,, \tag{1.8}$$

where

$$V_g = -\frac{1}{2}Re\{\alpha(\omega)\}\langle \mathsf{E}^2(\mathbf{r},t)\rangle_t \tag{1.9}$$

is now called the "energy shift", and

$$\Gamma_g = -\frac{1}{\hbar}Im\{\alpha(\omega)\}\langle \mathsf{E}^2(\mathbf{r},t)\rangle_t \tag{1.10}$$

is the lifetime of the "dressed" ground state.

We now investigate the implications of this shift for trapping. First we define the "detuning", δ, which is the difference between the laser frequency and the atomic transition frequency, defined by

$$\delta = \omega - \omega_{eg}\,, \tag{1.11}$$

where we recall that ω_{eg} is the transition frequency,

$$\omega_{eg} = \frac{(E_e - E_g)}{\hbar}\,. \tag{1.12}$$

Conventionally, a positive value of δ is called "blue detuning" and a negative value of δ is "red detuning". Next we define the Rabi Frequency, Ω_R, which is just the magnitude of the Stark effect matrix element expressed in terms of frequency

$$\Omega_R = \frac{|\langle e|\vec{\boldsymbol{d}} \cdot \hat{\varepsilon}|g\rangle|}{\hbar} . \tag{1.13}$$

Using equations (1.11), (1.12) and (1.13) we may rewrite the ground state energy shift, V_g,

$$V_g = \frac{\hbar\,\delta\,\Omega_R^2}{\delta^2 + (\Gamma_e/2)^2} . \tag{1.14}$$

Equation (1.14) tells us about the force on the atoms due to the shifting of the atomic ground state energy by virtual transitions. We see that if the laser is blue-detuned then the atomic ground state energy is shifted to a higher value, and the atoms will move toward regions of lower field. However, if the laser field is red-detuned then the atoms move toward regions of higher field.

In addition, we must consider the force on the atom from radiation pressure due to spontaneous emission. But this force should only be important if Γ_e is larger than or comparable to the magnitude of the detuning, $|\delta|$. That is, the transition probability is a Lorentzian distribution of width Γ_e, centered at ω_{eg}, so if the detuning is much larger than Γ_e, then probabilty of a real transition occuring will be very, very small. In practice [12], the optical lattice is create using a blue detuned laser, far enough from the atomic resonance so that only the force due to virtual transitions is important in trapping the atoms, and the atoms occupy the minima of the standing wave that makes up the optical lattice. The reason for this convention is that the standing wave minima are also photon density minima, so the cross-section for atom-photon interactions is minimized there as well. Generally we want to minimize loss mechanisms such as atom-photon scattering.

The resulting potential is most generally written

$$V(x,y,z) = V_{0,x}\sin^2\left(\frac{\pi x}{d_x}\right) + V_{0,y}\sin^2\left(\frac{\pi y}{d_y}\right) + V_{0,z}\sin^2\left(\frac{\pi z}{d_z}\right), \tag{1.15}$$

where $\{x, y, x\}$ are orthogonal Cartesian coordinates, while $\{V_{0,x}, V_{0,y}, V_{0,z}\}$ and $\{d_x, d_y, d_z\}$ are the corresponding lattice depths and lattice constants, respectively. Equation (1.15) represents a three dimensional lattice of potential wells, where the parameters are often controllably adjustable in experiment, although, in practice, problems related to phase matching are always of concern. As noted before, we can now clearly see why the ability to independently adjust d and λ is important. That is, we can adjust the lattice spacing, d, without changing the magnitude, sign, and stability of the optical trapping potential, which depend on λ.

In experiment, constructing an asymmetric optical lattice introduces more challenges to producing a viable trap. However, there have been some notable successes. For instance, the dimensionality of the optical lattice can be reduced by increasing V_0 along a single axis so that atomic motion is restricted in that direction. We then have a two-dimensional optical lattice system. This procedure has been realized by several groups, including the NIST Gaithersburg team [13], and is particularly important here because it is an experimental realization of the trap geometry studied theoretically in this dissertation.

1.3 From Optical Lattice Trapping to the Bose-Hubbard Model

In their letter from October 12, 1998 Jaksch et. al. [9] proposed that a dilute gas of ultracold bosons loaded onto an optical lattice could be well described by

a Bose-Hubbard model (BHM). Furthermore, they showed the relationship between the model's parameters and the microscopics of the underlying system, as well as demonstrating how these parameters of the BHM could be controllably varied in experiments. They describe the creation of square-lattice geometries where $d = \lambda/2$. We follow their argument to show how the effective BHM arises from the more general continuum description.

We begin by stating the continuum Hamiltonian operator for our system,

$$\begin{aligned} \hat{H} &= \int d^3\vec{x}\, \hat{\psi}^\dagger(\vec{x}) \left(-\frac{\hbar^2}{2m}\vec{\nabla}^2 + V_O(\vec{x}) + V_T(\vec{x}) \right) \hat{\psi}(\vec{x}) \\ &+ \frac{1}{2}\frac{4\pi a_s \hbar^2}{m} \int d^3\vec{x}\, \hat{\psi}^\dagger(\vec{x})\, \hat{\psi}^\dagger(\vec{x})\, \hat{\psi}(\vec{x})\, \hat{\psi}(\vec{x}) \ , \end{aligned} \tag{1.16}$$

where $\hat{\psi}(\vec{x})$ is a bosonic field operator, $V_O(\vec{x})$ is the optical lattice potential, and $V_T(\vec{x})$ is a slowly varying external trapping potential. Also, m is the mass of a single boson, and a_s is the boson-boson s-wave scattering length. Note that we have *a priori* made the pseudopotential approximation, so that the interatomic interaction is a delta function proportional to a_s. Going forward, the basic program is to formulate a tight-binding approximation to the Hamiltonian. This will yield an effective hopping model, a Bose-Hubbard Model, to describe the boson dynamics.

The *tight-binding* approximation is often used to described the low-energy electron bands in a solid ([14], pp. 176-189), and the logic is as follows. First we consider the solid to be a lattice of isolated atoms whose electrons occupy orbitals well localized at their lattice position. Real materials, however, are many-body systems where electrons centered at a particular atomic nucleus will interact with electrons centered at other atomic nuclei. To model this we must suitably modify our description consisting of isolated atoms. The first correction to the isolated-atoms picture is to additionally consider the overlap between

orbitals on neighboring sites, the *nearest-neighbor* approximation. Analogously, we consider bosons trapped in a periodic potential described by equation (1.15). The periodic potential induces a band structure for our bosons, but the energy scale of the boson dynamics is small enough so that we may confine our argument to the lowest energy band, that is, each boson occupies the ground vibrational state of a potential well, and thus we expect that the corresponding wavefunctions are well localized about the minimum of their respective wells. As a first correction to the picture of bosons isolated in a potential well, we consider the mixing of vibrational states in neighboring wells.

Following this approach, one expects to find a Bose-Hubbard Hamiltonian:

$$\hat{H} = -\sum_{\langle i,j \rangle} \left(t_{ij}\, \hat{a}_i^\dagger \hat{a}_j + h.c. \right) + \frac{U}{2} \sum_i \hat{n}_i \left(\hat{n}_i - 1 \right) - \sum_i \mu_i \hat{n}_i \,, \tag{1.17}$$

where $\langle i, j \rangle$ denotes the sum over pairs of nearest-neighbor sites. To clarify what terms are included, we can think of each term as a bond connecting nearest-neighbor sites, and the sum is over all distinct bonds. Also, t_{ij} is the tunneling (or "hopping") matrix element for an atom tunneling from site j to site i, *h.c.* refers to "hermitian conjugate", $\hat{a}_i^\dagger$ ($\hat{a}_j$) is the bosonic creation (annihilation) operator for site i (j), U is the pair interaction energy for two atoms sharing the same site, $\sum_i$ is the sum over all sites i, $\hat{n}_i = \hat{a}_i^\dagger \hat{a}_i$ is the number operator for site i, and μ_i is the local chemical potential at site i. Qualitatively, the first term on the right-hand side of equation (1.17) is the contribution to the total energy due to delocalization of the system by tunneling. The second term is the sum of the on-site pair-interaction energies, and the third term is the potential energy offset commonly due to an external trapping potential in addition to the optical lattice. Equation (1.17) will be the starting point for the calculations performed in this dissertation. We now show how to derive the parameters in this approximate

Hamiltonian.

Quantitatively, we do this by expressing our bosonic field operators in terms of tightly-peaked Wannier functions, $w(\mathbf{x})$, that is,

$$\hat{\psi}(\vec{x}) = \sum_j \hat{a}_j \, w\left(\vec{x} - \vec{x}_j\right) \tag{1.18}$$

where the sum runs over each lattice site, and $\hat{a}_j$ is a bosonic annihilation operator for site j. The form of $w(x)$ will be discussed shortly. Then we substitute equation (1.18) into equation (1.16). This gives the parameters in equation (1.17) in terms of the Wannier wavefunctions.

First we consider the interaction term from equation (1.16). Using equation (1.18) we have

$$\begin{aligned} &\int d^3\vec{x}\, \hat{\psi}^\dagger(\vec{x})\, \hat{\psi}^\dagger(\vec{x})\, \hat{\psi}(\vec{x})\, \hat{\psi}(\vec{x}) = \\ &\sum_{i,j,k,l} \hat{a}_i^\dagger \hat{a}_j^\dagger \hat{a}_k \hat{a}_l \int d^3\vec{x}\, w^*(\vec{x} - \vec{x}_i)\, w^*\left(\vec{x} - \vec{x}_j\right) w(\vec{x} - \vec{x}_k)\, w(\vec{x} - \vec{x}_l) \; . \end{aligned} \tag{1.19}$$

Now since the Wannier functions are so well localized, the dominant term is when the site indices are all equal, that is, on-site interactions. It has been shown that in most circumstances the next greatest term, the nearest-neighbor repulsion, is about two orders of magnitude smaller, and is thus omitted from the effective Hamiltonian [9]. We can then make the identification

$$U = \frac{4\pi a_s \hbar^2}{m} \int d^3\vec{x}\, |w(\vec{x} - \vec{x}_i)|^4 \, . \tag{1.20}$$

Next we consider the trapping potential term. Since the trapping potential, $V_T(\vec{x})$, is so slowly varying on the scale of the optical potential, we may perform this integral as if there is only a static background to the Wannier functions. Again, because the Wannier functions are very localized, the on-site term

is dominant and the overlap terms may be truncated. We are then left with

$$\int d^3\vec{x}\,\hat{\psi}^\dagger(\vec{x})\,V_T(\vec{x})\,\hat{\psi}(\vec{x}) \approx \sum_i \hat{n}_i \int d^3\vec{x}\,V_T(\vec{x})\,|w(\vec{x}-\vec{x}_i)\,|^2\,, \tag{1.21}$$

and we identify the integral as

$$\epsilon_i = \int d^3\vec{x}\,V_T(\vec{x})\,|w(\vec{x}-\vec{x}_i)|^2 \approx V_T(\vec{x}_i)\;, \tag{1.22}$$

which is the energy offset at lattice site i due to the external potential. In addition, since we deal with the grand-canonical ensemble, we define the chemical potential μ and write the *full* Hamiltonian, $\hat{H}_{\text{Full}} = \hat{H} - \mu \sum_i \hat{n}_i$. From now on we drop the subscripts from $\hat{H}$ and, unless otherwise stated, always work with the full Hamiltonian. The chemical potential term follows directly from the argument leading to ϵ_i. Since both parameters multiply the number operator, it is convenient to define a local chemical potential for each site,

$$\mu_i = \mu - \epsilon_i\,. \tag{1.23}$$

Lastly, we analyze the term including the kinetic and optical lattice potential energies,

$$\int d^3\vec{x}\,\hat{\psi}^\dagger(\vec{x})\,\hat{K}(\vec{x})\,\hat{\psi}(\vec{x}) = \sum_{i,j} \hat{a}_i^\dagger \hat{a}_j \int d^3\vec{x}\,w^*(\vec{x}-\vec{x}_i)\,\hat{K}(\vec{x})\,w\Big(\vec{x}-\vec{x}_j\Big)\,, \tag{1.24}$$

where $\hat{K}(\vec{x}) = \Big(-\frac{\hbar^2}{2m}\vec{\boldsymbol{\nabla}}^2 + V_0\,(\vec{x})\Big)$, and the sum is over all sites of the optical lattice. First consider just the on-site term, where $i = j$. We find that this integral is approximately the ground state energy of a single boson in a potential well. This energy is the same for each boson in the system, so the total energy contribution is constant for a constant number of bosons, and the energy contribution connected to number fluctuations is already accounted for by the chemical potential. Thus we can truncated this term without changing the physics of our

effective model. Note that this is the "isolated boson" energy term in our tight binding approximation. The first correction to the isolated boson energy is then found by considering nearest-neighbor mixing. The next-nearest neighbor term is characteristically two orders of magnitude smaller than the nearest-neighbor term, so we omit it from our effective model, and thus make the identification

$$t_{ij} = -\int d^3\vec{x}\, w^*(\vec{x} - \vec{x}_i)\, \hat{K}(\vec{x})\, w\left(\vec{x} - \vec{x}_j\right) , \tag{1.25}$$

where $\{i, j\}$ denote nearest neighbor sites. The above sign convention is fixed so that all the effective parameters in the BHM will be non-negative in the case of a uniform system. It appears as though there is a minus sign missing from the definition of the tunneling amplitude in Jaksch et. al. [9].

The only remaining step is to calculate the Wannier states. Generically, this must be done numerically. We first comment on the qualitative effects of tuning the laser intensity in an experiment. Recall that the optical-trap depth, V_0, is proportional to the intensity of the laser field, so the experimentalist may control the trap depth. If we increase the trap depth, then each boson should become more localized in its respective potential well. Thus there should be more overlap of bosons occupying the same well so the magnitude of U should increase, and tunneling should become more difficult, so the magnitude of t_{ij} should decrease. As a result the potential term becomes dominant in determining the ground state, and at a certain well depth we expect a phase transition to a state with "commensurate filling of the lattice" [9], that is, a Mott Insulator (MI). In the opposite limit the tunneling of bosons should dominate the form of the ground state, and we expect that in this limit the ground state is highly delocalized and phase coherent, that is, a superfluid (SF).

The qualitative insights made above are supported in experiment [12] and

by highly-accurate numerical calculations [15]. We can also write a corresponding analytic theory by approximating the region in the minimum of the well to be a harmonic oscillator potential, where each boson is then in a harmonic oscillator ground state. In this way we will get a sense of how the BHM parameters should scale with respect to the experimental parameters. First we determine the three harmonic oscillator angular frequencies (one for each spatial direction, using separation of variables in Cartesian coordinates). We do this by taking the second derivative of the optical lattice potential (see equation (1.15)) and finding the value at the minimum of the well ($x = 0$ or $y = 0$ or $z = 0$) and setting it equal to the standard form of the harmonic oscillator potential, $\hat{V}_{HO} = \frac{1}{2}m\omega^2 x^2$, where m is the boson mass and ω is the angular frequency. We find that

$$\omega_i = \frac{\sqrt{4E_R V_{0,i}}}{\hbar}, \tag{1.26}$$

where the index i denotes spatial direction, and $E_R (= \hbar^2 k^2/(2m))$ is the recoil energy, where k is the laser wavenumber. We can then estimate the size of a single-boson wavefunction by the corresponding oscillator length $\ell_i (= \sqrt{\hbar/(m\omega_i)})$, and now we have a context in which to present the self-consistency conditions for the Bose-Hubbard model [9].

For our analysis to make sense we need $a_s \ll \ell \ll d$, where $\ell \ll d$ is the condition for the tight-binding approximation. The condition $a_s \ll \ell$ is required for interactions to not excite atoms into higher bands. This is equivalent to setting $\Delta E_j = \frac{1}{2}Un_j(n_j - 1) \ll \hbar\omega$, where the subscript j denotes a lattice site. In practice these inequalities are easily satisfied [9].

Next, we use 3-D harmonic-oscillator ground state wavefunctions for a spherically symmetric potential to calculate analytic estimates for t and U for

a cubic optical lattice. The wavefunction is ([16], pp. 31-44),

$$\psi_{HO}(r) = \frac{1}{\pi^{3/4}\ell^{3/2}} \exp\left(-\frac{r^2}{2\ell^2}\right), \tag{1.27}$$

where ℓ is the oscillator length, and ω is the corresponding angular frequency. Next, by substituting equation (1.27) into equation (1.20), we find

$$U = \sqrt{\frac{2}{\pi}}\hbar\omega\left(\frac{a_s}{\ell}\right), \tag{1.28}$$

which tells us that the interaction parameter, U, scales as $(k^2V_0)^{3/4}$. For the uniform case, we estimate t by calculating the integral,

$$t \sim \int d^3\vec{\mathbf{x}}\,\psi^*_{HO}\left(\mathbf{x} - \frac{\lambda}{2}\right)\left[-\frac{\hbar^2}{2m}\vec{\nabla}^2\right]\psi^*_{HO}(\mathbf{x}), \tag{1.29}$$

where we recall that $(\lambda/2)(= \pi/k)$ is the lattice spacing. We find

$$\begin{aligned} t &\sim \left(\frac{1}{\ell^3}\right)\exp\left(-\frac{\pi^2}{4\ell^2k^2}\right) \\ &\sim (k^2V_0)^{3/4}\exp\left(-\sqrt{\frac{m}{8}}\frac{\pi^2}{\hbar}\frac{\sqrt{V_0}}{k}\right), \end{aligned} \tag{1.30}$$

where we notice that the hoping parameter, t, is exponentially dependent on V_0 and k. Thus t is much more strongly dependent on the experimental parameters than U, although in general t/U is the important parameter for predicting the behavior of the system. If nothing else, equations (1.30) and (1.28) give us a general idea of how this ratio should scale as the trap parameters are modified.

In the next chapter we present some useful solutions to the Bose-Hubbard model in both the weakly-interacting and strongly-interacting limits.

CHAPTER 2

REPULSIVELY INTERACTING BOSONS IN THE TIGHT-BINDING LIMIT

2.1 Weakly-interacting limit

Non-interacting lattice bosons

The spatially uniform, non-interacting Bose-Hubbard model (BHM) is described by the full Hamiltonian,

$$\hat{K} = \hat{H} - \mu\hat{N} = -t \sum_{<i,j>} (\hat{a}_i^\dagger \hat{a}_j + \hat{a}_j^\dagger \hat{a}_i) - \mu \sum_j \hat{a}_j^\dagger \hat{a}_j \,. \tag{2.1}$$

As is often the case, the symmetry of the system leads us to the "good" quantum numbers. The discrete translational symmetry of the square lattice in one-, two- or three-dimensions suggests that equation (2.1) can be diagonalized in the basis of (crystal) momentum. We take advantage of this by Fourier transforming equation (2.1) to momentum space. Normalizing the lattice spacing to 1 and imposing periodic boundary conditions (BC), the correct Fourier transform (FT) pair is

$$\hat{b}_k = \frac{1}{\Omega^{d/2}} \sum_j \hat{a}_j \, \exp(-ik \cdot j) \,, \tag{2.2}$$

$$\hat{a}_j = \frac{1}{\Omega^{d/2}} \sum_k \hat{b}_k \, \exp(ik \cdot j) \,, \tag{2.3}$$

where $\hat{b}_k$ annihilates a boson of momentum k, Ω is the number of lattice sites along each edge of the system , and d is the dimensionality of the system. The j-sum runs over all the lattice sites, while the k-sum is over the aforementioned crystal momentum ($k = (2\pi p)/\Omega$, where $p = \{-\lfloor \Omega/2 \rfloor, ..., 0, ..., \lfloor (\Omega - 1)/2 \rfloor\}$, see Arfken and Weber [17], pp.840-3, for details on discrete FT).

The number operator is easy to write in momentum space. Using the orthogonality relationship between Fourier components we find

$$-\mu \sum_j \hat{a}_j^\dagger \hat{a}_j = -\mu \sum_k \hat{b}_k^\dagger \hat{b}_k. \tag{2.4}$$

The nearest-neighbor hopping term seems more difficult, however there is a neat trick to diagonalize a square lattice of any dimension.

2.1.1 Diagonalizing The Nearest-Neighbor Hopping Term

Let's first consider the situation in one spatial dimension, where our lattice is just a chain of equally spaced sites. In this case, one can easily show that we may replace the nearest neighbor sum over i and j with a sum over j, where we have replaced the index i by $j + 1$, that is,

$$\sum_{<i,j>} (\hat{a}_i^\dagger \hat{a}_j + \hat{a}_j^\dagger \hat{a}_i) = \sum_j (\hat{a}_{j+1}^\dagger \hat{a}_j + \hat{a}_j^\dagger \hat{a}_{j+1}) . \tag{2.5}$$

Next we FT equation (2.5), and use orthogonality to diagonalize. The result is

$$\sum_{<i,j>} (\hat{a}_i^\dagger \hat{a}_j + \hat{a}_j^\dagger \hat{a}_i) = 2 \sum_k (\cos(k)) \hat{b}_k^\dagger \hat{b}_k . \tag{2.6}$$

The procedure is similar for the two-dimensional case.

In the 2-D square lattice we may represent each point by an x- and a y-component, for example, site j can be written (j_x, j_y). Also, notice that each site has four nearest neighbors, so that, in analogy with equation (2.5), we may write

$$\sum_{<i,j>} (\hat{a}_i^\dagger \hat{a}_j + \hat{a}_j^\dagger \hat{a}_i) = \sum_j (\hat{a}_{j_x+1}^\dagger \hat{a}_j + \hat{a}_j^\dagger \hat{a}_{j_x+1} + \hat{a}_{j_y+1}^\dagger \hat{a}_j + \hat{a}_j^\dagger \hat{a}_{j_y+1}) , \tag{2.7}$$

where the sum over j can equivalently be written as two sums, one over each component, that is,

$$\begin{aligned}&\sum_{j}(\hat{a}^{\dagger}_{j_x+1}\hat{a}_j + \hat{a}^{\dagger}_j\hat{a}_{j_x+1} + \hat{a}^{\dagger}_{j_y+1}\hat{a}_j + \hat{a}^{\dagger}_j\hat{a}_{j_y+1})\\ = &\sum_{j_x}\sum_{j_y}(\hat{a}^{\dagger}_{j_x+1}\hat{a}_j + \hat{a}^{\dagger}_j\hat{a}_{j_x+1} + \hat{a}^{\dagger}_{j_y+1}\hat{a}_j + \hat{a}^{\dagger}_j\hat{a}_{j_y+1})\,. \end{aligned} \tag{2.8}$$

Also, the Fourier transform pairs are conveniently written in terms of x- and y-components, that is,

$$\hat{a}_j = \frac{1}{\Omega}\sum_{k_x}\sum_{k_y}\exp\left(i(k_x j_x + k_y j_y)\right)\hat{b}_k\,, \tag{2.9}$$

and

$$\hat{a}^{\dagger}_j = \frac{1}{\Omega}\sum_{k_x}\sum_{k_y}\exp\left(-i(k_x j_x + k_y j_y)\right)\hat{b}^{\dagger}_k\,, \tag{2.10}$$

where our system is a square with Ω sites along each edge. Now substitute equations (2.9) and (2.10) into equation (2.7), and use orthogonality to diagonalize the 2-D hopping term

$$\sum_{<i,j>}(\hat{a}^{\dagger}_i\hat{a}_j + \hat{a}^{\dagger}_j\hat{a}_i) = 2\sum_{k_x}\sum_{k_y}(\cos(k_x) + \cos(k_y))\hat{b}^{\dagger}_k\hat{b}_k\,, \tag{2.11}$$

where $k = (k_x, k_y)$.

Diagonalizing the three-dimensional square (or "cubic") lattice case is exactly the same, except we just extend our procedure for an additional spatial dimension. Using the same logic as before we can immediately write the key steps leading to the final result. First, our nearest neighbor sum takes the form

$$\sum_{<i,j>}(\hat{a}^{\dagger}_i\hat{a}_j + \hat{a}^{\dagger}_j\hat{a}_i) = \sum_{j_x}\sum_{j_y}\sum_{j_z}(\hat{a}^{\dagger}_{j_x+1}\hat{a}_j + \hat{a}^{\dagger}_j\hat{a}_{j_x+1} + \hat{a}^{\dagger}_{j_y+1}\hat{a}_j + \hat{a}^{\dagger}_j\hat{a}_{j_y+1} + \hat{a}^{\dagger}_{j_z+1}\hat{a}_j + \hat{a}^{\dagger}_j\hat{a}_{j_z+1})\,. \tag{2.12}$$

The Fourier transform pair is

$$\hat{a}_j = \frac{1}{\Omega^{3/2}}\sum_{k_x}\sum_{k_y}\sum_{k_z}\exp\left(i(k_x j_x + k_y j_y + k_z j_z)\right)\hat{b}_k\,, \tag{2.13}$$

and

$$\hat{a}_j^\dagger = \frac{1}{\Omega^{3/2}} \sum_{k_x} \sum_{k_y} \sum_{k_z} \exp\left(-i(k_x j_x + k_y j_y + k_z j_z)\right) \hat{b}_k^\dagger \,. \tag{2.14}$$

Then, by substituting equations (2.13) and (2.14) into equation (2.12) and using orthogonality, we diagonalize the 3-D hopping term

$$\sum_{<i,j>} (\hat{a}_i^\dagger \hat{a}_j + \hat{a}_j^\dagger \hat{a}_i) = 2 \sum_{k_x} \sum_{k_y} \sum_{k_z} (\cos(k_x) + \cos(k_y) + \cos(k_z)) \hat{b}_k^\dagger \hat{b}_k \,, \tag{2.15}$$

where $k = (k_x, k_y, k_z)$.

2.1.2 The Spectrum and Ground State of the Non-Interacting BHM

Combining the results of the last section with equation (2.4) we may write the full non-interacting Bose-Hubbard Hamiltonian in diagonal form. For the 1-D chain we have

$$\hat{K} = -\sum_k (\mu + 2t\cos k) \hat{b}_k^\dagger \hat{b}_k \,. \tag{2.16}$$

For the 2-D square lattice we have

$$\hat{K} = -\sum_k (\mu + 2t(\cos(k_x) + \cos(k_y))) \hat{b}_k^\dagger \hat{b}_k \,. \tag{2.17}$$

And for the 3-D cubic lattice we have

$$\hat{K} = -\sum_k (\mu + 2t(\cos(k_x) + \cos(k_y) + \cos(k_z))) \hat{b}_k^\dagger \hat{b}_k \,. \tag{2.18}$$

We see that the form of equations (2.16), (2.17) and (2.18) are exactly the same except for the cosine-term, where the generalization to a system of any dimensionality is straightforward.

Now, dropping the chemical potential, μ, from the above equations for $\hat{K}$, we find that the lowest energy single-particle state is the ($k = 0$)-state in 1-D, the ($k_x = 0, k_y = 0$)-state in 2-D, and the ($k_x = 0, k_y = 0, k_z = 0$)-state in 3-D. Then, since bosons are free to multiply occupy states, the normalized ground state of non-interacting bosons at zero temperature is

$$|\psi_0\rangle = \frac{(\hat{b}_0^\dagger)^N}{\sqrt{N!}}|0\rangle\,, \tag{2.19}$$

where N is the total number of particles, $|0\rangle$ is the boson vacuum state, and $\hat{b}_0^\dagger$ represents the creation operator for the zero momentum state in any dimension.

The chemical potential is actually defined by the ground state energy, that is, $\mu = \frac{\partial E_0}{\partial N}$, and just sets the minimum value of the grand canonical energy at zero[1]. However, $|\psi_0\rangle$ is the same regardless of whether μ is included or not. Equation (2.19) is a pure Bose-Einstein Condensate (BEC), that is, each boson populates the lowest energy single-particle state. In general we define BEC as a macroscopic population of the single-particle ground state. In a real system the BEC is depleted by thermal motion, and also by scattering due to boson-boson interaction. Since optical lattice experiments investigate bosons at temperatures much lower than the BEC-transition temperature (see, for example, Greiner et. al. [12]), we choose to calculate the depletion of the BEC caused purely by interactions. We ignoring the effects due to finite temperature, which should be small in comparison.

[1]In this section I refer to the eigenvalues of $\hat{H}$ as *energy* and the eigenvalues of $\hat{K} = \hat{H} - \mu\hat{N}$ as *grand-canonical energy*. In most other sections of this dissertation the convention is to always deal with the full Hamiltonian, label it $\hat{H}$ and refer to it's eigenvalues or expectation values as "energy". However it is important for the argument in this section to differentiate between $\hat{H}$ and $\hat{K}$.

Bogoliubov diagonalization procedure

Now we consider the case where we have a finite interaction that depletes the population of a spatially uniform condensate (zero-momentum state). Suppose we tune the interaction so that it is weak enough that the overwhelming majority of bosons still occupy the zero-momentum single–particle state, but a finite amount of the bosons inhabit nonzero-momentum states. There are many approaches to finding the excitation spectrum and ground state for this system[2] . Here, I present the way that I feel is most systematic.

We begin with grand-canonical Hamiltonian for the nearest–neighbor BHM with interactions

$$\hat{K} = \hat{H} - \mu\hat{N} = -t \sum_{<i,j>} (\hat{a}_i^\dagger \hat{a}_j + \hat{a}_j^\dagger \hat{a}_i) + \frac{V_o}{2} \sum_j \hat{a}_j^\dagger \hat{a}_j^\dagger \hat{a}_j \hat{a}_j - \mu \sum_j \hat{a}_j^\dagger \hat{a}_j \,. \tag{2.20}$$

Everything in equation (2.20) is identical to equation (2.1) except we now have an interaction term where V_0 is the effective boson-boson interaction parameter. Using the commutation relations for bosonic operators, we can rewrite the interaction term with respect to the number operators for each site,

$$\frac{V_o}{2} \sum_j \hat{a}_j^\dagger \hat{a}_j^\dagger \hat{a}_j \hat{a}_j = \frac{V_o}{2} \sum_j \hat{n}_j(\hat{n}_j - 1) \,. \tag{2.21}$$

Recall that for n objects there are $\frac{n(n-1)}{2}$ distinct pairs, so the interaction term in equation (2.20) makes an energy contribution corresponding to V_0 for each distinct pair of bosons on the same lattice site. Also, since the condensate is spatially uniform μ and V_0 have no spatial dependence.

In order to find the excitations and the new ground state that results from weak interactions, we perturb the spatially uniform condensate. In practice we

[2]See, for example, Pethick and Smith, pp. 204-16 [10]; Fetter, pp. 67-72 [18]; or Pitaevskii, pp. 26-33 [19]

set each boson operator in position space equal to a uniform condensate term plus a tiny, site-dependent, bosonic fluctuation operator:

$$\hat{a}_j = \hat{\phi}_0 + \delta\hat{a}_j \,, \tag{2.22}$$

where $\hat{\phi}_0$ is the annihilation operator for the zero–momentum state (the condensate), and $\delta\hat{a}_j$ is an annihilation operator for site j with no zero–momentum component. We use $\delta\hat{a}_j$ as the small parameter to determine the corrections to the non-interacting ground state. We justify this by noting that In the Hamiltonian, the small parameter is the interaction strength, V_0, which implies $\delta\hat{a}_j$ should also be a small parameter.

Next we use the so-called "Bogoliubov prescription" (Pitaevskii and Stringari, pp. 28 [19]),

$$\hat{\phi}_0 = \sqrt{n_0} \,, \tag{2.23}$$

where n_0 is the density of the condensate. This prescription is valid due to the fact that the condensate population, $N_0 = n_0\Omega$, is macroscopic, that is,

$$N_0 \gg 1 \,. \tag{2.24}$$

In light of equation (2.24) we expect that creating or annihilating some small amount (order unity) of zero momentum bosons should have little effect on the system (see Nozieres and Pines, pp. 133-5 [20]). Quantitatively,

$$\hat{\phi}_0|\psi_0(N_0)\rangle = \sqrt{N_0}|\psi_0(N_0-1)\rangle \sim \sqrt{N_0}|\psi_0(N_0)\rangle \,, \tag{2.25}$$

and

$$\hat{\phi}_0^\dagger|\psi_0(N_0)\rangle = \sqrt{N_0+1}|\psi_0(N_0+1)\rangle \sim \sqrt{N_0}|\psi_0(N_0)\rangle \,. \tag{2.26}$$

It follows that $\hat{\phi}_0$ and $\hat{\phi}_0^\dagger$ commute with each other as well as all nonzero mo-

mentum operators, and equation (2.23) is justified[3]. Now, using equation (2.23), we rewrite equation (2.22),

$$\hat{a}_j = \sqrt{n_0} + \delta\hat{a}_j \,. \tag{2.27}$$

Next we substitute equation (2.27) into equation (2.20) and expand this new expression through quadratic order in the fluctuation operators. We expand to quadratic order since the first-order variation of the Hamiltonian must vanish in order to minimize the energy of the condensate, and this leaves the quadratic variation as the highest-order nonvanishing correction to the noninteracting system. Also, we justify stopping at quadratic order by noting that, since the fluctuations are tiny, the quadratic correction is far larger than any higher-order correction. Now, after some algebra, our result is

$$\hat{K} = K_0 + \hat{K}_1 + \hat{K}_2 \,, \tag{2.28}$$

$$K_0 = -(2d\,t + \mu)\Omega^d n_0 + \frac{1}{2}V_0\Omega^d n_0^2 \,, \tag{2.29}$$

$$\hat{K}_1 = \sqrt{n_0}(-2d\,t + V_0 n_0 - \mu)\sum_j (\delta\hat{a}_j + \delta\hat{a}_j^\dagger) \,, \tag{2.30}$$

$$\hat{K}_2 = -t\sum_{<i,j>}(\delta\hat{a}_i^\dagger\delta\hat{a}_j + \delta\hat{a}_j^\dagger\delta\hat{a}_i) + \frac{1}{2}V_0 n_0\sum_j(\delta\hat{a}_j^\dagger\delta\hat{a}_j^\dagger + \delta\hat{a}_j\delta\hat{a}_j) + \sum_j(2V_0 n_0 - \mu)\delta\hat{a}_j^\dagger\delta\hat{a}_j \,, \tag{2.31}$$

where K_0 is the grand-canonical energy of the condensate (zeroth order term), $\hat{K}_1$ is the first order variation of the condensate energy with respect to the quantum fluctuation operators, $\hat{K}_2$ is the second order variation of the condensate energy, and d is the dimensionality of the system. To minimize the energy of the condensate the first-order variation of the condensate energy must vanish, that is,

$$-2d\,t + V_0 n_0 - \mu = 0 \,. \tag{2.32}$$

[3]Note that if one writes $|\psi_0\rangle = \exp\left(\sqrt{N_0}\hat{b}_0^\dagger\right)|0\rangle$ then $\hat{\phi}_0|\psi_0\rangle = \sqrt{N_0}|\psi_0\rangle$. The particle number in this $|\psi_0\rangle$ is Poisson distributed about N_0, and as N_0 gets larger, the distribution becomes tighter about N_0. This helps explain the validity of equations (2.25) and (2.26).

As a consistency check, note that we get the same condition by setting

$$\frac{\partial K_0}{\partial n_0} = 0\,. \tag{2.33}$$

Equation (2.32) is the Gross-Pitaevskii equation (GPE) for a uniform gas on a lattice with no external field. In this case there are no spatial or temporal dynamics, so the GPE just sets the value of the chemical potential μ. Using equation (2.32), the grand-canonical energy of the condensate is then

$$K_0 = -\frac{1}{2}N_0 n_0 V_0\,. \tag{2.34}$$

Next we write what is called the "Bogoliubov Hamiltonian" (Fetter, p. 70 [18]), $\hat{K}_B$, which generally consists of a zeroth-order term and a quadratic-order term:

$$\begin{aligned}\hat{K}_B &= -\frac{1}{2}N_0 n_0 V_0 - t\sum_{<i,j>}(\delta\hat{a}_i^\dagger\delta\hat{a}_j + \delta\hat{a}_j^\dagger\delta\hat{a}_i) + \frac{1}{2}V_0 n_0\sum_j(\delta\hat{a}_j^\dagger\delta\hat{a}_j^\dagger + \delta\hat{a}_j\delta\hat{a}_j)\\ &+ \sum_j(V_0 n_0 + 2d\,t)\delta\hat{a}_j^\dagger\delta\hat{a}_j\,.\end{aligned} \tag{2.35}$$

Now recall that in the non-interacting case we guessed that crystal momenta were the good quantum numbers due to the discrete translational symmetry of the lattice. Here we make the same assumption, and our next step is to Fourier transform equation (2.35) into momentum space. First recall that $\delta\hat{a}_j$ is a site-basis operator with no zero-momentum component. It follows that the correct FT pair is

$$\hat{b}_k = \frac{1}{\Omega^{d/2}}\sum_j \delta\hat{a}_j\,\exp(-ik\cdot j)\,, \tag{2.36}$$

$$\delta\hat{a}_j = \frac{1}{\Omega^{d/2}}\sum_{k\neq 0}\hat{b}_k\,\exp(ik\cdot j)\,, \tag{2.37}$$

where $\hat{b}_k^\dagger$ and $\hat{b}_k$ are the creation and annihilation operators, respectively, for bosons of crystal momentum k. Also assume that the site index j represents

a site in any dimension and the crystal momentum k represents a momentum in any dimension. Substituting equation (2.37) and its hermitian conjugate into equation (2.35), and using the orthogonality of Fourier components, as well as the results for diagonalization of a nearest neighbor sum (see equations (2.6), (2.11) and (2.15)), we can write $\hat{K}_B$ in the momentum representation[4]. Note that this result has the same form regardless of dimensionality. The only difference is that "k" has one, two or three components, the cosine term is different (again see equations (2.6), (2.11) and (2.15)), and the chemical potential term is different as well (see equation (2.32)). It turns out that this generality will extend to all future results in this paper. For convenience, I will use the 1-D cosine and chemical potential terms, that is, $(\cos(k) - 1)$, to present these results. Here we have

$$\hat{K}_B = -\frac{1}{2}N_0 n_0 V_0 + \sum_{k\neq 0}\left[(V_0 n_0 - 2t(\cos k - 1))\hat{b}_k^\dagger \hat{b}_k + \frac{1}{2}V_0 n_0(\hat{b}_k^\dagger \hat{b}_{-k}^\dagger + \hat{b}_k \hat{b}_{-k})\right], \quad (2.38)$$

where the 2- and 3-D results are immediately acquired by substituting the appropriate cosine term, that is, $(\cos(k_x) + \cos(k_y) - 2)$ in 2-D and $(\cos(k_x) + \cos(k_y) + \cos(k_z) - 3)$ in 3-D, for "$\cos(k) - 1$".

From equation (2.38) it is straightforward to determine the eigenvalue spectrum using the Heisenberg equations of motion (HEOM) and a linear (Bogoliubov) transformation to quasiparticle operators that diagonalize K_B (Pethick and Smith, pp. 214-6 [10]). The process is as follows. First, write the HEOM using the fact that the fluctuation operators obey boson commutation relations

$$i\frac{\partial \hat{b}_q}{\partial t} = [\hat{b}_q, \hat{K}_B] = (g\, n_0 - 2t(\cos q - 1))\hat{b}_q + (V_0\, n_0)\hat{b}_{-q}^\dagger, \quad (2.39)$$

[4]Knowing that crystal momenta are the good quantum numbers, we could have immediately Fourier transformed equation (2.20) into momentum space and then decomposed each term into zero- and nonzero-momentum pieces. This process also gives equation (2.38), but it is not as general as the procedure we used in that it only works when momentum is the good quantum number, and so, for example, would fail if we added a harmonic potential.

where $\hbar = 1$. Then, in order to solve for the excitation spectrum we use a Bogoliubov transformation

$$\hat{b}_q = u_q \exp[-i\epsilon_q t]\hat{\beta}_q - v^*_{-q} \exp[i\epsilon_q t]\hat{\beta}^\dagger_{-q}\,, \tag{2.40}$$

$$\hat{b}^\dagger_{-q} = u^*_{-q} \exp[i\epsilon_q t]\hat{\beta}^\dagger_{-q} - v_q \exp[-i\epsilon_q t]\hat{\beta}_q\,, \tag{2.41}$$

where we choose $\hat{\beta}_q$ so that the time-dependent bosonic quasiparticle operator, $\hat{\beta}_q(t) = \exp[-i\epsilon_q t]\hat{\beta}_q$, diagonalizes $\hat{K}_B$, and ϵ_q is the quasiparticle spectrum. This claim is verified by the HEOM for $\hat{\beta}_q(t)$, that is,

$$\epsilon_q \hat{\beta}_q(t) = [\hat{\beta}_q(t),\, \hat{K}_B]\,, \tag{2.42}$$

which implies that $\hat{K}_B$ is of the form

$$\hat{K}_B = (Constant) + \sum_q \epsilon_q \hat{\beta}^\dagger_q \hat{\beta}_q\,. \tag{2.43}$$

Next, substitute equations (2.40) and (2.41) into equation (2.39) and we get one equation each by equating the coefficients of $\hat{\beta}_q$ and $\hat{\beta}^\dagger_{-q}$:

$$\epsilon_q u_q = (V_0\, n_0 - 2t(\cos q - 1))\, u_q - V_0\, n_0\, v_q \tag{2.44}$$

and

$$-\epsilon_q v_q = (V_0\, n_0 - 2t(\cos q - 1))\, v_q - V_0\, n_0\, u_q\,, \tag{2.45}$$

respectively. It is simple to solve equations (2.44) and (2.45) for ϵ_q, and the result is

$$\epsilon_q = \sqrt{(V_0\, n_0 - 2t(\cos q - 1))^2 - (V_0\, n_0)^2}\,, \tag{2.46}$$

which is the exact expression for the 1-D chain. Using our prescription for extending results to higher dimensions we can immediately write the expression for the excitation spectrum on a 2-D square lattice,

$$\epsilon_q(2D) = \sqrt{(V_0\, n_0 - 2t(\cos(q_x) + \cos(q_y) - 2))^2 - (V_0\, n_0)^2}\,, \tag{2.47}$$

and on a 3-D cubic lattice

$$\epsilon_q(3D) = \sqrt{(V_0\, n_0 - 2t(\cos(q_x) + \cos(q_y) + \cos(q_z) - 3))^2 - (V_0\, n_0)^2}\,. \tag{2.48}$$

Note that regardless of dimensionality we must choose the "+"–sign solution, since negative energy excitations would make the condensate unstable. A good check of equations (2.46)-(2.48) is to explore the long wavelength (small q) limit.

In the long wavelength limit, where q is much smaller than the inverse lattice spacing, we expect the lattice excitation spectrum to approach the form of the excitation spectrum for the continuous case, that is (Pitaevskii and Stringari, p. 32 [19]),

$$\epsilon(p) = \sqrt{\left(\frac{p^2}{2m}\right)^2 + \frac{g\, n_0}{m} p^2}\,, \tag{2.49}$$

where m is the mass of a single boson, p is the magnitude of the momentum (with units $(length)^{-1}$), and g is the boson-boson coupling constant. Whereas V_0 (in equation (2.46)) is the effective interaction between two bosons sharing the same lattice site, and is determined by the size of the lattice site [9], g $(=4\pi\hbar^2 a/m)$ (in equation (2.49)) is determined by measuring the scattering length a. Also, where q (in equation (2.46)) is a unitless momentum scaled by the inverse lattice spacing, p (in equation (2.49)) is momentum with units $(length)^{-1}$.

Now, considering ϵ_q in the small q limit $(cos(q) \approx 1 - \frac{q^2}{2})$, we find that equation (2.46) gives

$$\epsilon_q \approx \sqrt{(t\, q^2)^2 + 2V_0\, n_0\, t\, q^2}\,, \tag{2.50}$$

where this expression looks the same for a square lattice of any dimension if we keep in mind that q here is the *magnitude* of the momentum. If we then let $q = d\, p$, where d is the lattice spacing, and define an effective mass,

$$m^* = \frac{1}{2t\, d^2}\,, \tag{2.51}$$

then we may rewrite equation (2.50) as

$$\epsilon_p \approx \sqrt{\left(\frac{p^2}{2m^*}\right)^2 + \frac{V_0 n_0}{m^*} p^2}\,. \tag{2.52}$$

Comparing equation (2.52) with equation (2.49), we see that in the long wavelength limit the excitation spectrum for the lattice has the same form as the excitation spectrum in the continuous case. This result suggests that equation (2.46) is correct.

Our next task is to find u_q and v_{-q}, which are determined so that $\hat{K}_B$ is indeed diagonalized by $\hat{\beta}_q$ and $\hat{\beta}_q^\dagger$. First, we won't worry about time dependence anymore, so let $t = 0$ in the Bogoliubov transformation (equations (2.40) and (2.41)). Next, substitute these equations into $\hat{K}_B$ (equation (2.38)) and group the result into diagonal and off-diagonal terms[5]

$$\hat{K}_B = \hat{K}_D + \hat{K}_{OD}\,, \tag{2.53}$$

$$\begin{aligned}\hat{K}_D &= -\frac{1}{2}N_0 n_0 V_0 + \sum_k \left[(V_0\, n_0 - 2t\,(\cos k - 1))\,|v_k|^2 - \frac{1}{2}V_0\, n_0\,(v_k^* u_k + u_k^* v_k)\right] \\ &+ \sum_k \hat{\beta}_k^\dagger \hat{\beta}_k \left[(V_0\, n_0 - 2t\,(\cos k - 1))\left(|u_k|^2 + |v_k|^2\right) - V_0\, n_0\,(v_k^* u_k + u_k^* v_k)\right]\,,\end{aligned} \tag{2.54}$$

$$\begin{aligned}\hat{K}_{OD} &= \sum_k \hat{\beta}_k^\dagger \hat{\beta}_{-k}^\dagger \left[(V_0\, n_0 - 2t\,(\cos k - 1))\,(-v_{-k}^* u_k^*) + \frac{V_0\, n_0}{2}\,(v_{-k}^* v_k^* + u_k^* u_{-k}^*)\right] \\ &+ \sum_k \hat{\beta}_k \hat{\beta}_{-k} \left[(V_0\, n_0 - 2t\,(\cos k - 1))\,(-v_{-k} u_k) + \frac{V_0\, n_0}{2}\,(v_{-k} v_k + u_k u_{-k})\right]\,,\end{aligned} \tag{2.55}$$

where $\hat{K}_D$ is the ground state energy plus the diagonal $\hat{\beta}_q$ term, and $\hat{K}_{OD}$ is the off-diagonal term. We know that $\hat{K}_{OD}$ must vanish, so this gives us a condition

[5] I identify "diagonal" and "off-diagonal" terms by considering the matrix elements of each term with respect to an occupation number basis in the momentum representation.

for determining u_k and v_k. Since all of the coefficients are real, we can choose a real solution to the position basis eigenfunctions, that is, the FT of u_k and v_{-k}. This implies that $u_k = u^*_{-k}$ and $v_k = v^*_{-k}$, so the condition becomes

$$(V_0\, n_0 - 2t\,(\cos k - 1))\; u_k v_{-k} \;=\; \frac{1}{2} V_0\, n_0 \left(|v_{-k}|^2 \;+\; |u_k|^2\right). \tag{2.56}$$

The second condition for for u_k and v_{-k} results from the Bose commutation relations of $\hat{b}_k$ and $\hat{b}^\dagger_k$:

$$[\hat{b}_k\,,\, \hat{b}^\dagger_{k'}] \;=\; \delta_{k,k'}\,, \tag{2.57}$$

$$[\hat{b}_k,\, \hat{b}_{k'}] \;=\; 0\,, \tag{2.58}$$

as well as the analogous commutators for $\hat{\beta}_k$ and $\hat{\beta}^\dagger_k$. Using the Bogoliubov transformations (equation (2.40) and (2.41)) and equation (2.57) we find

$$|u_k|^2 - |v_{-k}|^2 \;=\; 1\,. \tag{2.59}$$

In the same style we use equation (2.58) to find

$$u_k v^*_k - v^*_{-k} u_{-k} \;=\; 0\,. \tag{2.60}$$

Now, since the coefficients of equation (2.56) are real, then a real solution is guaranteed to exist for u_k and v_{-k}. Assuming u_k and v_{-k} are real, and using equation (2.59) we can solve equation (2.56) for u^2_k:

$$u^2_k \;=\; \frac{1}{2}\left(1 \pm \frac{V_0\, n_0 - 2t(\cos k - 1)}{\epsilon_k}\right). \tag{2.61}$$

Since u_k is real, then u^2_k should be positive, and we must make the sign choice in equation (2.61) accordingly. However, this choice will depend on the sign of V_0. Up to this point we have not specified what range of values V_0 could take, but we can do this now by investigating the condition for thermodynamic stability of the condensate. Let's take a short aside to calculate this.

We first guarantee that the condensate is thermodynamically stable, and it turns out that this specifies the sign that V_0 must have. The conditon for thermodynamic stability can be stated (Pitaevskii and Stringari, p.29 [19])

$$\frac{\partial n_0}{\partial P} > 0\,, \tag{2.62}$$

where n_0 is the density of the condensate and P is the pressure ($P = -\frac{\partial E_0}{\partial \Omega}$). E_0 is the ground state energy (energy of the condensate) and Ω^d is the volume of the system. To lowest order approximation, the ground state energy is (see equation (2.29), and let $\mu = 0$).

$$E_0 = \frac{N_0^2\, V_0}{2\Omega^d} - 2d\, t\, N_0\,, \tag{2.63}$$

where N_0 is the number of bosons in the condensate. From these expressions we find

$$\frac{\partial n_0}{\partial P} = \frac{1}{V_0 n_0}\,, \tag{2.64}$$

thus V_0 must be greater than zero to ensure thermodynamic stability. For the remainder of the paper I will assume $V_0 > 0$, as suggested by the above result.

Since I now assume $V_0 > 0$ we must choose the "+"–sign in equation (2.61) to ensure $u_k^2 > 0$. Next, from equation (2.59) we may immediately write v_{-k}^2 , and then we have determined u_k and v_{-k} to within a sign:

$$u_k \;=\; \pm\sqrt{\frac{1}{2}\left(\frac{V_0\, n_0 - 2t(\cos k - 1)}{\epsilon_k} + 1\right)}, \tag{2.65}$$

$$v_{-k} \;=\; \pm\sqrt{\frac{1}{2}\left(\frac{V_0\, n_0 - 2t(\cos k - 1)}{\epsilon_k} - 1\right)}. \tag{2.66}$$

We constrain the sign choice and check the above result by substituting equations (2.65) and (2.66) into the coefficient of $\hat{\beta}_k^\dagger \hat{\beta}_k$ in equation (2.54). The resulting spectrum must be equal to the quasiparticle spectrum, ϵ_k (equation (2.46)), for u_k

and v_{-k} to be viable solutions. We find that we must either choose "+" in equations (2.65) and (2.66) or "−" in both equations, in order to be consistent with ϵ_k. Choosing the "+"-sign convention for u_k and v_{-k}, we then substitute these into the higher order ground state grand-canonical energy term from equation (2.54), that is,

$$E_{0,GC} = -\frac{V_0 N_0^2}{2\Omega} + \sum_{k\neq 0}\left[(V_0\, n_0 - 2t(\cos k - 1))\, v_k^2 - V_0\, n_0\, v_k u_k\right], \tag{2.67}$$

where $E_{0,GC}$ is the total ground state grand–canonical energy. Also, note that we have used the fact that u_k and v_k are real functions, and also even functions with respect to k.[6] The resulting expression for ground state grand-canonical energy is then (for dimensions one through three):

$$E_{0,GC}(1D) = -\frac{V_0 N_0^2}{2\Omega} + \frac{1}{2}\sum_{k\neq 0}\left[\epsilon_k - V_0\, n_0 + 2t(\cos k - 1)\right], \tag{2.68}$$

$$E_{0,GC}(2D) = -\frac{V_0 N_0^2}{2\Omega^2} + \frac{1}{2}\sum_{k\neq 0}\left[\epsilon_k - V_0\, n_0 + 2t(\cos(k_x) + \cos(k_y) - 2)\right], \tag{2.69}$$

$$E_{0,GC}(3D) = -\frac{V_0 N_0^2}{2\Omega^3} + \frac{1}{2}\sum_{k\neq 0}\left[\epsilon_k - V_0\, n_0 + 2t(\cos(k_x) + \cos(k_y) + \cos(k_z) - 3)\right], \tag{2.70}$$

and $\hat{K}_B$ in full diagonal form is

$$\hat{K}_B = E_{0,GC} + \sum_{k\neq 0}\epsilon_k \hat{\beta}_k^\dagger \hat{\beta}_k\,. \tag{2.71}$$

Now that we have determined the ground state grand–canonical energy and excitation spectrum of the weakly–interacting Bose gas, let's determine the actual *ground state*.

[6] Note that these quantities are functions only of the magnitude of k.

2.1.3 The Weakly Interacting Ground State

The ground state in the weakly–interacting case is defined as the quasiparticle vacuum, that is,

$$\hat{\beta}_k|GS\rangle = 0\,, \tag{2.72}$$

where $|GS\rangle$ is the weakly–interacting ground state. The weakly–interacting ground state is written in the form of a "squeezed state" , that is,

$$|GS\rangle = \exp\left(-\sum_{k\neq 0}\lambda_k \hat{b}_k^\dagger \hat{b}_{-k}^\dagger\right)|\psi_0\rangle\,, \tag{2.73}$$

where $|\psi_0\rangle$ is the non–interacting ground state (equation (2.19)). All we are left to do is to determine λ_k. But first let's give a physical interpretation of equation (2.73). Using properties of the exponential function we can rewrite equation (2.73) as

$$|GS\rangle = \prod_{k\neq 0}\sum_{q=0}^{\infty}\frac{(-\lambda_k)^q}{q!}(\hat{b}_k^\dagger \hat{b}_{-k}^\dagger)^q|\psi_0\rangle\,. \tag{2.74}$$

So $|GS\rangle$ is a product of $|k|$–states, where each $|k|$-state is a linear combo of all possible occupancies that contribute *zero* momentum. The weakly–interacting ground state is defined as a zero momentum eigenstate (see equation (2.72)), and equation (2.73) is a very general way of writing this, while allowing finite occupancy of nonzero–momentum single–particle states. Next we shift our attention to determining λ_k.

The first step is to write equation (2.72) where $\hat{\beta}_k$ is expressed in terms of the bare bosonic operators, that is,

$$(u_k\hat{b}_k + v_k\hat{b}_{-k}^\dagger)\exp\left(-\sum_{k\neq 0}\lambda_k \hat{b}_k^\dagger \hat{b}_{-k}^\dagger\right)|\psi_0\rangle = 0\,. \tag{2.75}$$

Then using the Taylor Series expansion and the commutation relations of $\hat{b}_k$ and $\hat{b}_k^\dagger$ (see equations (2.57) and (2.58)) we can show that, for any analytic function,

$F(\hat{b}_k^\dagger)$,

$$[\hat{b}_k, F(\hat{b}_k^\dagger)] = F'(\hat{b}_k^\dagger) \tag{2.76}$$

is generally true (Cohen-Tannoudji, Diu, and Laloë, pp.171-2 [21]). Using equations (2.75) and (2.76) we arrive at the following expression,

$$(-\lambda_k u_k + v_k)\hat{b}_{-k}^\dagger |GS\rangle = 0\,, \tag{2.77}$$

which is easily solved for λ_k, so we can fully specify the weakly–interacting ground state,

$$|GS\rangle = \exp\left(-\sum_{k\neq 0} \frac{v_k}{u_k} \hat{b}_k^\dagger \hat{b}_{-k}^\dagger\right)|\psi_0\rangle = 0\,. \tag{2.78}$$

In addition to determining the form of the weakly interacting ground state, we may use equation (2.72) to determine the density of noncondensed bosons, n_{nc}, where

$$n_{nc} = \frac{1}{\Omega^d} \sum_{k\neq 0} \langle \hat{b}_k^\dagger \hat{b}_k \rangle\,, \tag{2.79}$$

and in the thermodynamic limit

$$n_{nc} = \left(\frac{1}{2\pi}\right)^d \int d^d k\, \langle \hat{b}_k^\dagger \hat{b}_k \rangle\,, \tag{2.80}$$

where we integrate over all momentum space. First we calculate $\langle \hat{b}_k^\dagger \hat{b}_k \rangle$,

$$\langle \hat{b}_k^\dagger \hat{b}_k \rangle = \langle GS\,|\hat{b}_k^\dagger \hat{b}_k|GS\rangle\,, \tag{2.81}$$

where $|GS\rangle$ is determined above, and defined by equation (2.72). In order to take advantage of equation (2.72) to calculate $\langle \hat{b}_k^\dagger \hat{b}_k \rangle$ we use the Boguliubov transformation in equations (2.40) and (2.41) (at $t = 0$) to express equation (2.81) in terms of the Bogoliubov quasiparticle operators, $\hat{\beta}_k$ and $\hat{\beta}_k^\dagger$. Then it is easy to find

$$\langle \hat{b}_k^\dagger \hat{b}_k \rangle = v_k^2\,, \tag{2.82}$$

where v_k^2 is specified by equation (2.66).

We are most interested in the long-wavelength limit where $k \ll 1$, so $(\cos(k) - 1 \approx -\frac{k^2}{2})$, and the 2- and 3-D cases also return $-\frac{k^2}{2}$, where k is the magnitude of the momentum. In this limit,

$$\nu_k^2 = \frac{1}{2}\left(\frac{1+y}{(y^2+2y)^{1/2}} - 1\right), \tag{2.83}$$

where we have defined the unitless parameter $y = \frac{t}{V_0 n_0}k^2$. Now it remains to perform the integral from equation (2.80) in 1-, 2- and 3-dimensions. In one dimension we find that the integral does not converge, that is, the number of noncondensed bosons is infinite. At the beginning of this calculation we assumed that the number of noncondensed bosons would be tiny, so our calculation in one dimension is not self-consistent, and is thus fatally flawed in the thermodynamic limit. However, in two and three dimensions we get finite results:

$$n_{nc}(2D) = \frac{1}{8\pi}\frac{V_0 n_0}{t}, \tag{2.84}$$

and

$$n_{nc}(3D) = \frac{1}{6\pi^2\sqrt{2}}\left(\frac{V_0 n_0}{t}\right)^{3/2}. \tag{2.85}$$

Since we are in the weakly interacting limit, V_0/t is a small parameter, and we may specify that V_0 is small enough so that $\{n_{nc}(2D), n_{nc}(3D)\} \ll n_0$, as required to ensure self-consistency.

2.2 Strongly-interacting limit

In this section I demonstrate some important strategies for calculating ground states of the Bose-Hubbard model in the limit of strong interactions. The strongly-interacting limit implies a system where the interaction strength is the dominant energy scale and the hopping part of the Hamiltonian is treated as

a perturbation. Quantitatively we can state this limit with respect to the parameters of the Bose-Hubbard Hamiltonian, that is, $t/U \ll 1$, and where the Gutzwiller *ansatz* provides an accurate description of the system. This regime of the Bose-Hubbard model has been studied rather extensively [9, 22, 23]. In this section I present the mean-field theory of the zero-temperature phase diagram, using both analytic and the numerical techniques.

2.2.1 Phase diagram of the repulsive Bose-Hubbard Hamiltonian in the mean-field approximation

We begin by writing the Bose-Hubbard hamiltonian for a uniform system:

$$\hat{H} = -t \sum_{\langle i,j \rangle} \left(\hat{a}_i^\dagger \hat{a}_j + \hat{a}_j^\dagger \hat{a}_i \right) + \frac{1}{2} U \sum_i \hat{n}_i \left(\hat{n}_i - 1 \right) - \mu \sum_i \hat{n}_i \,, \tag{2.86}$$

where t is the hopping matrix element, U is the on-site interaction strength, and μ is the chemical potential. The indices refer to sites, and $\langle ... \rangle$ surrounding the indices denotes a nearest neighbor sum. We determine the phase diagram by calculating the expectation value of $\hat{H}$ in the mean-field approximation. The basis of our mean-field theory is the Gutzwiller product *ansatz*,

$$|G\rangle = \prod_i \left(\sum_n f_n^i |n\rangle_i \right) , \tag{2.87}$$

where $|n\rangle_i$ is the n-particle occupation number state at site i, f_n^i is the corresponding amplitude, the sum is over all possible occupation numbers, and the product is over all sites. Since the system is uniform, we are left with a single-site problem. The grand-canonical energy per site is

$$\langle \hat{H} \rangle = \frac{1}{M\,U} \langle G|H|G\rangle = -\tilde{t} |\langle \hat{a} \rangle|^2 + \frac{1}{2} \left(\langle \hat{n}^2 \rangle - \langle \hat{n} \rangle \right) - \tilde{\mu} \langle \hat{n} \rangle \,, \tag{2.88}$$

where M is the total number of sites, $\tilde{t} = t\sigma/U$, $\tilde{\mu} = \mu/U$, and σ is the coordination number of the lattice. Using the triangle inequality, one finds that, for global minima, $\langle\hat{H}\rangle(|f_m|) \leq \langle\hat{H}\rangle(f_m)$. Thus, we may assume that the f_m's are nonnegative and purely real.

We determine the superfluid energy by minimizing $\langle\hat{H}\rangle$ with respect to the normalization constraint

$$\sum_m f_m^2 = 1\,, \tag{2.89}$$

and the self-consistency equation of the superfluid order parameter, i.e.,

$$\langle\hat{a}\rangle = \sum_m \sqrt{m}\, f_{m-1}\, f_m. \tag{2.90}$$

Of course,

$$\langle\hat{n}\rangle = \sum_m m\, f_m^2\,, \tag{2.91}$$

and

$$\langle\hat{n}^2\rangle = \sum_m m^2\, f_m^2\,. \tag{2.92}$$

We use Lagrange minimization to construct an eigenvalue equation for the f_m's. We then determine the f_m's by an iterative numerical procedure [7] that is self-consistent with equation (2.90). We then calculate the energy by substituting the f_m's into $\langle\hat{H}\rangle$. In general the f_m's will all be nonzero, so $\langle\hat{a}\rangle \neq 0$, and $\langle\hat{H}\rangle$ is the mean-field ground state energy per site for the superfluid phase.

The competing phase in this Bose-Hubbard model is the zero-temperature Mott insulator. The Mott insulator phase consists of each site being filled by the number of particles that minimizes the local potential. Furthermore, tunneling between sites is completely suppressed, so $\langle\hat{a}\rangle = 0$ and $\langle n\rangle = n_{\mathrm{MI}} = \left[\tilde{\mu} + \frac{1}{2}\right]$, where the brackets denote rounding to the nearest integer. The energy of the Mott

[7] We elaborate on this procedure in chapter 4

phase is calculated by substituting n_{MI} into $\langle \hat{H} \rangle (\langle \hat{a} \rangle = 0)$. The resulting energy of the zero temperature Mott insulator state is

$$E_{MI} = \frac{1}{2}\left(n_{MI}^2 - n_{MI}\right) - \tilde{\mu} n_{MI} \,. \tag{2.93}$$

We construct the phase plot for equation (2.86) by calculating the difference between E_{MI} and $\langle \hat{H} \rangle$ over the domain of interest for $(\tilde{\mu}, \tilde{t})$. The phase with the lowest energy is the ground state. The resulting phase diagram is plotted in Figure (2.1). Due to their shape, the Mott insulator regions are commonly referred to as "Mott lobes". Including the constant $\langle \hat{n} \rangle$ contours in the superfluid region of Figure (2.1), we find that the n-particle Mott lobe has an $\langle \hat{n} \rangle = n$ contour emerging at the critical point, $\tilde{t}_c$. In the next section we calculate an analytic expression for $\tilde{t}_c$ within Gutzwiller mean-field theory.

2.2.2 Determination of $\tilde{t}_c$

Assume that we are approaching the critical point of the n-particle Mott lobe on the $\langle \hat{n} \rangle = n$ contour, and thus are operating in the canonical ensemble where we may set $\tilde{\mu} = 0$. Inside the Mott lobe we know that the ground state solution must be $f_n = 1$. Outside the Mott lobe we know that the ground state phase is superfluid, i.e., $\langle \hat{a} \rangle \neq 0$, so there must be adjacent $f_m's \neq 0$. Our *ansatz* consists of making a guess about the form of the mean-field solution for $\tilde{t}$ *just above* $\tilde{t}_c$, i.e., where the reduced hopping amplitude, τ $(= (\tilde{t} - \tilde{t}_c)/\tilde{t}_c)$, is $\ll 1$, but still greater than zero.

Within mean-field theory the distribution of f_m's in the ground state deep in the superfluid regime ($\tilde{t} \gg \tilde{t}_c$) is Poissonian, and is peaked about f_n. As $\tilde{t}$ decreases, the number fluctuations of the ground state solution decrease. That is,

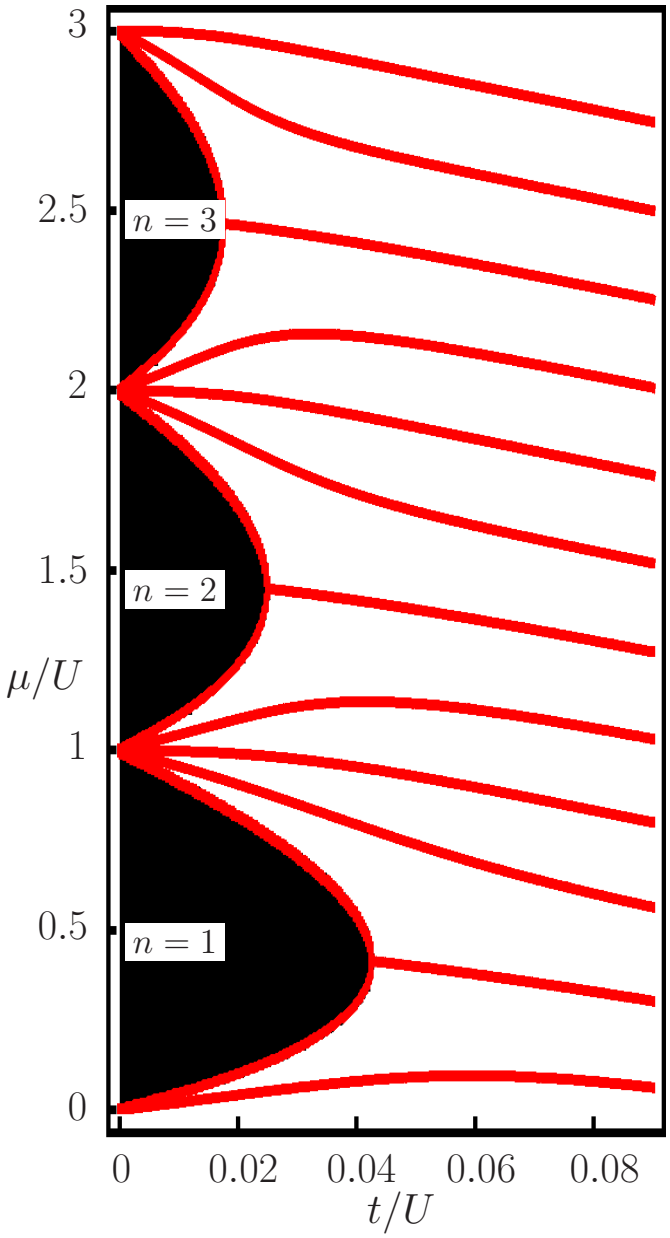

Figure 2.1: **Phase plot of the uniform Bose-Hubbard model**. The superfluid ground state dominates in the white region. The black regions are the Mott insulator phases labeled by their respective particles-per-site. The horizontal (vertical) axes are hopping parameter (chemical potential) scaled by the on-site interaction. The red lines are contours of constant total-particle density, where from bottom to top they represent $\langle \hat{n} \rangle = \{0.75 - 3.5\}$ with a spacing of 0.25. As μ/U increases, the Mott lobes continue with the same general shape, but with decreasing values of t_{critical}.

the distribution of f_m's in the ground state solution become more tightly peaked about f_n. Below the critical point the distribution is a delta function peak at f_n. So for $\tilde{t}$ just above the critical point we expect the distribution to be very close to that. Specifically, we guess that f_n is just below 1, and only the f's directly adjacent to f_n have nonzero values. If we assume that there is particle-hole symmetry in this region (i.e., $f_{n-1} = f_{n+1}$) then our *ansatz* is

$$(f_{n-1}, f_n, f_{n+1}) = \left(\varepsilon, \sqrt{1-2\varepsilon^2}, \varepsilon\right), \tag{2.94}$$

where $\varepsilon (\ll 1)$ is the order parameter. One should note that equation (2.94) is properly normalized and has $\langle \hat{n} \rangle = n$. If $\varepsilon \neq 0$ (and thus $\langle \hat{a} \rangle \neq 0$) then our solution is a superfluid, while if $\varepsilon = 0$, then the solution is a Mott insulator. The value of $\tilde{t}$ where ε first vanishes to minimize the energy is the critical value, $\tilde{t} = \tilde{t}_c$.

The recipe for finding this point is well documented in the mean-field treatment of critical phenomena [24]. We just write $\langle \hat{H} \rangle$ as power series in ε, and we find a standard ε^4-theory:

$$\langle \hat{H} \rangle = 2\tilde{t}\left((2n+1) + 2\sqrt{n(n+1)}\right)\varepsilon^4 + \left(1 - \tilde{t}\left((2n+1) + 2\sqrt{n(n+1)}\right)\right)\varepsilon^2 + \frac{1}{2}\left(n^2 - n\right) \tag{2.95}$$

To analyze equation (2.95), first re-scale ε, so that it is no longer $\ll 1$. Then one can see that at large ε the ε^4-term dominates and $\langle \hat{H} \rangle$ grows monotonically. Now, letting

$$\langle \hat{H} \rangle''(\varepsilon = 0) = \left.\frac{\partial^2 \langle \hat{H} \rangle}{\partial \varepsilon^2}\right|_{\varepsilon=0} = \left(1 - \tilde{t}\left((2n+1) + 2\sqrt{n(n+1)}\right)\right), \tag{2.96}$$

we can see that if $\langle \hat{H} \rangle'' < 0$ then $\langle \hat{H} \rangle$ has minima at $\varepsilon \neq 0$, and if $\langle \hat{H} \rangle'' > 0$ then $\langle \hat{H} \rangle$ is minimized at $\varepsilon = 0$. The critical point corresponds to the crossing point between the aforementioned solutions, that is, when $\langle \hat{H} \rangle'' = 0$. It follows that

$$\tilde{t}_c = \left[(2n+1) + 2\sqrt{n(n+1)}\right]^{-1}, \tag{2.97}$$

The entire Mott lobe is obviously not particle/hole symmetric, but in the next section we show that a suitable generalization of equation (2.94) yields the expression for the entire coexistence curve.

2.2.3 Calculation of $\tilde{\mu}_c$ and the SF-MI coexistence curve

We begin with an *ansatz* similar to equation (2.94), with one important difference. In equation (2.94) we assumed that we approached the critical point on the contour $\langle n \rangle = n$ so it was natural to guess that $f_{n-1} = f_{n+1}$ which enforces this constraint. However, to determine $\tilde{\mu}_c$ we will approach the critical point on the line of constant $\tilde{t}$, so that $\langle n \rangle$ is not fixed. Of course $\langle n \rangle = n$ at the critical point, but the value of $\tilde{\mu}_c$ will depend on how $\langle n \rangle$ approaches n as $\tilde{\mu}$ approaches $\tilde{\mu}_c$. Thus we make the slightly more general *ansatz*:

$$(f_{n-1}, f_n, f_{n+1}) = \left(\varepsilon_1, \sqrt{1 - \varepsilon_1^2 - \varepsilon_2^2}, \varepsilon_2\right), \tag{2.98}$$

where ε_1 and ε_2 are independent parameters, and thus $\langle n \rangle$ is allowed to vary close to the critical point.

We already know the value of $\tilde{t}_c$, so if we solve for $\tilde{\mu}$ with respect to $\tilde{t}$ then we will have automatically determined $\tilde{\mu}_c$. To solve for $\tilde{\mu}$ we write the expectation value of the total Hamiltonian, i.e., $\langle \hat{H} \rangle - \tilde{\mu} \langle \hat{n} \rangle$ to the lowest order in ε's that includes $\tilde{\mu}$ and $\tilde{t}$:

$$\begin{aligned} \langle \hat{H} \rangle - \tilde{\mu} \langle \hat{n} \rangle = f(\varepsilon_1, \varepsilon_2) &= -\left(n\tilde{t} + (n-1) - \tilde{\mu}\right)\varepsilon_1^2 + \left(n - (n+1)\,\tilde{t} - \tilde{\mu}\right)\varepsilon_2^2 \\ &- 2\tilde{t}\sqrt{n(n+1)}\varepsilon_1\varepsilon_2 + \frac{1}{2}\left(n^2 - n\right) - \tilde{\mu} n\,. \end{aligned} \tag{2.99}$$

It is perhaps prudent to pause here and justify writing the expression above which is cut off at second order in the ε's. We know that close enough to the

critical point only f_{n-1} and f_{n+1} will be nonzero (aside from f_n, of course, which is very close to 1), but these adjacent f's are very small with respect to f_n, which is the same as saying that ε_1 and ε_2 are $\ll 1$. Since the ε's are so small we only choose the lowest order that can provide the desired expression (in this case $\tilde{\mu}$ with respect to $\tilde{t}$). The higher order terms will be very small compared to the leading order unless the leading order does not give an expression, i.e., if we were to find $0 = 0$ or an expression for $\tilde{\mu}$ that does not depend on $\tilde{t}$. If this happened then we would merely go to the next highest order, and again try to solve for $\tilde{\mu}$. We repeat the process until we find the dependence of $\tilde{\mu}$ on $\tilde{t}$. This is equivalent to discovering a degeneracy (i.e., no correction) at the leading order in perturbation theory and thus moving on to higher orders until this degeneracy is broken. But of course, we always start off with the lowest non-vanishing order equation and only move on to higher orders if necessary. In this case we will find that it is not necessary to consider higher orders in ε.

By minimizing $f(\varepsilon_1, \varepsilon_2)$ with respect to ε_1 we get the condition

$$(n\tilde{t} + (n-1) - \tilde{\mu})\,\varepsilon_1 + \tilde{t}\sqrt{n(n+1)}\varepsilon_2 = 0\,, \tag{2.100}$$

while minimizing $f(\varepsilon_1, \varepsilon_2)$ with respect to ε_2 yields,

$$(n - (n+1)\,\tilde{t} - \tilde{\mu})\,\varepsilon_2 - \tilde{t}\sqrt{n(n+1)}\varepsilon_1 = 0\,. \tag{2.101}$$

Equations (2.100) and (2.101) constitute an eigenvalue problem for $\tilde{\mu}$, which is easily solved to give

$$\tilde{\mu}_\pm = \left(n - \frac{1}{2}(1+\tilde{t})\right) \pm \sqrt{\frac{1}{4}\tilde{t}^2 - \left(n + \frac{1}{2}\right)\tilde{t} + \frac{1}{4}}\,. \tag{2.102}$$

$\tilde{\mu}_+$ is the expression for the coexistence curve of the n-particle lobe when $\tilde{\mu} > \tilde{\mu}_c$, while $\tilde{\mu}_-$ is the expression when $\tilde{\mu} < \tilde{\mu}_c$. When $\tilde{t} = \tilde{t}_c$ the square-root term

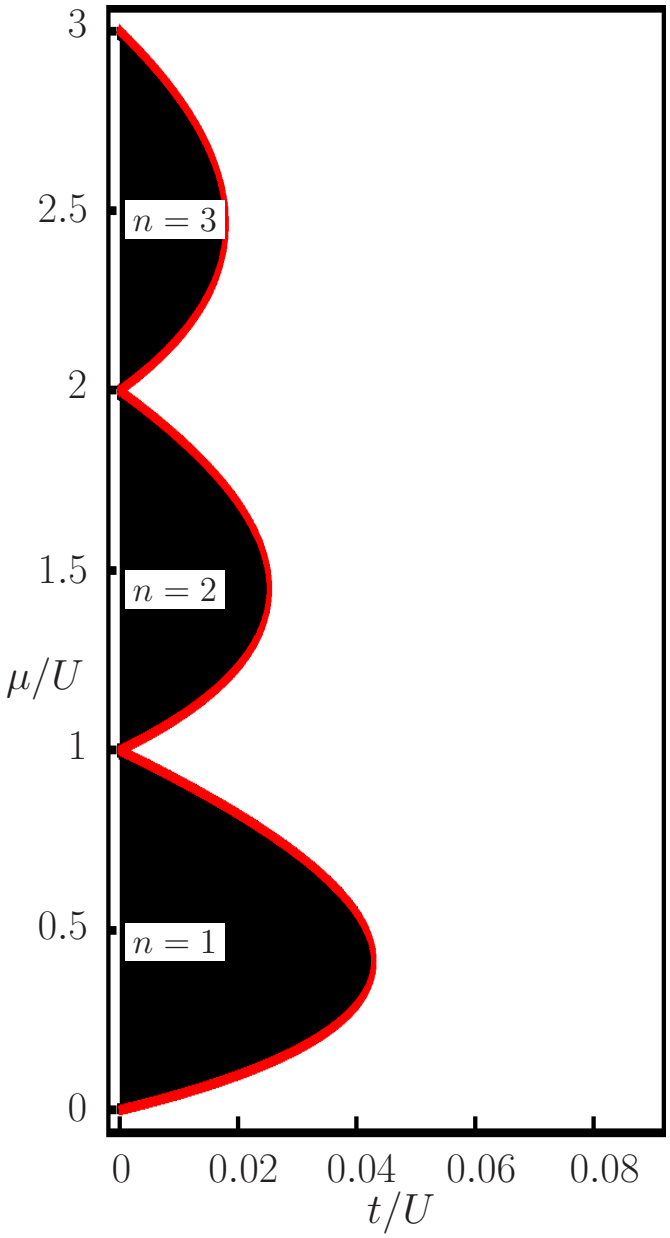

Figure 2.2: **Comparison of numerical and analytic calculations**. The white and black regions reflect the results of the numerical calculation of the phase diagram. The superfluid ground state dominates in the white region. The black regions are the Mott insulator phases labeled by their respective particles-per-site. The horizontal (vertical) axes are hopping parameter (chemical potential) scaled by the on-site interaction. The red curve is the coexistence curve calculated analytically from mean-field theory (equation (2.103)).

in equation (2.102) vanishes, and we obtain the value of the critical chemical potential for the n-particle lobe, that is,

$$\tilde{\mu}_c = n - \frac{1}{2}(1 + \tilde{t}_c) \ . \tag{2.103}$$

In Figure (2.2) we plot the first three Mott lobes from numerical mean-field theory, as well as the analytic coexistence curves determined immediately above (equation (2.103)). The close agreement in Figure (2.2) suggests that our analytic expression is correct.

CHAPTER 3

BOSONS ON A ROTATING OPTICAL LATTICE

The final ingredient for understanding the work presented later in this dissertation, is a basic knowledge of the response of ultracold lattice bosons to rotation of the lattice. In this chapter I describe how to modify the Bose-Hubbard Hamiltonian to account for the effects of rotation, and then how to calculate a vortex ground state using Gutzwiller mean-field theory.

3.1 The Bose-Hubbard Hamiltonian in a rotating frame

In Chapter 1 we showed how the tight-binding approximation connects the continuum model of lattice bosons to the Bose-Hubbard model. In the current section, we will show how the same reasoning can be used to arrive at a tight-binding model for a rotating lattice system. We start with a continuum description of a Bose gas with a point interaction

$$\begin{aligned} \hat{H} &= \int d^3\vec{x}\, \hat{\psi}^\dagger(\vec{x}) \left(-\frac{\hbar^2}{2m}\vec{\nabla}^2 + V_O(\vec{x}) - \mu \right) \hat{\psi}(\vec{x}) \\ &+ \frac{1}{2} g \int d^3\vec{x}\, \hat{\psi}^\dagger(\vec{x})\, \hat{\psi}^\dagger(\vec{x})\, \hat{\psi}(\vec{x})\, \hat{\psi}(\vec{x}) \ , \end{aligned} \tag{3.1}$$

where $\hat{\psi}(\vec{x})$ is a boson field operator, $V_O(\vec{x})$ is the optical lattice potential, μ is the chemical potential, and g is the usual interaction parameter dependent on the s-wave scattering length. We then expand the field operators in the basis of Wannier states, $w(\vec{x} - \vec{x}_i)$,

$$\hat{\psi}(\vec{x}) = \sum_i \hat{a}_i\, w(\vec{x} - \vec{x}_i) \ , \tag{3.2}$$

where $\hat{a}_i$ is a boson annihilation operator for optical lattice site i. Substituting equation (3.2) into equation (3.1), and using the fact that each Wannier state is

tightly localized about its respective optical lattice sight, we may then argue for the following effective Hamiltonian,

$$\hat{H} = -t \sum_{\langle i,j \rangle} \left(\hat{a}_i^\dagger \hat{a}_j + \hat{a}_j^\dagger \hat{a}_i \right) + \frac{1}{2} U \sum_i \hat{n}_i \left(\hat{n}_i - 1 \right) - \mu \sum_i \hat{n}_i \,, \tag{3.3}$$

where

$$t = \int d^3\vec{\boldsymbol{x}}\, w^*(\vec{\boldsymbol{x}} - \vec{\boldsymbol{x}}_i) \left(-\frac{\hbar^2}{2m} \vec{\boldsymbol{\nabla}}^2 + V_O(\vec{\boldsymbol{x}}) \right) w\left(\vec{\boldsymbol{x}} - \vec{\boldsymbol{x}}_j \right) \tag{3.4}$$

is the hopping matrix element between nearest neighbor sites i and j, and

$$U = g \int d^3\vec{\boldsymbol{x}} \, |w(\vec{\boldsymbol{x}} - \vec{\boldsymbol{x}}_i)|^4 \tag{3.5}$$

is the on-site interaction parameter. Next, we construct a Bose-Hubbard model for a gas of bosons in a rotating frame. We will find that this is easily done when we take for granted the procedure outlined above.

First, we write the classical relationship between the Hamiltonian in the non-rotating reference frame, H_{NR}, and the Hamiltonian in the rotating reference frame, H_R,

$$H_R = H_{NR} - \vec{\boldsymbol{\Omega}} \cdot \vec{\boldsymbol{L}} \,, \tag{3.6}$$

where $\vec{\boldsymbol{\Omega}}$ is the rotation velocity, and $\vec{\boldsymbol{L}}$ is the angular mometum. Writing out the terms explicitly we have

$$H_R = \frac{p^2}{2m} - \vec{\boldsymbol{\Omega}} \cdot (\vec{\boldsymbol{x}} \times \vec{\boldsymbol{p}}) + V(\vec{\boldsymbol{x}}) \,, \tag{3.7}$$

where $V(\vec{\boldsymbol{x}})$ is the sum of the optical lattice potential, $V_O(\vec{\boldsymbol{x}})$, and the external trapping potential, $V_T(\vec{\boldsymbol{x}})$, minus the chemical potential, μ. Next recall that the quantity $\vec{\boldsymbol{\Omega}} \cdot (\vec{\boldsymbol{x}} \times \vec{\boldsymbol{p}})$ is cyclically invariant, and thus we complete the square with respect to $\vec{\boldsymbol{p}}$,

$$H_R = \frac{1}{2m} \left(\vec{\boldsymbol{p}} - m(\vec{\boldsymbol{\Omega}} \times \vec{\boldsymbol{x}}) \right)^2 - \frac{1}{2} m \Omega^2 x^2 + V(\vec{\boldsymbol{x}}) \,. \tag{3.8}$$

Next, since $V_T(\vec{x})$ and $-\frac{1}{2}m\Omega^2 x^2$ are both slowly varying near the center of the trap, then we may set Ω so that they effectively cancel [25]. Using this cancellation, and substituting the first quantization operator for momentum, we have

$$H_R = -\frac{\hbar^2}{2m}\left(\vec{\nabla} - i\vec{A}(\vec{x})\right)^2 + V_O(\vec{x}) - \mu\,, \tag{3.9}$$

where $\vec{A}(\vec{x}) = \frac{m}{\hbar}\left(\vec{\Omega}\times\vec{x}\right)$. Next we write equation (3.9) in second-quantized form using bosonic field operators and adding a point interaction,

$$\begin{aligned}\hat{H} &= \int d^3\vec{x}\,\hat{\psi}^\dagger(\vec{x})\left(-\frac{\hbar^2}{2m}\left(\vec{\nabla} - i\vec{A}(\vec{x})\right)^2 + V_O(\vec{x}) - \mu\right)\hat{\psi}(\vec{x}) \\ &+ \frac{1}{2}g\int d^3\vec{x}\,\hat{\psi}^\dagger(\vec{x})\,\hat{\psi}^\dagger(\vec{x})\,\hat{\psi}(\vec{x})\,\hat{\psi}(\vec{x})\ .\end{aligned} \tag{3.10}$$

Comparing equation (3.10) with equation (3.1) we see that the only difference is the rotation potential $\vec{A}(\vec{x})$. Our strategy will be to expand the operators in a basis that essentially reduces the physics of equation (3.10) to the physics of equation (3.1), so that we may then use the same argument as before to arrive at a Bose-Hubbard Hamiltonian analogous to equation (3.3).

We guess a solution consisting of an expansion with respect to a basis of Wannier functions (as before) with an additional phase factor dependent on $\vec{A}(\vec{x})$,

$$\hat{\psi}(\vec{x}) = \sum_j \hat{a}_j\, w\left(\vec{x} - \vec{x}_j\right)\exp\left[i\int_{\vec{x}_j}^{\vec{x}} d^3\vec{r}\cdot\vec{A}(\vec{r})\right]. \tag{3.11}$$

This guess is physically motivated in that we expect the same order of magnitude arguments (related to localization about lattice sites) to hold in the rotating case, as were used in the non-rotating case. The phase factor is a convenient choice because it has the effect of reducing the Hamiltonian (3.10) to the form

of (3.1), that is,

$$\left(\vec{\boldsymbol{\nabla}} - i\vec{\boldsymbol{A}}(\vec{\boldsymbol{x}})\right)^2 \left(w\left(\vec{\boldsymbol{x}} - \vec{\boldsymbol{x}}_j\right) \exp\left[i \int_{\vec{\boldsymbol{x}}_j}^{\vec{\boldsymbol{x}}} d^3\vec{\boldsymbol{r}} \cdot \vec{\boldsymbol{A}}(\vec{\boldsymbol{r}}) \right] \right) = \left(\vec{\boldsymbol{\nabla}}^2 w\left(\vec{\boldsymbol{x}} - \vec{\boldsymbol{x}}_j\right)\right) \exp\left[i \int_{\vec{\boldsymbol{x}}_j}^{\vec{\boldsymbol{x}}} d^3\vec{\boldsymbol{r}} \cdot \vec{\boldsymbol{A}}(\vec{\boldsymbol{r}}) \right]. \tag{3.12}$$

Now, since the exponential term cannot be greater than one, we may use the same order of magnitude arguments as in the non-rotating case to arrive at a Bose-Hubbard Hamiltonian in the rotating reference frame,

$$\hat{H}_{R,BH} = -t \sum_{\langle i,j \rangle} \left(\hat{a}_i^\dagger \hat{a}_j \exp\left[i \int_{\vec{\boldsymbol{x}}_j}^{\vec{\boldsymbol{x}}_i} d\mathbf{r} \cdot \vec{\boldsymbol{A}}(\vec{\boldsymbol{r}}) \right] + h.c. \right) + \frac{1}{2} U \sum_i \hat{n}_i \left(\hat{n}_i - 1\right) - \mu \sum_i \hat{n}_i \,. \tag{3.13}$$

This Hamiltonian has now been used extensively in the study of ultracold atoms, beginning with Wu et. al. [25]. Historically, its development began in the problem of lattice electrons in a magnetic field, where the procedure of replacing $\hbar\vec{\boldsymbol{k}}$ with $\vec{\boldsymbol{p}} - e\vec{\boldsymbol{A}}(\vec{\boldsymbol{x}})/c$ in the tight-binding Bloch functions is known as the *Peierls substitution* [26]. Next, it is appropriate to analyze our derivation procedure, as well as the validity of equation (3.13).

One important point is whether the tight-binding approximation used above is really valid in the presence of fast rotation, and a harmonic trapping potential. One might worry that we must self-consistently calculate t and U at each site. For sufficiently deep lattices this worry is unfounded. If rotation and the external trapping potential do not deform the atomic wavepackets centered at each site, then the tight-binding approximation is valid. We check this by comparing the effective "oscillator length" for each confining potential; the oscillator length is the length scale on which the potential deforms a wavefunction. For our system the oscillator lengths are $d_{OL} = \sqrt{\hbar/m\omega_{OL}}$, $d_{Rot} = \sqrt{\hbar/m\Omega}$, and $d_{ext} = \sqrt{\hbar/m\omega}$, where ω_{OL}, Ω, and ω are the angular frequencies representing a single optical-lattice well, rotation, and the external harmonic trap, respectively. Each site-centered atomic wavepacket has length scale d_{OL}, so as long as $d_{OL} \ll \{d_{Rot}, d_{ext}\}$,

then the hamiltonian above is valid.

3.2 A single 2π-vortex

In this section our goal is to simulate a singly-quantized vortex that is part of an infinite square lattice of such vortices. We do this using the above Bose-Hubbard Hamiltonian in a rotating reference frame (equation (3.13)), and using Gutzwiller mean-field theory. First let's discuss how the quantized circulation of a superfluid constrains the solutions of this Hamiltonian.

3.2.1 quantized circulation

Since a superfluid can be described by a macroscopic wavefunction with a well-defined phase, its velocity is written $\vec{\boldsymbol{v}} = \frac{\hbar}{m}\vec{\boldsymbol{\nabla}}\phi$, where ϕ is the phase of the superfluid order parameter. It follows that the velocity field is irrotational, that is, $\vec{\boldsymbol{\nabla}} \times \vec{\boldsymbol{v}} = 0$, except where ϕ is singular.

Since the condensate wavefunction must be single valued, then the difference in the phase around a closed contour must be an integer multiple of 2π, that is,

$$\Delta\phi = \oint \vec{\boldsymbol{\nabla}}\phi \cdot d\vec{\boldsymbol{s}} = 2\pi\ell, \tag{3.14}$$

where ℓ is an integer. The quantization of the circulation, Γ, is then easily discovered,

$$\Gamma = \oint \vec{\boldsymbol{v}} \cdot d\vec{\boldsymbol{s}} = \frac{\hbar}{m} 2\pi\ell = \ell\frac{h}{m}\,. \tag{3.15}$$

Now let's define our rotation velocity, $\vec{v}_R$,

$$\vec{v}_R = \vec{\Omega} \times \vec{r}\,, \tag{3.16}$$

thus

$$\vec{A} = \frac{m}{\hbar}\vec{v}_R\,. \tag{3.17}$$

Then, using equations (3.15) and (3.17) we find that

$$\oint \vec{A} \cdot d\vec{s} = 2\pi\ell\,. \tag{3.18}$$

Next, we specify that our calculation takes place on a square region with side length L, where the lattice geometry is square and we have scaled all lengths by the nearest-neighbor lattice spacing. We simulate a singly-quantized vortex in this region, so it follows that equation (3.18), with $\ell = 1$, holds when the closed loop is the boundary of our square region. By performing this integral we find the value of Ω fixed by our circulation constraint. First, let $\vec{\Omega} = \Omega\hat{z}$, $d\vec{s} = dx\hat{x}+dy\hat{y}$, and let the bottom left-corner of our region be labeled (x_0, y_0). We can then write the total contour integral as the sum of four 1-D integrals (one for each boundary edge),

$$I. \int_{x_0}^{x_0+L} \vec{A} \cdot d\vec{s} = -\frac{m\Omega}{\hbar} y_0 L \tag{3.19}$$

$$II. \int_{y_0}^{y_0+L} \vec{A} \cdot d\vec{s} = \frac{m\Omega}{\hbar}(x_0 + L)L \tag{3.20}$$

$$III. \int_{x_0+L}^{x_0} \vec{A} \cdot d\vec{s} = \frac{m\Omega}{\hbar}(y_0 + L)L \tag{3.21}$$

$$IV. \int_{y_0+L}^{y_0} \vec{A} \cdot d\vec{s} = -\frac{m\Omega}{\hbar} x_0 L\,. \tag{3.22}$$

Using equation (3.18), we then find $\Omega = (\pi\hbar)/(mL^2)$.

3.2.2 The Gutzwiller approach to a system of rotating bosons

Our goal here is to calculate the density and the superfluid density for each site in our lattice. We does this by treating our Hamiltonian (equation (3.13)) self-consistently. The first step is to calculate the expectation value of the Hamiltonian using the Gutzwiller *ansatz* for the ground state,

$$|\Psi\rangle = \prod_i \left(\sum_n f_n^i |n\rangle_i \right), \tag{3.23}$$

where i is the site index and $\{|n\rangle\}$ is the orthonormal single-site occupation number basis, and we assume that the wavefunction for each site is normalized,

$$\sum_n |f_n^i|^2 = 1\,. \tag{3.24}$$

Next we calculate the expectation value of the Hamiltonian piece-by-piece.

The expectation value of the density is written

$$\langle \hat{n}_j \rangle = \langle \Psi | \hat{n}_j | \Psi \rangle = \sum_n n |f_n^j|^2\,, \tag{3.25}$$

and the density-squared is

$$\langle \hat{n}_j^2 \rangle = \sum_n n^2 |f_n^j|^2\,. \tag{3.26}$$

The expectation value of the hopping term is written

$$\langle \hat{a}_i^\dagger \hat{a}_j \rangle = \langle \hat{a}_i^\dagger \rangle \langle \hat{a}_j \rangle = \left(\sum_n \sqrt{n+1} (f_{n+1}^i)^* f_n^i \right) \left(\sum_n \sqrt{n} (f_{n-1}^j)^* f_n^j \right). \tag{3.27}$$

We now proceed with Lagrange minimization. Equation (3.24) gives the set of normalization constraints, and thus the equation to minimize is

$$G = \langle \hat{H} \rangle + \sum_i \lambda_i \left(\sum_n |f_n^i|^2 - 1 \right), \tag{3.28}$$

where the λ_i's are the Lagrange multipliers. Next we minimize this equation by setting

$$\frac{\partial G}{\partial (f_m^i)^*} = 0\,, \tag{3.29}$$

which returns coupled eigenvalue equations, one for each site,

$$\begin{aligned}\frac{\partial G}{\partial (f_m^i)^*} &= -t \sum_{j,\,\text{nn of } i} \left(\langle \hat{a}_j \rangle \sqrt{m}\, f_{m-1}^i R_{ij} + \langle \hat{a}_j^\dagger \rangle \sqrt{m+1}\, f_{m+1}^i R_{ji} \right) \\ &+ \left(\frac{U}{2} m^2 - \left(\mu + \frac{U}{2} \right) m + \lambda_i \right) f_m^i = 0\,. \end{aligned} \tag{3.30}$$

In equation (3.30) the sum is over j that are nearest neighbors of i, and

$$R_{ij} = \exp\left[i \int_{\vec{x}_j}^{\vec{x}_i} d\vec{r} \cdot \vec{A}(\vec{r}) \right], \tag{3.31}$$

where the i inside the exponential is just $\sqrt{-1}$, and $\vec{x}_i$ is the position of site i.

We may rewrite equation (3.30) in more explicit fashion by using the fact that we are referring to a two-dimensional square lattice.

$$\begin{aligned} &- t \left(\langle \hat{a}_{ix+1} \rangle R_{i,ix+1} + \langle \hat{a}_{ix-1} \rangle R_{i,ix-1} + \langle \hat{a}_{iy+1} \rangle R_{i,iy+1} + \langle \hat{a}_{iy-1} \rangle R_{i,iy-1} \right) \sqrt{m}\, f_{m-1}^i \\ &- t \left(\langle \hat{a}_{ix+1}^\dagger \rangle R_{ix+1,i} + \langle \hat{a}_{ix-1}^\dagger \rangle R_{ix-1,i} + \langle \hat{a}_{iy+1}^\dagger \rangle R_{iy+1,i} + \langle \hat{a}_{iy-1}^\dagger \rangle R_{iy-1,i} \right) \sqrt{m+1}\, f_{m+1}^i \\ &+ \left[\frac{U}{2} m^2 - \left(\mu + \frac{U}{2} \right) m \right] f_m^i = -\lambda_i f_m^i\,, \end{aligned} \tag{3.32}$$

where the Cartesian coordinates (ix, iy) refer to site i. Also, we use some shorthand notation in equation (3.32), for example,

$$R_{i,ix+1} \text{ is equivalent to } R_{(ix,iy),(ix+1,iy)}\,, \tag{3.33}$$

and

$$\langle \hat{a}_{ix+1} \rangle \text{ is equivalent to } \langle \hat{a}_{(ix+1,iy)} \rangle\,. \tag{3.34}$$

By simple calculation we find that

$$R_{ix+1,i} = R_{i,ix-1} = \exp\left[-i \frac{\pi}{L^2} (iy) \right] = R_{i,ix+1}^* = R_{ix-1,i}^*\,, \tag{3.35}$$

and

$$R_{iy+1,i} = R_{i,iy-1} = \exp\left[i\frac{\pi}{L^2}(ix)\right] = R^*_{i,iy+1} = R^*_{iy-1,i}\,. \tag{3.36}$$

Next we write the elements of the eigenvalue matrix, M, for each site:

$$M[m,m] = \frac{U}{2}m^2 - \left(\mu + \frac{U}{2}\right)m\,, \tag{3.37}$$

$$\begin{aligned} M[m+1,m] = \; &- \; t\sqrt{m+1}\left(\langle\hat{a}_{ix+1}\rangle \exp\left[i\frac{\pi}{L^2}(iy)\right] + \langle\hat{a}_{ix-1}\rangle \exp\left[-i\frac{\pi}{L^2}(iy)\right]\right) \\ &- \; t\sqrt{m+1}\left(\langle\hat{a}_{iy+1}\rangle \exp\left[-i\frac{\pi}{L^2}(ix)\right] + \langle\hat{a}_{iy-1}\rangle \exp\left[i\frac{\pi}{L^2}(ix)\right]\right), \end{aligned} \tag{3.38}$$

and

$$\begin{aligned} M[m-1,m] = \; &- \; t\sqrt{m}\left(\langle\hat{a}^\dagger_{ix+1}\rangle \exp\left[-i\frac{\pi}{L^2}(iy)\right] + \langle\hat{a}^\dagger_{ix-1}\rangle \exp\left[i\frac{\pi}{L^2}(iy)\right]\right) \\ &- \; t\sqrt{m}\left(\langle\hat{a}^\dagger_{iy+1}\rangle \exp\left[i\frac{\pi}{L^2}(ix)\right] + \langle\hat{a}^\dagger_{iy-1}\rangle \exp\left[-i\frac{\pi}{L^2}(ix)\right]\right). \end{aligned} \tag{3.39}$$

We must now specify the geometry of the region on which we will perform calculations.

We perform calculations on a two-dimensional square lattice with L sites per side, and where the lattice spacing is scaled to unity. We now specify that the coordinate origin is the center of rotation, so that the sites of this lattice are labeled by the Cartesian coordinates $(-L/2, -L/2)$ for the bottom left-hand corner and $(L/2-1, L/2-1)$ for the top right-hand corner. Since the eigenvalue equation for each site depends upon the value of the superfluid order parameter ($\langle\hat{a}\rangle$) at each nearest-neighbor site. Thus we must specify boundary conditions, which turn out to be quite important in determining the ground state. The choice of boundary conditions is the topic of the next subsection.

3.2.3 Boundary conditions for a square vortex lattice

In a fast enough rotating condensate the angular momentum of the fluid is stored in a vortex lattice. In a free condensate the lattice geometry is triagonal, however, if the condensate is trapped by a deep enough optical lattice, then the vortex lattice will share the geometry of the optical lattice [8, 27, 28]. Here we treat one singly-quantized vortex that is part of a square lattice of such vortices, and then develop the appropriate boundary conditions.

The order parameter $\langle \hat{a} \rangle$ can be conveniently written as a complex number in the polar representation, that is, $\langle \hat{a} \rangle = \alpha = |\alpha| \exp i\phi$. The magnitude of the order parameter, $|\alpha|$, is just the square root of the local condensate density[1], and ϕ is the local phase of the condensate wavefunction. Since the position of the vortex cores is periodic and the underlying potential is uniform, then it is natural to assume that each core has the same condensate density profile, so

$$|\alpha(x_0 + nL, y_0 + mL)| = |\alpha(x_0, y_0)|\,, \tag{3.40}$$

where n and m are integers. The more complicated matter is determining the boundary conditions for ϕ. The most natural way to develop these conditions is through the group theory treatment of Zak [29, 30], while the analogous "magnetic boundary conditions" for electrons on a two-dimensional lattice are discussed in Thouless et. al. [31]. The boundary conditions are:

$$\begin{aligned} \alpha\,(x + L, y) &= -\alpha\,(x, y) \exp\left[-i\frac{\pi}{L}\,(2y_v - y)\right], \\ \alpha\,(x, y + L) &= -\alpha\,(x, y) \exp\left[+i\frac{\pi}{L}\,(2x_v - x)\right], \end{aligned} \tag{3.41}$$

where (x_v, y_v) is the shift of the central vortex core off the center of rotation.

[1] In the Gutzwiller mean-field approximation "condensate density" and "superfluid density" are equivalent.

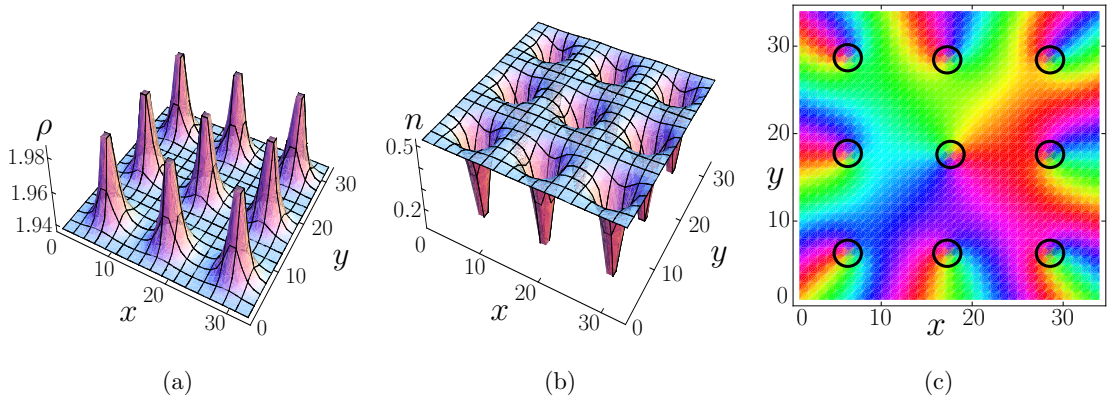

Figure 3.1: **Simulation of a vortex lattice**. Results of a vortex lattice calculation performed with the methods outlined in this chapter. The calculations are performed over a square lattice region where the Cartesian coordinates denoted (x, y) are scaled by the optical lattice constant. The central vortex region was calculated using numerical self-consistency and the appropriate boundary conditions. The outer vortices are generated by applying the boundary conditions to the solution there. (a) Density, ρ: The density is peaked in the vortex cores due to the emergence of the Mott insulator phase there. (b) Superfluid density, n: The superfluid density vanishes at the center of each vortex core and then gradually "heals" toward its bulk value. (c) Complex phase field, where $[0, 2\pi]$ is denoted by "Hue". Continuous cycling of the phase about a point indicates a vortex core there. In this case each vortex is singly quantized (has a phase winding of 2π). Black circles are drawn around vortex cores as a guide to the eye.

Using these boundary conditions we numerically simulate a vortex lattice of bosons on a rotating optical lattice (Figure (3.1)). We use the mean-field theory developed in the previous section to calculate the density profile of the central vortex, and then use boundary conditions to extend the result. Notice that the density profile and condensate density profile are qualitatively different. This is due to the emergence of the Mott insulator phase in the vortex core. This phenomenon was first calculated in the context of ultracold lattice bosons by

Wu et. al. in 2004 [25].

In the next chapter we use the methods developed here to investigate the structural phases of vortex lattices of bosons in a deep rotating optical lattice.

CHAPTER 4

STRUCTURAL PHASE TRANSITIONS FOR VORTEX LATTICES OF BOSONS IN DEEP ROTATING OPTICAL LATTICES NEAR THE MOTT BOUNDARY

The contents of this chapter are adapted from work originally published as *Vortex lattices of bosons in deep rotating optical lattices*, Phys. Rev. A, **77**, 033629 (2008).

In this chapter we study vortex-lattice phases for a Bose gas trapped in a rotating optical-lattice near the superfluid–Mott-insulator transition. We find a series of abrupt structural phase transitions where vortices are pinned with their cores only on plaquettes or only on sites. We discuss connections between these vortex structures and the Hofstadter-butterfly spectrum of free particles on a rotating lattice.

4.1 Introduction

Two of the most exciting directions in cold-atom research involve studying lattice systems and rotating systems [1]. By increasing the importance of interactions compared to kinetic energy, lattices allow one to study strongly correlated phenomena such as the boson superfluid–Mott-insulator transition [12]. These lattice systems are ideal for studying model many-body systems and protocols for quantum information processing [2]. Rotating gases lead to interesting vortex physics [32, 33, 34, 35], and the promise of exotic states such as those which give rise to analogs of fractional quantum-Hall effects [36, 37]. Here we study the interplay of lattice physics and rotation physics by calculating the vortex-

lattice structures near a Mott transition.

In the absence of an optical lattice a rotating Bose-Einstein Condensate (BEC) develops a triangular lattice of singly quantized vortices [33, 34]. This triangular configuration minimizes the logarithmic vortex-vortex interaction. However, as seen in recent experiments far from the Mott regime [28], a sufficiently deep optical-lattice potential will pin these vortices at the maxima of that potential [8, 27, 38].

In this chapter we show that qualitatively different behavior can be seen in the superfluid state near the Mott-insulator phase. We find that due to changes in the structure of the vortex cores the vortices can actually be pinned at the minima of the potential. In Sec. II we perform numerical mean-field calculations, and find a sequence of first-order transitions between site-centered and plaquette-centered vortex lattices. In Sec. III we use a reduced basis *ansatz* to perform analytic calculations near the Mott boundary, and as a result show how the theory at the Mott boundary is related to the Hofstadter butterfly spectrum. In Sec. IV we summarize our results.

4.2 Numerical calculation of vortex-lattice states

4.2.1 Mean-field theory of the rotating Bose-Hubbard model

We consider a deep lattice where we can make a tight-binding approximation [9], and the system is described in the rotating frame by a Bose-Hubbard

Hamiltonian [25],

$$\hat{H}_{RBH} = -t \sum_{\langle i,j \rangle} \left(\hat{a}_i^\dagger \hat{a}_j \exp\left[i \int_{\vec{r}_j}^{\vec{r}_i} d\vec{r} \cdot \vec{A}(\vec{r}) \right] + H.c. \right) + \frac{1}{2} U \sum_i \hat{n}_i (\hat{n}_i - 1) - \mu \sum_i \hat{n}_i \,. \quad (4.1)$$

Above, the operator $\hat{a}_i^\dagger$ ($\hat{a}_i$) creates (destroys) a boson and $\hat{n}_i$ is the number operator at optical-lattice site i. The subscript $\langle i, j \rangle$ denotes a nearest-neighbor sum. The parameters t, U, and μ are the hopping matrix element, the on-site repulsion strength, and the chemical potential, respectively. Rotation produces the vector potential $\vec{A}(\vec{r}) = (m/\hbar)\left(\vec{\Omega} \times \vec{r}\right) = \pi\nu\,(x\hat{y} - y\hat{x})$, where ν is the number of circulation quanta (h/m, where m is the atomic mass, and h is 2π times Planck's constant $\hbar$) per optical-lattice site. Rotation also produces a harmonic centrifugal-potential which we have assumed is cancelled by a harmonic trap. Although we choose to work in the symmetric gauge our results are not gauge dependent. Scaling energies by U and distances by the lattice constant, the system is characterized by the unitless parameters $\tilde{t}\,(= t/U)$, $\tilde{\mu}\,(= \mu/U)$ and ν.

We choose to model a uniform system, rather than explicitly considering a harmonic trap, because we feel that this approach gives more understanding of the phenomena. In addition, we also restrict ourselves to two dimensions, where the physics we are investigating is particularly clear. This geometry can be engineered by applying a sufficiently strong optical lattice in the z-direction which prevents hopping in that direction [39]. Also, a rapidly-rotating BEC can assume a similar geometry through centrifugal distortion of its density profile [35]. Furthermore, we restrict ourselves to the case where the rotation speed is tuned so that ν is a rational fraction, thus avoiding the commensurability issues which generically occur [28]. In the strong optical-lattice limit, the vortex lattice will share the geometry of the optical lattice [8, 27, 38].

As one approaches the superfluid-Mott boundary from weak coupling, the

vortex cores evolve from empty to containing the Mott phase [25]. This happens because when the superfluid order is suppressed in the vortex core, the Mott phase is energetically favorable compared to the vacuum. This raises the possibility that the energy of the vortex lattice will be reduced if the cores are centered on optical-lattice minima, "sites", rather than at the potential maxima, "plaquettes". A competing effect is that if the vortices are site-centered then the overlap of atomic wavepackets centered at neighboring sites will be reduced, raising the kinetic energy. We find that the interplay between these effects leads to a rich structure.

To model an infinite vortex-lattice we perform self-consistent Gutzwiller mean-field calculations on a two-dimensional square-lattice supercell made up of L sites per side, where each site is an optical-lattice potential minimum. We focus on the simplest case where each supercell contains one quantum of circulation, which produces a ground-state solution containing one singly-quantized vortex per supercell, and $\nu = \left(1/L^2\right)$. The Gutzwiller mean-field theory can be viewed as a variational calculation where one minimizes $\langle \hat{H}_{RBH} \rangle$ over the Gutzwiller product-states [9], $|\Psi\rangle = \prod_i \left(\sum_n f_n^i |n\rangle_i \right)$, where i is the site index, n is the particle number, and $|n\rangle_i$ is the n-particle occupation-number state at site i. Minimizing $\langle \hat{H}_{RBH} \rangle$ with respect to f_n^{i*} with the constraint $\sum_n |f_n^i|^2 - 1 = 0$ gives L^2 nonlinear eigenvalue equations, one for each site,

$$-t \sum_{k,\,\text{nn of } j} \left(\langle \hat{a}_k \rangle \sqrt{m} f_{m-1}^j R_{jk} + \langle \hat{a}_k^\dagger \rangle \sqrt{m+1} f_{m+1}^j R_{kj} \right) + \left(\frac{U}{2} m^2 - \left(\mu + \frac{U}{2} \right) m + \lambda_j \right) f_m^j = 0 \,, \tag{4.2}$$

where the sum is over all nearest neighbors of site j, m is the particle-number index, λ_j is a Lagrange multiplier, and $R_{jk} = \exp\left[i \int_{\vec{r}_k}^{\vec{r}_j} d\vec{r} \cdot \vec{A}(\vec{r}) \right]$, where $i = \sqrt{-1}$. We iteratively solve these equations: first choosing a trial order-parameter field $\left\{ \alpha_j^{(0)} \right\}$, where $\alpha_j = \langle \hat{a}_j \rangle$; then updating it by $\alpha_j^{(p)} = \sum_n \sqrt{n} f_{n-1}^{j*} \left(\left\{ \alpha_j^{(p-1)} \right\} \right) f_n^j \left(\left\{ \alpha_j^{(p-1)} \right\} \right)$,

where p is the iteration index. Similar calculations were performed by Oktel et. al. [40] (in a strip geometry) and Wu et. al. [25] (in a square geometry) to produce vortex lattices.

We perform calculations in the neighborhood of the $n = 1$ Mott phase, so the occupation-number distribution of each site will be peaked about 1, with small variance. Hence we only need to allow f_0^j, f_1^j and f_2^j to be nonzero. In most cases f_2^j and f_0^j will be much smaller than f_1^j. We find that using a larger occupation-number basis causes slight shifts of the boundary curves and the energy differences between plaquette- and site-centered vortex-lattice states, but the position of the Mott-lobe is unchanged. To model the infinite vortex lattice with our (LxL)–supercell we use magnetic boundary conditions [29, 30]

$$\alpha(x+L,y) = -\alpha(x,y)\exp\left[-i\frac{\pi}{L}(2y_0-y)\right], \tag{4.3}$$

$$\alpha(x,y+L) = -\alpha(x,y)\exp\left[+i\frac{\pi}{L}(2x_0-x)\right], \tag{4.4}$$

where $\alpha(x,y) = \langle \hat{a}_j \rangle$, and (x,y) are the Cartesian coordinates of site j, and (x_0, y_0) are free parameters which correspond to the coordinates of the vortex core in our supercell.

4.2.2 Results and discussion

The phase diagrams for $L = 1-4$ are displayed in Figure 4.1. Each phase plot has the familiar lobe-shaped Mott-insulator region in the deep-well limit, whose size varies as one changes n_v [23, 40]. We refer to the plaquette-centered vortex-lattice phase by the symbol P, and the site-centered vortex-lattice phase by the symbol S. As shown in these phase diagrams we find alternating bands of P and S. Moving from weak (large $\tilde{t}$) to strong coupling (small $\tilde{t}$) we find for $L = 1$: P;

Table 4.1: **Boundary curve spacings**. Separation between each structural boundary curve ($L = 1 - 4$) and its corresponding Mott lobe, quantified by $\Delta\tilde{t}$ at $\tilde{\mu} = \sqrt{2} - 1$ (the Mott-lobe tip, see Figure 4.1). Curve number 1 refers to the curve closest to the Mott lobe, curve number 2 is the next curve out, etc.

$L =$ / Curve number	2	3	4
1	0.034	0.00087	0.000017
2	—	0.012	0.0013
3	—	—	0.0046

$L = 2$: PS; $L = 3$: PSP; $L = 4$: $PSPS$; $L = 5$ (not pictured): $PSPSP$. The bands get very narrow as one increases L and as one approaches the Mott lobe. Table 4.1 gives the width of the various phases along the line $\tilde{\mu} = \tilde{\mu}_c$, where $\tilde{\mu}_c \left(= \sqrt{2} - 1\right)$ is the scaled chemical potential at the tip of the $n = 1$ Mott lobe.

There are several important features of these phase diagrams. First, the outermost vortex-lattice phase is always P, since a shallow optical-lattice potential pins vortices to the maxima of the potential. Second, for the values of L we have investigated, the phase diagram of a square vortex-lattice configuration characterized by $n_v = 1/L^2$ has L phase boundaries. Third, the innermost vortex-lattice phase alternates between P (odd L values) and S (even L values). And finally, the phase boundaries appear to share a universal hyperbolic shape. Although we have no explanation for the second observation, below we will explain the others.

We analyze the nature of the vortex-configuration phase transition by studying how the energy depends on the location of the vortex core in a single supercell. Figure 4.2 illustrates that the transitions are discontinuous. We quantify the

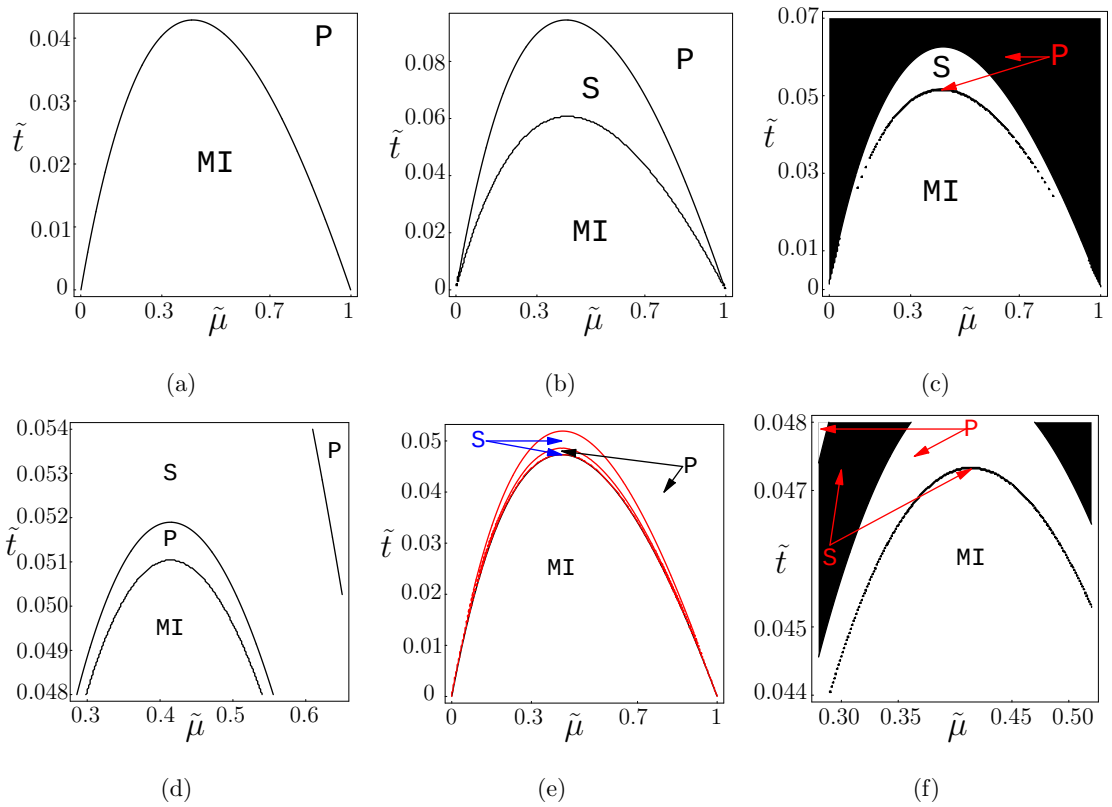

Figure 4.1: **Vortex structural phase plots**. (a)-(b) Structural phase plots for the cases $L = 1$ and $L = 2$, respectively. Dimensionless parameters $\tilde{t} = t/U$ and $\tilde{\mu} = \mu/U$ represent hopping amplitude and chemical potential, respectively, where each quantity is normalized by the on-site interaction. The plot labels *P*, *S* and *MI* refer to P-centered, S-centered and Mott-insulating phases, respectively. (c) The $L = 3$ phase plot, where shading is used to emphasize the thin reentrant P phase. (d) A closeup of the critical region of the Mott lobe in (c); the reentrant phase is more clearly resolved. (e) The $L = 4$ phase plot, on this parameter range, the inner structural-boundary curve cannot be discerned from the Mott lobe. (f) A closeup of the critical region of the Mott lobe in (e); shading is used to resolve the second reentrant phase region (S phase).

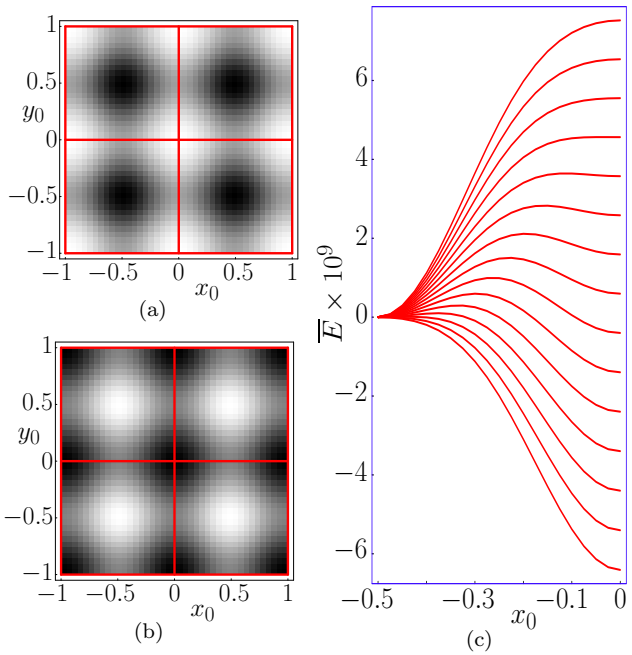

Figure 4.2: **Energy vs core-placement**. Vortex core position (x_0, y_0) in units of optical-lattice spacing with $(x_0, y_0) = (0, 0)$ corresponding to a vortex centered on a site, and $(x_0, y_0) = (0.5, 0.5)$ corresponding to a vortex centered on a plaquette. These plots correspond to the $L = 3$ recurrent phase boundary at $\tilde{\mu} = \sqrt{2} - 1$, and $0.0519 \leq \tilde{t} \leq 0.052$. In (a) ($\tilde{t} = 0.0519$) and (b) ($\tilde{t} = 0.052$) the vertices of the red (gray) lines are sites, and the plots are shaded so that darker (lighter) corresponds to lower (higher) energy. Plot (a) [(b)] corresponds to the P (S) state for $\tilde{t}$ just below (above) the boundary. (c) A composite of energy vs core-position curves on the diagonal line $y_0 = x_0 \in (-0.5, 0)$ (from plaquette to site), for $\tilde{t}$ between the spinodal points of the boundary. For each curve $\overline{E}(x_0) = [E(x_0) - E(-0.5)]/E_{\text{Mott}}$, where $E(x_0) = \langle \hat{H}_{RBH} \rangle (x_0)$. From top to bottom, this plot has 15 lines corresponding to $\tilde{t}_{\text{max}} = 0.051902$ and $\tilde{t}_{\text{min}} = 0.0519015$, with spacing $\Delta\tilde{t} = 7.5 \times 10^{-7}$.

Table 4.2: **Coexistence region widths**. Coexistence region widths, $\Delta\tilde{t}$, at $\tilde{\mu} = \sqrt{2} - 1$ (Mott-lobe tip) for the structural phase boundaries ($L = 1 - 4$). Widths are determined by finding the distance between spinodals. Curve number 1 refers to the boundary curve closest to the Mott lobe, curve number 2 is the next curve out, etc.

Curve number \ $L =$	2	3	4
1	0.014	7.5×10^{-6}	2.8×10^{-7}
2	—	0.0004	1.5×10^{-6}
3	—	—	2.5×10^{-5}

abruptness of the phase transition by measuring the width of the coexistence region; that is, we calculate the difference in $\tilde{t}$ (at fixed $\tilde{\mu}$) between spinodal points where each of the two energy minima disappear. As shown in Table 4.2, the coexistence region becomes thinner as L increases, and as the system moves toward the insulating phase.

The experimental consequences of our findings depend crucially on the energy difference of the two configurations. For example, the lattice will no longer be pinned if the temperature T exceeds this energy. On the line $\tilde{\mu} = \tilde{\mu}_c$ we plot these energies in Figure 4.3. The pinning energy decreases rapidly as L increases, and as the system approaches the insulating phase in parameter space. We find that the phases inside the outermost P phase all have tiny energy differences. To even see the $L = 2$ transition one requires a temperature below 0.15 nK. Hence our findings are mainly of academic interest. If the temperature is large compared with the pinning energy then the vortex configuration will be determined by the competition between vortex-vortex interaction, which favors a triangular vortex-lattice phase, and entropy, which favors a disordered

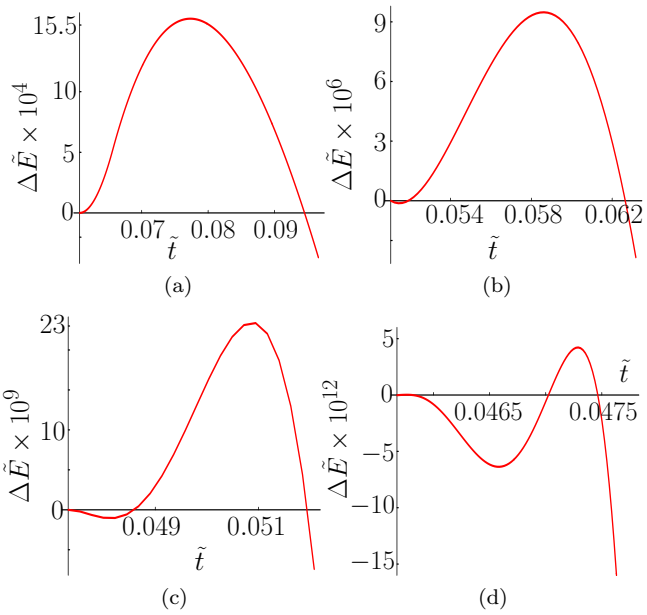

Figure 4.3: **Energy difference between P and S states**. Energy difference between P and S states with respect to $\tilde{t}$ at fixed values of L. (a)-(d) correspond to L=2-5, respectively. The dimensionless energy difference $\Delta\tilde{E} = (E_P - E_S)/U$, where $E_{P(S)} = \langle \hat{H}_{RBH} \rangle_{P(S)}$. The P-centered configuration is always favored in the outermost phase region. The energy differences decrease with decreasing n_v (increasing L), and also as the system approaches the insulating region (decreasing $\tilde{t}$). These numbers suggest that, in practice, a homogeneous vortex-lattice configuration is unlikely to be thermally stable in any of the inner phase regions.

vortex-liquid.

An additional concern is that the structures we find might be in part an artifact of the mean-field theory. Even if this is the case, we believe it is valuable to understand the structure of the mean-field theory. Furthermore, in the following sections we will give arguments which suggest that those results are more general. Finally, we note that experiments are currently far from the regime we consider.

4.3 Analytic theory near the Mott-boundary

Very near the Mott phase we can linearize Eq. (4.1) and analytically calculate the state of the system. During preparation of this paper, Umucahlar and Oktel [41] presented an independent study with substantial overlap of this section.

4.3.1 Reduced-basis *ansatz* and Harper's equation

It is simplest to illustrate this method by starting with the case of a uniform system which is not rotating ($\Omega = 0$). The expectation value of this Hamiltonian with respect to our Gutzwiller product state is

$$\langle \hat{H} \rangle / N = -\sigma \tilde{t} |\alpha|^2 + \frac{1}{2} \langle \hat{n}^2 \rangle - \left(\tilde{\mu} + \frac{1}{2} \right) \langle \hat{n} \rangle \,, \tag{4.5}$$

where σ is the number of nearest neighbors, and N is the total number of sites. As one approaches the n-particle Mott lobe we can, as before, make the *ansatz* that the single-site wavefunction is of the form $|\psi\rangle = f_{n-1}|n-1\rangle + f_n|n\rangle + f_{n+1}|n+1\rangle$, with $(f_{n-1}, f_n, f_{n+1}) = \left(\epsilon_1, \sqrt{1 - \epsilon_1^2 - \epsilon_2^2}, \epsilon_2 \right)$, where ϵ_i are small. One can readily verify that the terms neglected in this *ansatz* are of higher order in ϵ. Minimizing $\langle \hat{H} \rangle$ one finds that the chemical potential at which ϵ_i becomes nonzero is

$$\tilde{\mu}_\pm = \left(n - \frac{1}{2} (1 + \sigma \tilde{t}) \right) \pm \sqrt{\frac{1}{4} \sigma^2 \tilde{t}^2 - \left(n + \frac{1}{2} \right) \sigma \tilde{t} + \frac{1}{4}} \,. \tag{4.6}$$

In particular, the tip of the Mott Lobe is at $\tilde{\mu}_c = \sqrt{n(n+1)} - 1$, $\sigma \tilde{t}_c = \left[2n + 1 + 2\sqrt{n(n+1)} \right]^{-1}$.

Adding rotation, the energy divided by U is

$$\langle \hat{H}_{RBH} \rangle = -\sum_{\langle i,j \rangle} \left(\tilde{t}_{ij} \alpha_i^* \alpha_j + c.c. \right) + \sum_i \left(\frac{1}{2} \langle \hat{n}_i^2 \rangle - \left(\tilde{\mu} + \frac{1}{2} \right) \langle \hat{n}_i \rangle \right) , \tag{4.7}$$

where $\tilde{t}_{ij} = \tilde{t}\exp\left[i\pi\nu\int_{\vec{r}_j}^{\vec{r}_i}(x\hat{y}-y\hat{x})\cdot d\vec{r}\right]$. Again, near the Mott lobe we write

$$\left(f^i_{n-1}, f^i_n, f^i_{n+1}\right) = \left(\lambda^i\overline{\alpha}^*_i, \sqrt{1-|\overline{\alpha}_i|^2\left(|\lambda^i|^2+|\lambda^i_1|^2\right)}, \lambda^i_1\overline{\alpha}_i\right) \tag{4.8}$$

where $\alpha = \overline{\alpha} + O\left(\overline{\alpha}^3\right)$, and $\lambda^i_1 = \frac{1}{\sqrt{n+1}}\left(1-\sqrt{n}\lambda^i\right)$. Note that unlike our previous calculations, we do not need to restrict $n_\nu = \nu$.

Next we minimize with respect to λ^i to find

$$\langle\hat{H}_{RBH}\rangle = -\sum_{\langle i,j\rangle}\left(\tilde{t}_{ij}\alpha^*_i\alpha_j + c.c.\right) + \frac{n-\tilde{\mu}}{n+1}\left(1-n\frac{n-\tilde{\mu}}{1+\tilde{\mu}}\right)\sum_i|\alpha_i|^2 + E_{\text{Mott}}\,, \tag{4.9}$$

where E_{Mott} is the energy-per-site of the n-particle Mott state, and we have neglected terms of order α^3. Next we minimize with respect to α^*_k. In the case of the 2D square lattice we arrive at a symmetric-gauge Harper's equation [26],

$$\begin{aligned} &-\alpha(x+1,y)\exp[i\pi\nu y] - \alpha(x-1,y)\exp[-i\pi\nu y] - \alpha(x,y+1)\exp[-i\pi\nu x] \\ &-\alpha(x,y-1)\exp[+i\pi\nu x] + \epsilon\alpha(x,y) = 0\,, \end{aligned} \tag{4.10}$$

where

$$\epsilon = \frac{1}{\tilde{t}}\frac{n-\tilde{\mu}}{n+1}\left(1-n\frac{n-\tilde{\mu}}{1+\tilde{\mu}}\right). \tag{4.11}$$

A simple gauge transformation, $\tilde{\alpha}_j = \alpha_j\exp\left[-i\pi\nu\int_{\vec{r}_j}^{\vec{r}_k}(x\hat{y}+y\hat{x})\cdot d\vec{r}\right]$ along with the assumption that $\tilde{\alpha}(x,y) = \exp(i\gamma)\beta(x)$, brings Eq. (4.10) into the more familiar form

$$\beta(x+1)+\beta(x-1)+2\cos(2\pi\nu x-\gamma)\beta(x) = \epsilon\beta(x)\,, \tag{4.12}$$

where the circulation density $\nu = p/q$ is a rational fraction, and γ is a wavevector set to $\pi/2q$ in Ref. [26]. The eigenvalue spectrum of Eq. (4.10) has an intricate fractal-structure known as the Hofstadter butterfly [26].

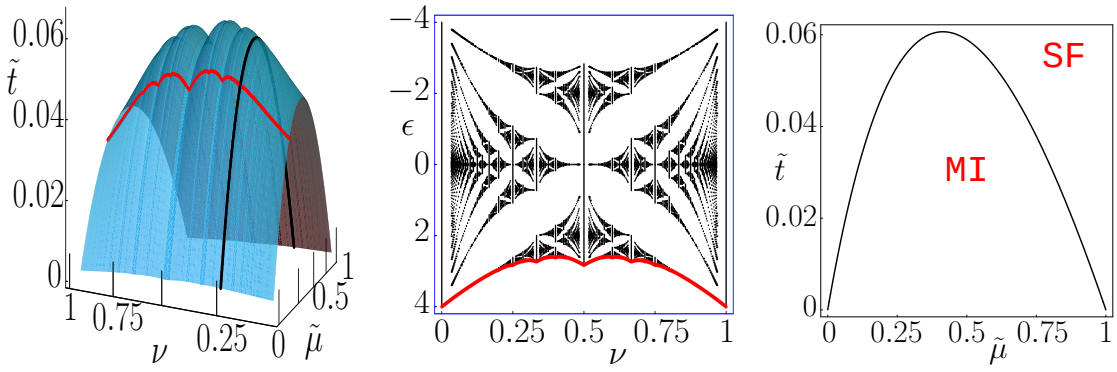

(a) (b) (c)

Figure 4.4: **The Mott boundary and the Hofstadter butterfly**. The blue (light gray) surface in (a) is the mean-field Mott boundary of the Bose-Hubbard model at zero temperature for chemical potential $\tilde{\mu} = \{0, 1\}$, and circulation-quanta per optical-lattice site $\nu = \{0, 1\}$. The red (dark gray) curve on this surface [and outlining the bottom edge of the spectrum in (b)] demonstrates how, at fixed $\tilde{\mu}$ (the value in the Figure is $\tilde{\mu} = 0.2$), the value of $\tilde{t}$ is inversely related to the edge eigenvalues of the Hofstadter butterfly spectrum shown in (b). The black curve on the boundary surface [and in (c)] demonstrates how, at fixed ν (in this case $\nu = 1/4$), the value of $\tilde{t}$ is just a familiar Mott-lobe boundary in the $(\tilde{t}, \tilde{\mu})$-plane, as shown in (c).

Fixing ν and $\tilde{\mu}$, the corresponding point on the Mott lobe is the smallest $\tilde{t}$ for which Eq. (4.11) is an eigenvalue of Eq. (4.10). This condition is satisifed by the largest eigenvalue $\epsilon = \epsilon_{\text{edge}}(\nu)$ of Eq. (4.10). We call this largest eigenvalue the *edge eigenvalue*. The Mott boundary is then given by

$$\tilde{t} = \frac{1}{\epsilon_{\text{edge}}[\nu]} \frac{n - \tilde{\mu}}{n + 1} \left(1 - n \frac{n - \tilde{\mu}}{1 + \tilde{\mu}}\right), \tag{4.13}$$

where n is the integer corresponding to the total-particle density in the Mott lobe. This remarkable relationship is illustrated in Figure 4.4. In the non-rotating case we find $\epsilon_{\text{edge}}[\nu = 0] = 4$, and Eq. (4.13) reduces to Eq. (4.6).

The eigenvectors of Harper's equation have rich topologies. The highest

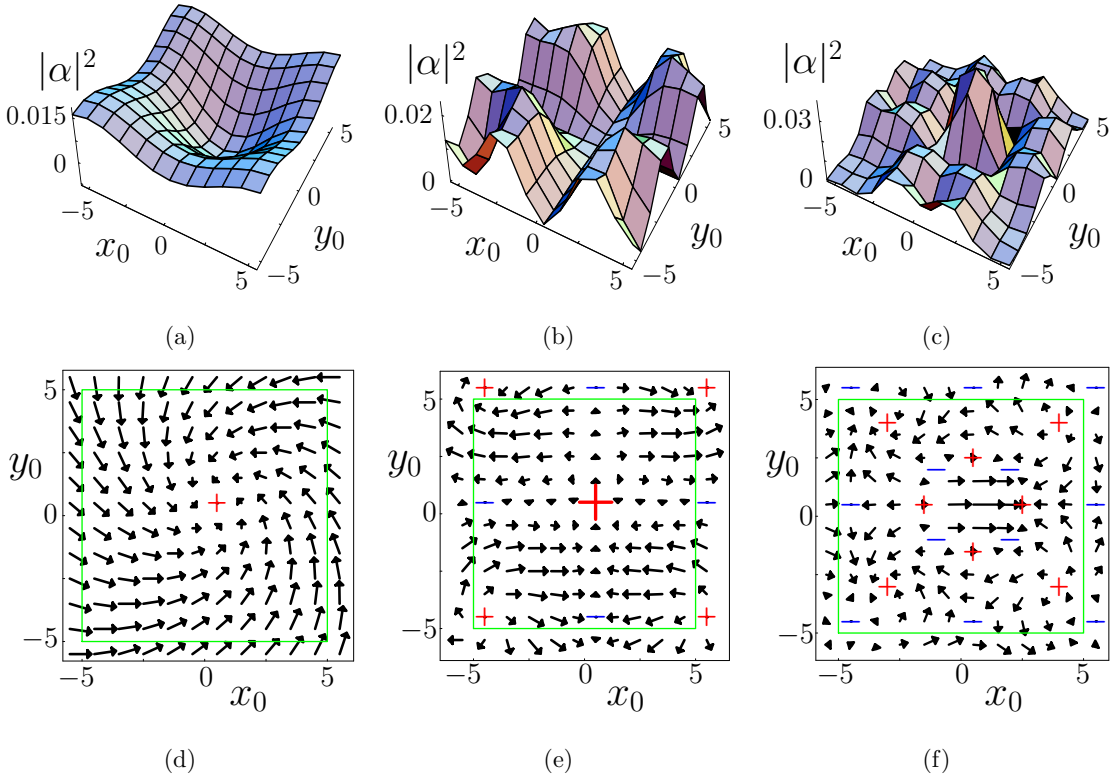

Figure 4.5: **Hofstadter butterfly eigenvectors**. Hofstadter butterfly eigenvectors for $\nu = 1/100$ in a 10x10 supercell. The position coordinates (x_0, y_0) are in units of the optical lattice spacing, and the order parameter density $|\alpha|^2$ is normalized so that over a single supercell $\sum_{(x_0,y_0)}|\alpha(x_0,y_0)|^2 = 1$. The bands are indexed with $n = 1$ for smallest central-eigenvalue, $n = 2$ for next smallest, etc. (a)-(c) Plots of order-parameter density $|\alpha|^2$ for bands $n = 100$, $n = 97$ and $n = 91$ respectively. (d)-(f) The corresponding complex-phase fields. At each site is the base of an arrow pointing in the direction $(Re[\alpha], Im[\alpha])$, and with length proportional to $|\alpha|$. Positively (negatively) charged vortices are labeled with a red "+" (blue "−"). The green boundary encloses one unit cell. The size and shape of this boundary are fixed, but varying ϵ will shift its position. The $n = 100$ plot has a single vortex with charge +1. The $n = 97$ state has a central doubly-quantized vortex of charge 2, connected by domain walls to vortices of charge −1 near the faces of the cell. Vortices of charge +1 lie near the corners. The $n = 91$ pattern contains 8 "+"–vortices and 7 "−"–vortices in each unit cell.

band (corresponding to the largest ϵ's) contains states with regular arrays of singly quantized vortices. Changing ϵ continuously changes the location of the vortices relative to the lattice. The lower bands include states with more complicated structures with multiple vortices of opposite signs. Also, the band structure is symmetric with respect to reflection about $\epsilon = 0$. Illustrative structures are shown in Figure 4.5.

The edge state corresponds to an array of singly quantized vortices. For $\nu = 1/L^2$ we find that for even or odd L these vortices are site-centered or plaquette-centered, respectively. This explains our previous observation of alternating vortex-lattice phases corresponding to even and odd L values.

4.3.2 Discussion

Why does the Hofstadter butterfly, a pattern associated with noninteracting particles, appear near the Mott lobe, where the interactions are strong? The answer is that near the Mott-lobe boundary most of the atoms are static, with only a dilute gas of mobile particles and/or holes. The diluteness of these excitations leads to single-particle physics.

It should be noted that this explanation does not depend on the approximations of mean-field theory. Even including fluctuations, near the Mott lobe (with the exception of the region immediately about the tip), the system is described by a weakly-interacting gas of excitations [23, 42]. Thus it is unlikely that the structural transitions we find are an artifact of mean-field theory. Interactions between the excitations can be included in our mean-field theory by including higher-order terms in equation (4.9). If one approximates $\langle \hat{n}_i^2 \rangle = |\alpha_i|^4$, one recov-

ers a nonlinear Schrödinger equation

$$-\sum_{\text{j, nn of k}}\left(\alpha_j \exp\left[i\pi\nu\int_{\vec{r}_j}^{\vec{r}_k}(x\hat{y}-y\hat{x})\cdot d\vec{r}\right]\right)+|\alpha_k|^2\alpha_k+\frac{\mu}{t}\alpha_k=0\,. \tag{4.14}$$

We should mention that one can also study Hofstadter butterfly physics far from the Mott lobe by using a Feshbach resonance [10] to tune the interaction of a gas of bosons trapped in a deep, rotating optical lattice. Merely reducing the lattice strength is probably insufficient, as the tight-binding approximation is apt to break down.

4.4 Summary

We have analyzed vortex-lattice phases in a deep optical-lattice potential using the mean-field theory of the rotating Bose-Hubbard Model in a two-dimensional square-lattice at zero temperature. We observed several transitions between site-centered and plaquette-centered vortex states. For the (L x L)-supercell calculation (corresponding to $n_v = 1/L^2$) there are L boundary curves – $L-1$ structural curves, and the Mott lobe. We found that the structural transitions are discontinuous, and we quantify trends in the widths of the corresponding coexistence regions as well as trends in the spacing of the structural boundary lines in parameter space. The boundary curves share a universal hyperbolic shape.

We also carried out an analytic study where we determined that the linear eigenvalue equation characterizing the Mott lobe also characterizes the Hofstadter butterfly spectrum. From this we determined an expression for the Mott-lobe boundary. This linearized analysis confirmed the vortex-core placement found in our numerical study.

CHAPTER 5

VORTICES NEAR THE MOTT PHASE OF A TRAPPED BOSE-EINSTEIN CONDENSATE

The contents of this chapter are adapted from work originally archived online as *Vortices near the Mott phase of a trapped Bose-Einstein condensate*, arXiv:0808.1548v1; and submitted for publication in *Physical Review Letters*.

In this chapter we present a theoretical study of vortices within a harmonically trapped Bose-Einstein condensate in a rotating optical lattice. We find that proximity to the Mott insulating state dramatically affects the vortex structures. To illustrate we give examples in which the vortices: (i) all sit at a fixed distance from the center of the trap, forming a ring, or (ii) coalesce at the center of the trap, forming a giant vortex. We model time-of-flight expansion to demonstrate the experimental observability of our predictions.

5.1 Introduction

Atomic clouds in a rotating optical lattice are at the intellectual intersection of several major paradigms of condensed matter physics. These rotating clouds may display a superfluid-insulator quantum phase transition [12], vortex pinning [8, 27], frustration [43], Josephson junction physics [44], and even analogs of the fractional quantum Hall effect [45]. Here we explore the theory of vortices in such systems, showing how proximity to the Mott insulator phase impacts the vortex configurations.

Considering a uniform gas of atoms of mass m in an optical lattice rotat-

ing with frequency Ω, there are three macroscopic length scales in the problem: the lattice spacing d, the magnetic length $\ell = \sqrt{\hbar/m\Omega}$, and the particle spacing $n^{-1/3}$, where $\hbar = h/2\pi$ is Planck's constant. Even without interactions, the commensurability of these lengths leads to nontrivial physics – the single particle spectrum, the Hofstadter butterfly, is fractal [26]. For interacting bosons, this fractal spectrum leads to a modulation of the boundary between superfluid and Mott insulating phases [41, 46]. Further, the vortices in a superfluid on a rotating lattice develop extra structure: their cores may fill with the Mott state [25], changing which vortex arrangements minimize the energy [46].

We consider a harmonically trapped superfluid gas on a rotating optical lattice in the single-band tight binding-limit close to the Mott state. We choose to study a two-dimensional cloud, as it provides the simplest setting for investigating vortex physics, and is an experimentally relevant geometry [13]. The proximity to the Mott state results in a nontrivial spatial dependance of the superfluid order parameter, and drives a rearrangement of vortices.

A similar geometry was realized in a recent experiment [28], with the caveat that their shallow optical lattice had such a large lattice spacing that they were not able to reach the tight binding limit. In principle their technique can be refined to explore the physics that we describe here. The tight binding limit may also be reached through quantum optics techniques which introduce phases on the hopping matrix elements for atoms in a non-rotating lattice [47, 48, 49, 50].

5.2 Model and calculation

In the rotating frame our system is described by the rotating Bose-Hubbard hamiltonian [9, 25]:

$$\hat{H} = -\sum_{\langle i,j \rangle} \left(t_{ij} \hat{a}_i^\dagger \hat{a}_j + h.c. \right) + \sum_i \left(\frac{U}{2} \hat{n}_i \left(\hat{n}_i - 1 \right) - \mu_i \hat{n}_i \right) \tag{5.1}$$

where $t_{ij} = t \exp\left[i \int_{\vec{r}_j}^{\vec{r}_i} d\vec{r} \cdot \vec{A}(\vec{r}) \right]$ is the hopping matrix element from site j to site i. The rotation vector potential, which gives rise to the Coriolis effect, is $\vec{A}(\vec{r}) = (m/\hbar)\left(\vec{\Omega} \times \vec{r}\right) = \pi\nu\,(x\hat{y} - y\hat{x})$, where ν is the number of circulation quanta per optical-lattice site. The local chemical potential $\mu_i = \mu_0 - m\left(\omega^2 - \Omega^2\right) r_i^2/2$ includes the centripetal potential. In these expressions, μ_0 is the central chemical potential, ω is the trapping frequency, $\vec{r}_i$ is the position of site i, $\hat{a}_i^\dagger$ ($\hat{a}_i$) is a bosonic creation (annihilation) operator, $\hat{n}_i = \hat{a}_i^\dagger \hat{a}_i$ is the particle number operator for site i, and U is the particle-particle interaction strength. The connection between these parameters and experiment are given by Jaksch et al. [9]. Here, and in the rest of the paper, we use units where the lattice spacing is unity.

Both the superfluid and Mott insulator can be approximated by a spatially inhomogeneous Gutzwiller product *ansatz* [9], $|\Psi_{GW}\rangle = \prod_{i=1}^{M} \left(\sum_n f_n^i |n\rangle_i \right)$, where i is the site index, M is the total number of sites, $|n\rangle_i$ is the n-particle occupation-number state at site i, and f_n^i is the corresponding complex amplitude, with $\sum_n |f_n^i|^2 = 1$. Despite the limitations of being a mean-field theory, the Gutzwiller approach compares well with exact methods, and strong coupling expansions [23, 42, 51]. It has also been used extensively to understand experimental results [12, 52, 53], and is well suited for studying the vortex physics that we consider here.

Using $|\Psi_{GW}\rangle$ as a variational *ansatz*, we minimize the energy with respect to

the $\{f_n^i\}$. We then extract the density $\rho_i = \sum_n n|f_n^i|^2$ and the condensate order parameter $\alpha_i = \langle \hat{a}_i \rangle = \sum_n \sqrt{n} \left(f_{n-1}^i \right)^* f_n^i$ at each site. The condensate density $\rho_i^c = |\langle \hat{a}_i \rangle|^2$ is equal to the superfluid density in this model, and is generally not equal to the density.

We use an iterative algorithm to determine the $\{f_n^i\}$ which minimize the energy. We use a square region with L sites per side and hard boundary conditions. We find that we must take L much larger than the effective cloud diameter so that our solutions do not depend on those boundaries. Typically we use $40 \leq L \leq 90$. For the simulation described in Figure 1 we impose four-fold rotational symmetry, but from unconstrained simulations on smaller clouds we find that this constraint does not significantly change the phenomena. Similar calculations were performed by Scarola and Das Sarma [54] to analyze the case where the single-particle Mott state is surrounded by a rotating superfluid ring.

Since this mean-field theory is highly nonlinear we find that the iterative algorithm often converges to different solutions depending on the initial state we use. For the results shown here we first iterate to self-consistency in a parameter region where the solution is unique, then slowly change parameter values, using the result from the previous parameters as a seed. One should see analogous results in an experiment where one adiabatically changes parameters. As in such experiments [55] we observe hysteresis.

5.3 Results

We have performed a thorough investigation of a wide range of parameters and, as one would expect, we find that a basic understanding of the trapped gas

can be extracted from the phase diagram of the homogeneous system, where $\Omega = \omega = 0$ [Figures 1(a) and 2(a)]. For a sufficiently gentle trap, the gas looks locally homogeneous, and its density at any point r can be approximated by that of a uniform system with chemical potential $\mu(r) = \mu_0 - V(r)$. As a general rule, nontrivial vortex structures appear when the LDA superfluid density deviates significantly from a typical Thomas-Fermi profile. The vortices tend to move to regions where there is a local suppression of the superfluid density.

We illustrate this principle with two examples: in Figure 5.1 we study the case where the superfluid density has a ring-shaped plateau, and in Figure 5.2 we consider the case where a Mott region sits in the center of the cloud.

5.4 Ring vortex configuration

We begin with the nonrotating configuration illustrated by the left half of the Subfigures in Figure 1 (with $t/U = 0.06, \mu_0/U = 0.7$). There is a plateau in the superfluid density but not in the total density, and the phase of the superfluid order parameter is uniform. Starting from this non-rotating configuration we gradually increase the rotation speed to $\nu = 0.04$, iterating to self-consistency at each step. Rather than forming a lattice, the resulting vortices form a ring around the central ρ^c peak in Figure 1(d). This configuration is favored because it minimizes the sum of competing energy costs: the rotation favors a uniform distribution of vortices, but the single vortex energy is smallest where ρ^c is low.

As seen in Figure 1(c), the phase of the superfluid inside the ring is essentially constant. This can be understood by an analogy with magnetostatics. The velocity $\vec{v}$ obeys an analog of Ampere's law $\oint \vec{v} \cdot d\vec{\ell} = (h/m)N_v$, where N_v, the

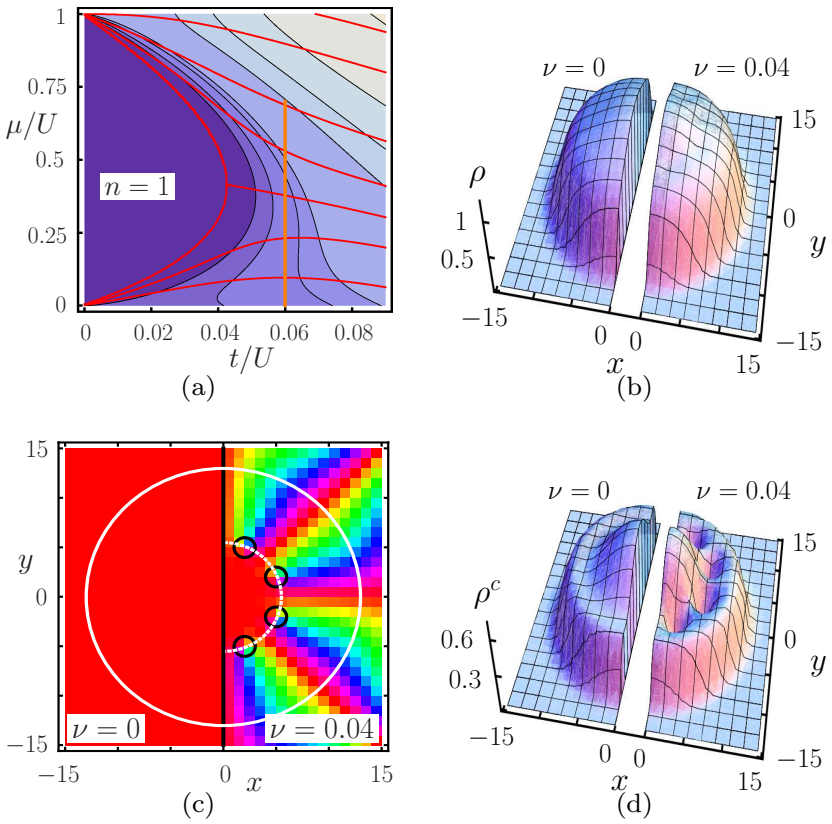

Figure 5.1: **Ring vortex configuration**. Comparison between non-rotating ($\nu = 0$) and rotating ($\nu = 0.04$) states of a system characterized by $(t/U = 0.06, \mu_0/U = 0.7)$. (a) Mean-field phase plot of the uniform Bose-Hubbard model. Contours of fixed ρ and ρ^c, are indicated by red and black curves. The superfluid density vanishes in the single-particle Mott region labeled "$n = 1$", and increases with lightening shades of purple. The vertical orange line represents the LDA parameter-space trajectory for the current system. (b) [(d)] Comparison of density [condensate density]. (c) Comparison of order parameter complex phase field. The complex phase is represented by "Hue". Solid and dotted white lines are a guide to the eye. Black circles enclose singly-quantized vortices. As seen in (c) and (d), vortices form in a circular pattern on the condensate density plateau; the density (b) changes only slightly due to rotation.

number of vortices enclosed in the contour of integration, plays the role of the enclosed current. Neglecting the discreteness of the vortices in the ring, the fluid inside is motionless, while the fluid outside moves as if all the vortices were at the geometric center of the cloud. Even with only eight vortices our system appears to approach this limit. If one increases the rotation speed, one can find a state with several concentric rings of vortices in the plateau. Similarly, increasing μ_0/U can can lead to multiple superfluid plateaus, each of which may contain a ring of vortices. This structure of nested rings of vortices is reminiscent of Onsager and London's original proposal of vortex sheets in liquid helium [56].

5.5 Giant vortex

Our second example of nontrivial vortex structures is illustrated in Figure 5.2, where the LDA predicts a superfluid shell surrounding a Mott core. Rather than forming a lattice of discrete vortices, one expects that this system will form a "giant" vortex [7] when rotated: the vortices occupying the Mott region, leaving a persistent current in the superfluid shell. The energy barriers for changing vorticity are particularly high, so we generate the rotating state in two stages. We start with a non-rotating system ($\nu = 0$) at weak coupling ($t/U = 0.2, \mu_0/U = 0.3$), gradually increasing the rotation to $\nu = 0.032$, where we find the square vortex lattice illustrated in Figures 2(b – left) and (d). We then adiabatically reduce t/U from 0.2 to 0.03. As we reduce t/U, the central ρ^c drops, while ρ approaches unity there. Eventually we see a Mott regime at the center of the cloud. During the evolution, we find that 8 of the vortices escape from the edge of the trap, while four of the vortices coalesce at the center of the trap and effectively form a vortex of charge 4. Such a dense packing of vorticity would be unstable in the

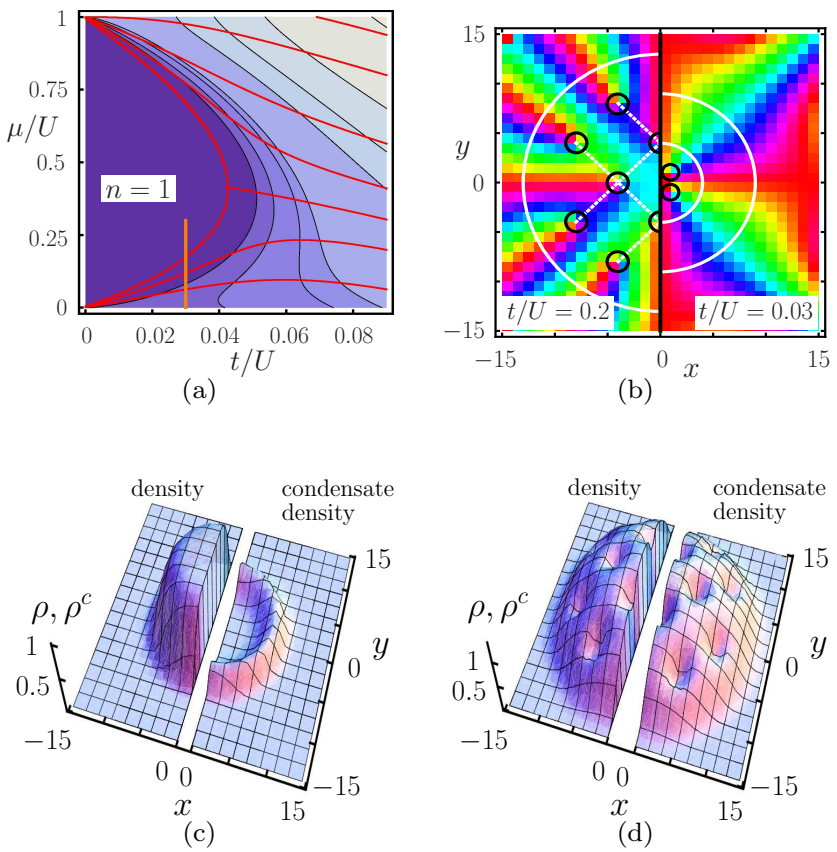

Figure 5.2: **Giant vortex**. Comparison of a vortex lattice far from the Mott regime ($t/U = 0.2$) and a giant vortex system where the Mott phase occupies the center of the cloud ($t/U = 0.03$). (a) Mean-field phase plot for the uniform Bose-Hubbard model with vertical orange parameter-space trajectory representing a system with ($t/U = 0.03$, $\mu_0/U = 0.3$). (b) Comparison of order parameter complex phase fields. (c) [(d)] Comparison of density and condensate density where $t/U = 0.03$ [$t/U = 0.2$].

absence of the optical lattice. For larger systems with higher rotation rates one finds giant vortices with larger circulation.

Due to its multiply connected topology, a ring, such as the one formed here, is one of the archetypical geometries used in theoretical discussions of superfluidity [57, 58, 59]. There are several experimental schemes for creating a ring-shaped trap [60], and many theoretical studies of giant vortex formation stabi-

lized by a quadratic-plus-quartic potential [61, 62, 63, 64]. Here the multiply connected geometry is spontaneously formed by the appearance of the Mott state in the center of the cloud. As was found by Scarola and Das Sarma [54], this Mott region effectively pins the vortices to the center.

By changing t/U one may study a few other interesting structures. For example, one can engineer a situation where a central superfluid region is surrounded by a Mott ring followed by a superfluid ring. At appropriate rotation speeds one produces a configuration which has properties of both the states seen in Figure 5.1 and in Figure 5.2. One will find no vortex cores (all of the vorticity is confined to the Mott ring), the central region will be stationary, and the outer region rotates.

Another interesting limit is found when one decreases the thickness of a Mott/superfluid region so much that it breaks up into a number of discrete islands. Small Mott islands act as pinning centers, while small superfluid islands form an analog of a Josephson junction array [65].

5.6 Detection

Vortex structures near the Mott limit may be hard to detect using *in-situ* absorption imaging. As is exemplified by Figure 1(b), the vortices do not necessarily have a great influence on the density of the cloud. This is principally because near the Mott boundary the superfluid fraction becomes small: even though the superfluid vanishes in the vortex core, the corresponding density may not appreciably change. Two other pieces of physics also influence the visibility. First, near the Mott boundary one can produce vortices with Mott cores [25].

Depending on the bulk density, this can lead to vortices where there is no density suppression at all, or even a density enhancement. Second, the lengthscale of the vortex core, the superfluid healing length, varies with U/t. For both very large and small U/t the healing length is large, while at intermediate couplings it is comparable to the lattice spacing, possibly below optical resolution.

We argue that the vortex structures will be much more easily imaged after time-of-flight (TOF) expansion of the cloud for time $\bar{t}$ [32]. The density after TOF expansion is made of two pieces – a largely featureless incoherent background from the normal component of the gas, and a coherent contribution from the superfluid component. The coherent contribution forms a series of Bragg peaks [12], where each peak reflects the Fourier transform of the superfluid order parameter. Neglecting interactions during time-of-flight, and using Gaussian initial states at each lattice site, we calculate the TOF column density. In the long time limit $D_{\bar{t}} \gg R_{TF}$, where $D_{\bar{t}} = \hbar\bar{t}/m\lambda$, R_{TF} is the radius of the initial cloud, and λ is the size of each initial Wannier state, the column density of the expanding cloud is

$$n(\vec{\boldsymbol{r}}, \bar{t}) = \rho(r, \bar{t}) \left[(N - N_c) + |\Lambda(\vec{\boldsymbol{r}}, \bar{t})|^2 \right] \tag{5.2}$$

$$\rho(r, \bar{t}) = \left(\pi D_{\bar{t}}^2 \right)^{-1} e^{-r^2/D_{\bar{t}}^2} \tag{5.3}$$

$$\Lambda(\vec{\boldsymbol{r}}, \bar{t}) = \sum_j \alpha_j e^{-i\vec{\boldsymbol{r}}\cdot\vec{\boldsymbol{r}}_j/D_{\bar{t}}\lambda}, \tag{5.4}$$

where N and N_c are the total number of particles and condensed particles, respectively.

The incoherent contribution $(N - N_c)\rho(r, \bar{t})$ is simply a Gaussian. This is a consequence of the Gutzwiller approximation, which neglects short range correlations. Adding these correlations would modify the shape of the background, but it will remain smooth. The coherent part has much more structure. Fig-

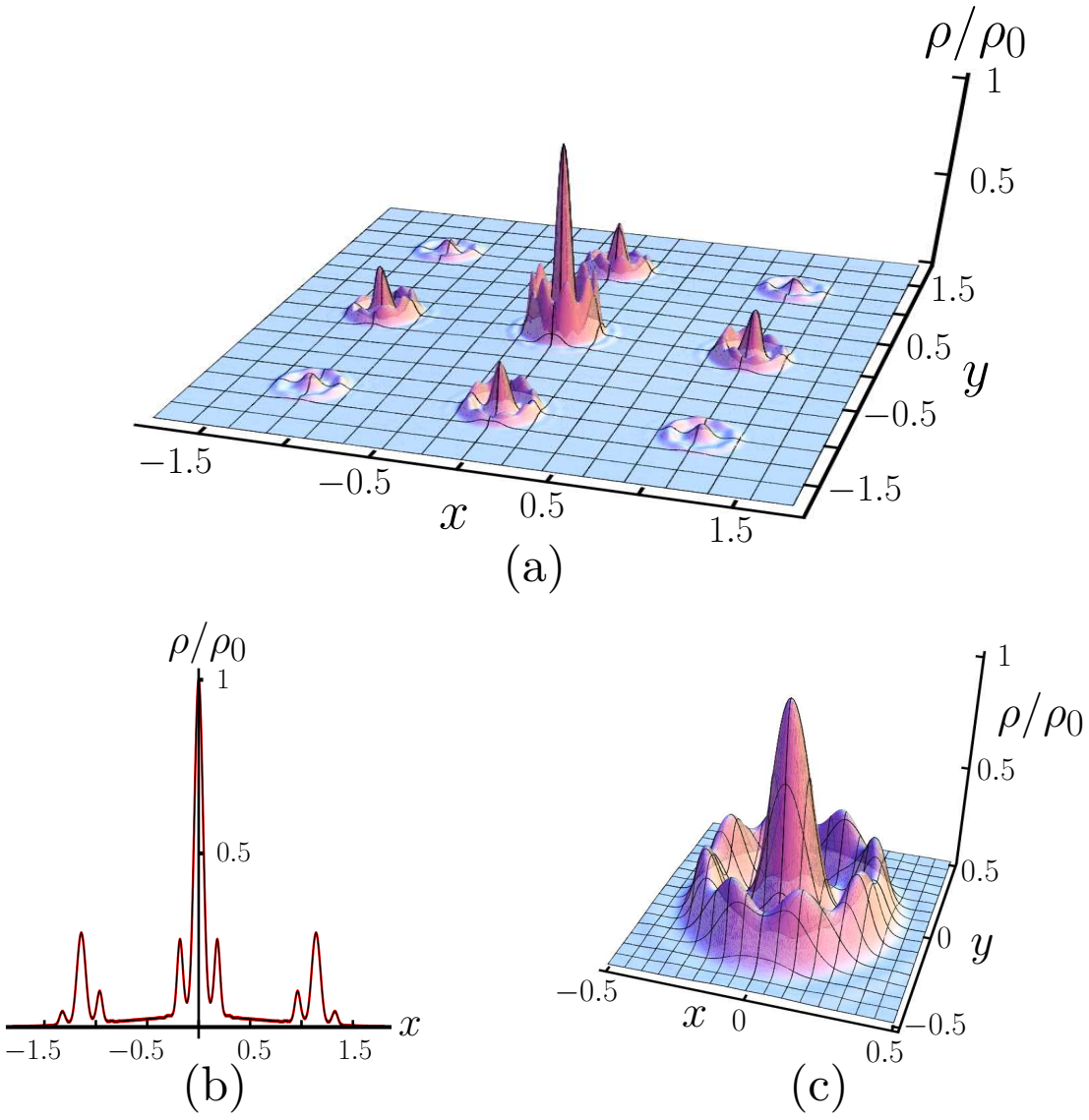

Figure 5.3: **Time-of-flight expansion**. (a) Column density ρ scaled by the central column density ρ_0 as a function of space for the ring configuration vortex state in Figure 5.1 after expanding for time $\bar{t}$. Positions are measured in terms of scaling parameter $D_{\bar{t}} = \hbar\bar{t}/m\lambda$, where λ is the initial extent of the Wannier wavefunction. (b) One dimensional cut through center of (a). Note the incoherent background between the Bragg peaks. (c) Close-up of the central Bragg peak, corresponding to the Fourier transform of the superfluid order parameter. The 8 dips in the outer crest result from the 8 vortices in the initial state.

ure 5.3 illustrates the density pattern which will be seen if the rotating cloud in Figure 5.1 is allowed to expand.

CHAPTER 6

COMMENSURABILITY AND HYSTERETIC EVOLUTION OF VORTEX CONFIGURATIONS IN ROTATING OPTICAL LATTICES

The contents of this chapter are adapted from work originally archived as *Commensurability and hysteretic evolution of vortex configurations in rotating optical lattices*, arXiv:0809.2078; and submitted for publication in *Physical Review A*.

In this chapter we present a theoretical study of vortices within a harmonically trapped Bose-Einstein condensate in a rotating optical lattice. Due to the competition between vortex-vortex interactions and pinning to the optical lattice we find a very complicated energy landscape, which leads to hysteretic evolution. The qualitative structure of the vortex configurations depends on the commensurability between the vortex density and the site density – with regular lattices when these are commensurate, and concentric rings when they are not. We model the imaging of these structures by calculating time-of-flight column densities. As in the absence of the optical lattice, the vortices are much more easily observed in a time-of-flight image than *in-situ*.

6.1 Introduction

Atomic clouds in rotating optical lattices have garnered a large amount of interest from researchers in the fields of condensed matter physics, atomic physics, and quantum optics. An optical lattice simulates the periodic potential ubiquitous in solid state physics, while rotation probes the superfluid character of these cold atomic gases by driving the formation of quantized vortices. Here

we explore the theory of vortices in an optical lattice. Specifically, we investigate the evolution of the vortex configurations that occur in the single-band tight-binding limit as the rotation rate is slowly varied. The energy landscape has a complicated topography that leads to hysteresis. The vortex configurations depend on commensurability of several different length scales.

A uniform gas of atoms of mass m in an optical lattice rotating with frequency Ω is characterized by several important scales. Among these are the on-site interaction U, the lattice spacing d, the magnetic length $\ell = \sqrt{\hbar/m\Omega}$, and the particle density n, where $\hbar = h/2\pi$ is Planck's constant. The behavior of the system changes when these various scales form different commensurate ratios. There are three well known examples of such commensurability effects, namely when $d^2/\pi\ell^2$ is rational for a two dimensional noninteracting gas, when nd^D is an integer of a non-rotating gas in dimension D, or when $\pi n\ell^2$ is rational for a two-dimensional lattice-free gas. The first example gives the Hofstadter butterfly single-particle spectrum [26], the second the superfluid-Mott transition, and the third the fractional quantum Hall effect. Here we explore how the commensurability between ℓ and d plays out in an interacting superfluid, away from the Mott [41, 46, 66] and fractional quantum Hall limits [36, 45, 48, 49, 50, 67, 68].

We study the vortex configurations that emerge in a harmonically trapped atomic cloud inside a rotating optical lattice in the single-band tight-binding limit. The resulting phenomenology is rich, as the vortex configurations depend on a number of factors, including: the vortex-vortex interaction, the vortex-pinning potential due to the optical lattice, the finite cloud size, and the past history of the cloud. Fast enough rotation of a uniform superfluid results in the formation of an array of quantized vortex lines of cross-sectional density n_{vor},

corresponding to a mean intervortex spacing of $n_{vor}^{-1/2} = \ell/\sqrt{\pi}$. In an infinite system, these vortices arrange themselves in a triangular lattice configuration, but a finite cloud size produces distortions [69, 70, 71, 72, 73, 74, 75]. A co-rotating optical lattice introduces a vortex-pinning potential with minima at the optical lattice potential maxima (between the occupied sites). For commensurate vortex densities, this pinning can cause the lowest energy configuration to switch from a triangular vortex lattice, to one that shares the geometry of the optical lattice [8, 25, 27, 28, 76, 77]. In practice the vortices are insufficiently mobile to find the true ground state, and one typically sees some metastable configuration, for example with a number of domains separated by defects. We present a realistic simulation of these effects.

We perform calculations in two-dimensions, modeling a harmonically trapped gas of bosons in a rotating square lattice. The two-dimensional case is convenient because we can then concentrate on the interaction between vortex cores in a single plane. This is also an experimentally relevant geometry, as the dimensionality of the system can be controlled by using an anisotropic harmonic potential, or optical lattice, where the hard trapping direction is along the rotation axis of the optical lattice [13]. A recent experiment [28] realized exactly this scenario by placing a rotating mask in the Fourier plane of a laser beam which forms an optical dipole trap. The mask contained three/four holes, producing a triangular/square lattice in the image plane, where the atoms were trapped. The lattice spacing was large due to the nature of their optics but can in principle be made small enough to explore the single-band tight-binding limit that we investigate. A similar setup, using a dual-axis acousto-optic deflector, promises to reach this limit in the near future [78].

We find hysteresis in our numerical algorithm, reflecting the complicated energy landscape for the vortex configurations, and discuss how similar hysteresis will appear in experiments. This landscape reflects the competition between vortex-vortex interactions and pinning to the optical lattice. In section II we describe our mean-field ansatz and numerical self-consistency routine. In section III we show how vortex configurations evolve from commensurate lattices to incommensurate ring-like structures as the rotation rate is varied. In section IV we present the hysteretic evolution of vortex configurations on spin-up and then spin-down. In section V we simulate the results of time-of-flight imaging of these systems, and in section VI we summarize our results.

Previous work, focusing on the multi-band weak lattice limit, found vortex structures similar to those we see in our tight binding model [8, 27], but did not report on how these structures evolved as parameters were adiabatically varied. Our discussion of the expansion of the rotating cloud initially in the single-band tight-binding regime is also novel.

6.2 Calculation

In the reference frame of the rotating optical lattice, our system is described by the rotating Bose-Hubbard hamiltonian [9, 25]:

$$\hat{H} = -\sum_{\langle i,j\rangle}\left(t_{ij}\hat{a}_i^\dagger\hat{a}_j + h.c.\right) + \sum_i\left(\frac{U}{2}\hat{n}_i\left(\hat{n}_i - 1\right) - \mu_i\hat{n}_i\right) \tag{6.1}$$

where $t_{ij} = t\exp\left[i\int_{\vec{r}_j}^{\vec{r}_i} d\vec{r}\cdot\vec{A}(\vec{r})\right]$ is the hopping matrix element from site j to site i. The rotation vector potential, which gives rise to the Coriolis effect, is $\vec{A}(\vec{r}) = (m/\hbar)\left(\vec{\Omega}\times\vec{r}\right) = \pi\nu\left(x\hat{y} - y\hat{x}\right)$, where ν is the number of circulation quanta

per optical-lattice site. The local chemical potential $\mu_i = \mu_0 - m\left(\omega^2 - \Omega^2\right) r_i^2/2$ includes the centripetal potential. In these expressions, μ_0 is the central chemical potential, ω is the trapping frequency, Ω is the rotation speed, $\vec{\boldsymbol{r}}_i$ is the position of site i, m is the atomic mass, $\hat{a}_i^\dagger$ ($\hat{a}_i$) is a bosonic creation (annihilation) operator, $\hat{n}_i = \hat{a}_i^\dagger \hat{a}_i$ is the particle number operator for site i, and U is the particle-particle interaction strength. The connection between these parameters and the laser intensities are given by Jaksch et al. [9]. Here, and in the rest of the paper, we use units where the lattice spacing is unity, and we operate exclusively at zero temperature.

Both the superfluid and Mott insulator are well described by a spatially inhomogeneous Gutzwiller product *ansatz* [9],

$$|\Psi_{GW}\rangle = \prod_{i=1}^{M} \left(\sum_n f_n^i |n\rangle_i \right), \tag{6.2}$$

where i is the site index, M is the total number of sites, $|n\rangle_i$ is the n-particle occupation-number state at site i, and f_n^i is the corresponding complex amplitude, with $\sum_n |f_n^i|^2 = 1$. This ansatz is more general than the more standard mean-field approximation described by the lattice Gross-Pitaevskii equation. In the limit where the latter works well, the two theories agree. The Gutzwiller ansatz has been used extensively to understand experimental results [12, 52, 53], and is well suited for studying the vortex physics that we consider here.

Using equation (6.2) as a variational *ansatz*, we minimize the energy with respect to the $\{f_n^i\}$. We then extract the density $\rho_i = \sum_n n |f_n^i|^2$ and the condensate order parameter $\alpha_i = \langle \hat{a}_i \rangle = \sum_n \sqrt{n} \left(f_{n-1}^i \right)^* f_n^i$ at each site. The condensate density $\rho_i^c = |\langle \hat{a}_i \rangle|^2$ is equal to the superfluid density in this model, and is generally not equal to the density.

We use an iterative algorithm to determine the $\{f_n^i\}$ which (locally) minimize

the energy. We use a square region with L sites per side with hard boundary conditions. We find that we must take L much larger than the effective trap radius so that our solutions do not depend on those boundaries. Typically we use $40 \leq L \leq 90$. We calculate $\langle \hat{H}_{RBH} \rangle$ using equation (6.2). Minimizing $\langle \hat{H}_{RBH} \rangle$ with respect to f_n^{i*} with the constraint $\sum_n |f_n^i|^2 - 1 = 0$ gives L^2 nonlinear eigenvalue equations, one for each site,

$$-t \sum_{k,\,\text{nn of } j} \left(\langle \hat{a}_k \rangle \sqrt{m} f_{m-1}^j R_{jk} + \langle \hat{a}_k^\dagger \rangle \sqrt{m+1} f_{m+1}^j R_{kj} \right) + \left(\frac{U}{2} m^2 - \left(\mu(r) + \frac{U}{2} \right) m + \lambda_j \right) f_m^j = 0 \,, \tag{6.3}$$

where the sum is over all nearest neighbors of site j, m is the particle-number index, λ_j is a Lagrange multiplier, and $R_{jk} = \exp\left[i \int_{\vec{r}_k}^{\vec{r}_j} d\vec{r} \cdot \vec{A}(\vec{r}) \right]$, with $i = \sqrt{-1}$. We iteratively solve these equations: first choosing a trial order-parameter field $\left\{ \alpha_j^{(0)} \right\}$, where $\alpha_j = \langle \hat{a}_j \rangle$; then updating it by $\alpha_j^{(p)} = \sum_n \sqrt{n} f_{n-1}^{j*} \left(\left\{ \alpha_j^{(p-1)} \right\} \right) f_n^j \left(\left\{ \alpha_j^{(p-1)} \right\} \right)$, where p is the iteration index. Similar calculations were performed by Scarola and Das Sarma [54] to analyze the case where the single-particle Mott state is surrounded by a rotating superfluid ring. In the uniform case this algorithm has been used by Wu et. al. [25] as well as Goldbaum and Mueller [46] and Oktel et. al. [40, 41].

Since equation (6.3) is highly nonlinear, we find that the solution that this iterative algorithm converges to is sensitive to the initial state we use. This feature allows us to see the hysteretic effects described in the text. Experiments will see similar hysteresis, but the precise details will differ from our calculations (for example the critical frequencies for vortex entry and egress will be somewhat modified).

We systematically explore the phase space, varying the parameters in the hamiltonian. We simulate clouds with diameter from 30-60 sites, comparable

to the sizes studied in experiments [52, 53]. For the largest simulations we impose four-fold rotational symmetry, but introduce no constraints in the smaller simulations.

6.3 Commensurability and Pinning

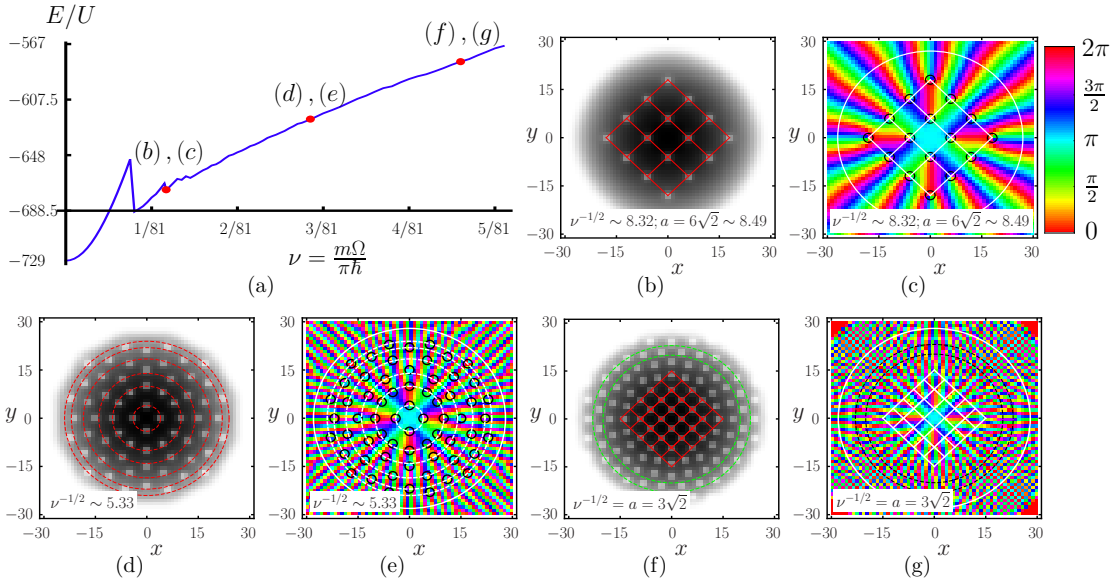

Figure 6.1: **Adiabatic spin-up**. Properties of cloud during adiabatic spin-up with parameters ($t/U = 0.2$, $\mu_0/U = 0.3$, $R_{TF} = 15$). (a) Energy vs rotation rate. Sharp drops indicate vortex formation. Energy scaled by on-site interaction parameter U, and rotation rate quoted as ν, the number of circulation quanta per optical-lattice site. (b), (d), (f) Superfluid density profile at parameters labeled in (a). Light-to-dark shading corresponds to low-to-high density, and position is measured in lattice spacing. Light spots correspond to vortex cores. Red and green lines are guides to the eye. (c), (e), (g) Superfluid phase represented by Hue. Solid white circle denotes edge of cloud. Dashed lines are guides to the eye. Black circles denote vortex locations. In (b), (c) and (f), (g) rotation speed should favor a commensurate square vortex lattice rotated by $\pi/4$ from the optical lattice axes. (d), (e) represents an incommensurate rotation speed.

We find a great variety of vortex patterns, including those resembling square vortex lattices. These are most stable at the rotation rates where they are commensurate with the underlying optical lattice. Commensurate Bravais lattices exist when $1/\nu$ is an integer, and commensurate square lattices when $\nu = 1/(n^2 + m^2)$, for integral n and m [8, 27, 28]. Which vortex patterns appear in a simulation, or in an experiment [55], depends on how the system is prepared. This hysteresis occurs because the energy landscape has many deep gorges with near-degenerate energies, separated by high barriers.

To illustrate this energy landscape, we fix $t/U = 0.2$ and $\mu_0/U = 0.3$, and study how the energy evolves as we vary the rotation speed. First, starting with the non-rotating ground state, we sequentially increase the rotation speed, using the previous wavefunction as a seed for our iterative algorithm. We adjust ω as we increase Ω so that the cloud size, related to the Thomas-Fermi radius, $R_{TF} = \sqrt{\frac{2\mu_0}{m(\omega^2-\Omega^2)}}$, remains effectively fixed. The energy as a function of rotation speed, shown in Figure 6.1(a), has a series of sharp drops, corresponding to the entry of one or more vortices from outside of the cloud. At these rotation speeds the system jumps from one local minimum of the energy landscape to another.

Figure 6.1 (b)-(g) shows the superfluid density and phases associated with the vortex patterns found during this *adiabatic* increase in rotation speed, where we impose four-fold rotation symmetry about the trap center. Subfigures (b) and (c) show a regular square vortex lattice seen near the commensurate $\nu = 1/(2\times6^2)$. Subfigures (d) and (e) show the vortex configuration at $\nu \sim 1/(2\times3.76^2)$ which is intermediate between the commensurate values $\nu = 1/(2 \times 3^2)$ and $\nu = 1/(2 \times 4^2)$. Rather than forming a square pattern, the vortex configuration appears to be made of concentric rings. Such ring-like structures also occur for

superfluids rotating in hard-walled cylindrical containers [79], where boundaries play an important role. Despite this analogy, it appears that in the harmonic trap these circular configurations are *not* a consequence of the circular boundary. When we simulate an elliptical trap, we still find roughly circular vortex configurations. As one increases ν towards $\nu \sim 1/(2 \times 3^2)$, a domain containing a square vortex lattice begins to grow in the center of the trap. As seen in Subfigures (f) and (g), at commensurability the domain only occupies part of the cloud, even though one would expect that a uniform square lattice would be energetically favorable. The inability of the system to find the expected lowest energy configuration during an adiabatic spin-up is indicative of the complicated energy landscape.

The patterns that we find are largely determined by the symmetry of the instabilities by which vortices enter the system. For example, even when we do not impose a four-fold symmetry constraint this adiabatic spin-up approach never produces square vortex lattices oriented at an angle other than $\pi/4$ with respect to the optical lattice axes. On the other hand, we readily produce other commensurate vortex lattices by choosing the appropriate rotation speed and seeding our iterative algorithm with the corresponding phase pattern. We have verified this approach with square vortex lattices oriented at various angles with respect to the optical lattice, taking $\nu^{-1/2} = \{4, 5, 6, 7, 8, 9, 10\}$, $(5\nu)^{-1/2} = \{2, 3, 4, 5, 6\}$ and $(10\nu)^{-1/2} = \{2, 3, 4\}$.

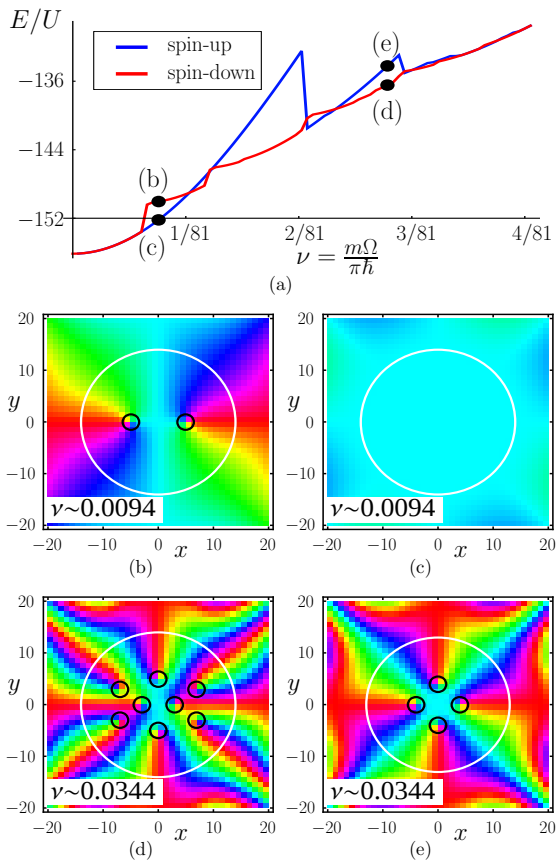

Figure 6.2: **Hysteresis**. (a) Energy versus rotation rate during increase (blue line) and decrease (red line) of ν. Energy steps in the blue (red) curve correspond to nucleation (expulsion) of vortices. (b)-(e) Order parameter complex phase for parameters labeled in (a). Black circles are drawn around vortex cores, and white circles indicate the approximate extent of the gas.

6.4 Hysteresis

We further explore the history dependance of the vortex configurations by increasing, then decreasing Ω. We do not impose a four-fold symmetry constraint, but take a smaller system with $R_{TF} = 7$. At any given Ω, the energy shown in Figure 6.2 (a) depends on the system's history. The increasing(blue)/decreasing(red) rotation curve has sharp energy drops signaling the introduction/ejection of vortices to/from the system. The energy drops occur

at different Ω for spin-up and spin-down, indicating that the critical rotation speed for a vortex to enter or exit the system is different. Generically, there are more vortices in the system on spin-down than on spin-up. Depending on Ω, one may find a lower energy state by increasing (subfigs. (b) and (c)) or by decreasing (subfigs. (d) and (e)) the rotation rate. As demonstrated by subfigs. (d) and (e), vortex configurations produced during spin-up typically have the four-fold rotational symmetry of the optical lattice, while the vortex configurations calculated during spin-down are more likely to break this symmetry. An experiment will display the same qualitative features, but slightly different vortex configurations.

When Ω is changed more rapidly (*i.e.*, the step-size is increased), we find more symmetry broken states than when we use small steps. The energy differences between the symmetric and asymmetric states are extremely small, so the energies shown in Figure 6.2 are robust over a large range of sweep rates.

6.5 Time-of-flight imaging

In a previous paper [66] we proposed detecting vortices in optical lattice systems through time-of-flight imaging [12, 32], where at time $\bar{t} = 0$ one turns off the lattice and the harmonic trap, letting the cloud expand. After some fixed time $\bar{t}$ one then produces an absorption image of the cloud using a resonant laser beam. In a weakly-interacting gas, the density profile is related to the momentum distribution of the gas. Here we elaborate on this argument, and show how the vortices will be observable in the time-of-flight (TOF) images. This complements other methods for extracting vortex properties, such as Bragg spec-

troscopy [80]. Recently Palmer, Klein, and Jaksch investigated time-of-flight expansion in the fractional quantum Hall limit [50].

We present a simple model where we neglect interactions during the time-of-flight. This approximation is quite good. First, the interactions between atoms from different sites can generically be neglected: by the time atoms from different sites overlap, the density is so low that they have negligable chance of scattering. Second, in the single-band tight-binding limit the kinetic energy from the zero-point motion of atoms on a single site should exceed the interaction energy, meaning that the trajectory of the atoms will only be slightly perturbed by the interactions. If one did include the effects of interactions during the expansion one would see a slight blurring of the interference patterns. This blurring comes from two effects: (1) atoms from sites with higher occupation will be moving faster (the interaction energy is converted into kinetic energy), and (2) the interactions introduce phase shifts which depend on atom number.

Within our approximation, calculating the density of the expanding cloud reduces to a series of single-particle problems. Taking the initial wavefunction to be given by equation (6.2), after time $\bar{t}$ the wavefunction will be

$$|\psi(\bar{t})\rangle = \prod_{i=1}^{M} \left(\sum_n f_n^i \frac{\left[\hat{a}_i^\dagger(\bar{t})\right]^n}{\sqrt{n!}} \right) |\text{vac}\rangle, \tag{6.4}$$

where $\hat{a}_i(0)$ is the operator which annihilates the single-particle state in site i of the lattice. This operator evolves via the Heisenberg equation of motion, $i\hbar\partial_{\bar{t}}\hat{a}_j(\bar{t}) = \left[\hat{a}_j(\bar{t}), \hat{H}_{\text{free}}\right]$ where $\hat{H}_{\text{free}}$ is the Hamiltonian for non-interacting particles. This is equivalent to evolving the single-particle state annihilated by $\hat{a}_i(\bar{t})$ via the free Schrodinger equation.

For this analysis we use the notation that $\vec{r}$ is a vector in the $x-y$ plane, and

z represents the coordinate in the perpendicular direction. We take the initial (Wannier) state at each site, $\phi_i(\vec{r}, z)$, to be gaussian:

$$\phi_i(\vec{r}, z) = \frac{1}{(\pi\lambda^2)^{1/2}} \frac{1}{\left(\pi\lambda_\perp^2\right)^{1/4}} \exp\left[-\frac{(\vec{r} - \vec{r}_i)^2}{2\lambda^2} - \frac{z^2}{2\lambda_\perp^2}\right], \tag{6.5}$$

where $\lambda = \sqrt{\frac{\hbar}{m\omega_{osc}}}$, and $\lambda_\perp = \sqrt{\frac{\hbar}{m\omega_\perp}}$ with ω_{osc} and $\omega_\perp$ being the small oscillation frequencies for each well. In the geometry we envision, $\omega_\perp \gg \omega_{osc}$. The wavefunctions at a time $\bar{t}$ after release of the trap are calculated by Fourier transforming $\phi_i(\vec{r}, z)$ to momentum space, then time evolving under $\hat{H}_{\text{free}}$ and finally Fourier transforming back to position space to arrive at $\phi_i\left(\vec{r}, z, \bar{t}\right) = \phi_i\left(\vec{r}, \bar{t}\right) f(z, \bar{t})$, where the only thing we need to know about the transverse wavefunction $f(z, \bar{t})$ is that it is normalized so $\int |f(z, \bar{t})|^2 dz = 1$. The in-plane wavefunction is

$$\phi_i\left(\vec{r}, \bar{t}\right) = \left(\frac{\lambda^2}{\pi\left(\lambda^2 + i\hbar\bar{t}/m\right)^2}\right)^{1/2} \exp\left[-\frac{(\vec{r} - \vec{\mathbf{r}}_\mathbf{i})^2}{2\left(\lambda^2 + i\hbar\bar{t}/m\right)}\right], \tag{6.6}$$

and the column density of the expanding cloud is then

$$n\left(\vec{r}, \bar{t}\right) = \int \langle\psi(\bar{t})|\hat{\psi}^\dagger(\vec{r}, z)\,\hat{\psi}(\vec{r}, z)\,|\psi(\bar{t})\rangle\, dz = \sum_{i=1}^{M} \left[n_i - n_{c,i}\right] |\phi_i\left(\vec{r}, \bar{t}\right)|^2 + \left|\sum_{i=1}^{M} \alpha_i \phi_i\left(\vec{r}, \bar{t}\right)\right|^2, \tag{6.7}$$

where n_i ($n_{c,i}$) is the number of atoms (condensed atoms) initially at site i, and $\hat{\psi}(\vec{r}, z)$ is the bosonic field operator annihilating an atom at position $(\vec{r}, z)$.

In the long-time limit where the expanded cloud is much larger than the initial cloud (i.e., $D_{\bar{t}} = \hbar\bar{t}/m\lambda \gg R_{TF}$), this expression further simplifies, and one has

$$n(\vec{r}, \bar{t}) = \rho(\vec{r}, \bar{t})\left[(N - N_c) + |\Lambda(\vec{r}, \bar{t})|^2\right] \tag{6.8}$$

$$\rho(\vec{r}, \bar{t}) = \left(\pi D_{\bar{t}}^2\right)^{-1} e^{-r^2/D_{\bar{t}}^2} \tag{6.9}$$

$$\Lambda(\vec{r}, \bar{t}) = \sum_j \alpha_j e^{-i\mathbf{r}\cdot\mathbf{r}_j/D_{\bar{t}}\lambda}, \tag{6.10}$$

where N and N_c are the total number of particles and condensed particles, respectively. The envelope, $\rho(\vec{r}, \bar{t})$, is a Gaussian, reflecting the Gaussian shape of the Wannier state. The incoherent contribution $(N - N_c)\rho(\vec{r}, \bar{t})$ has no additional structure. This is a consequence of the Gutzwiller approximation, which neglects short-range correlations. Adding these correlations would modify the shape of the background, but it will remain smooth.

The interference term has the structure of the envelope $\rho(\vec{r}, \bar{t})$ multiplied by the modulus squared of the discrete Fourier transform of the superfluid order parameter. The discrete Fourier transform can be constructed by taking the continuous Fourier transform of the product of a square array of delta-functions, and a smooth function which interpolates the superfluid order parameter. The resulting convolution produces of a series of Bragg peaks, each of which have an identical internal structure which is the Fourier transform of the interpolated superfluid order parameter. The vortices will be visible in the structure of these peaks.

Vortices in real-space lead to vortices in reciprocal space. This result is clearest for "lowest Landau level" vortex lattices [81] which are expressible as an analytic function of $\overline{z} = x + iy$ multiplied by a Gaussian of the form $e^{-|\overline{z}|^2/w^2}$, where w is a length scale which sets the cloud size. Aside from a scale factor and a rotation, the continuous Fourier transform of such a function is identical to the original. More generally, the topological charge associated with the total number of vortices is conserved in the expansion process.

Figure 6.3 displays simulated expansion images corresponding to the initial square vortex-lattice state shown in Subfigures 6.1 (a) and (b), where $t/U = 0.2$. In these images, lighter colors correspond to smaller column densities. Using

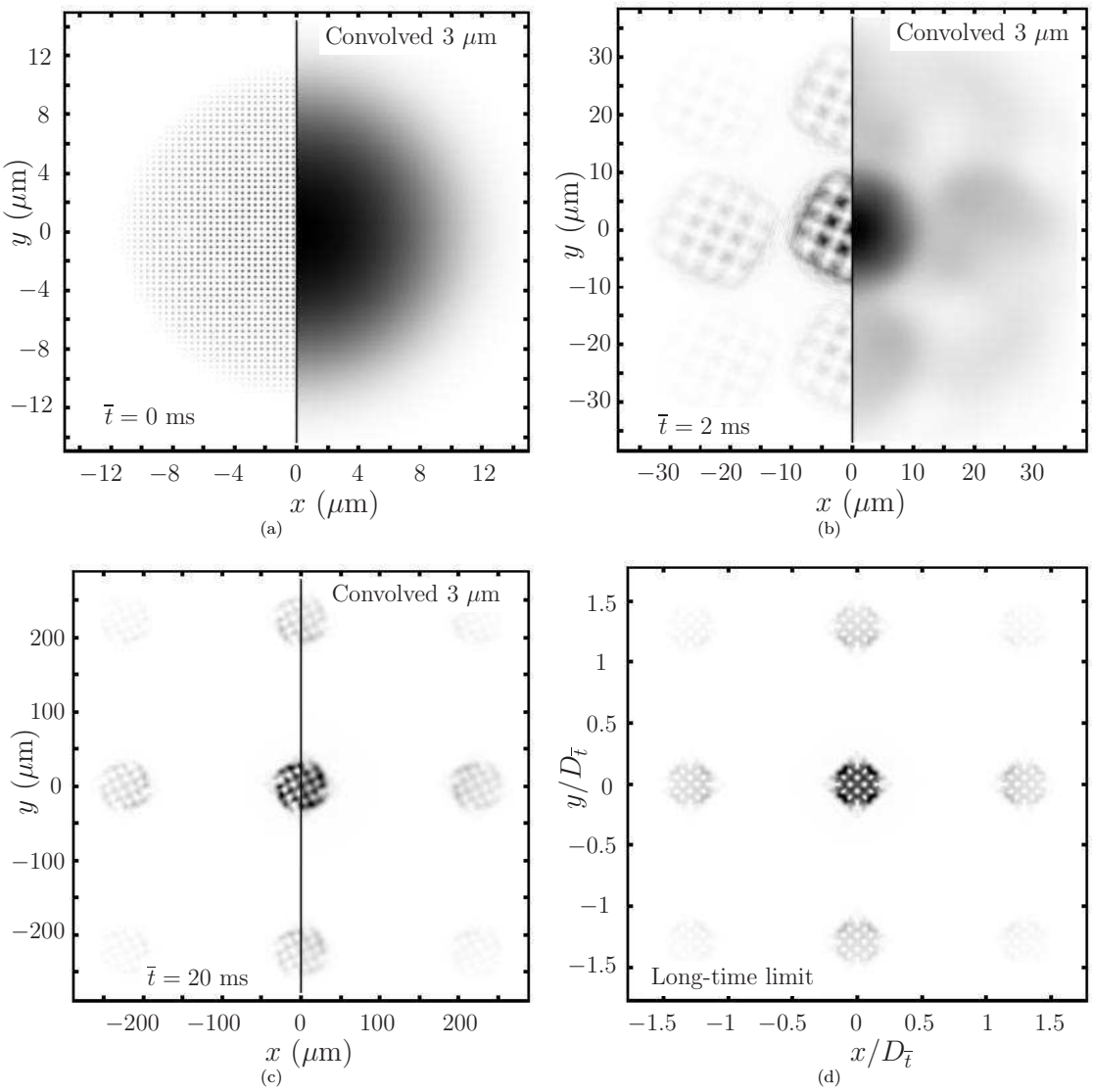

Figure 6.3: **Simulation of column density seen in time-of flight absorption images**. Darker shading corresponds to higher column density. The initial state corresponds to the the 4x4 square vortex lattice pictured in Subfigures 6.1(b),(c). (a)-(c) 0, 3, and 20 ms expansion. Left: column density profile calculated using equation (6.7); Right: column density convolved with a 3 μm wide Gaussian distribution to represent the finite resolution of a typical imaging system. (d) long-time scaling limit, where $D_{\bar{t}} = \hbar\bar{t}/m\lambda \gg R_{TF}$.

rubidium-87 atoms on an optical lattice characterized by $d = 410$ nm and a hard axis lattice depth of 30 E_R, which are the experimental values in ref. [13], we find that $V_0 = 5.7\ E_R$, which gives $\lambda = 84$ nm. Subfigures 6.3 (a)-(c) display absorption images: the left-hand side ($x < 0$) is the column density calculated with equation (6.7), while the right-hand side ($x > 0$) shows this density convolved with a 3 μm wide Gaussian, representing the blurring from typical optics. Subfigure 6.3(d) displays the long-time expansion limit column density calculated using equation (6.10), which only depends on the $\{f_n^i\}$'s and the ratio (λ/d).

Subfigure 6.3(a) shows the *in situ* (t=0 ms) column density. At this stage the Wannier functions are tightly peaked about the lattice sites, resulting in a series of sharp density bumps. The heights of these bumps are slightly modulated due to the square vortex lattice: near the cores of the vortices there is a slight depletion of the density. Due to the small vortex size, none of this structure is seen once the image is convolved with the Gaussian. This demonstrates that a typical imaging setup would be unable to resolve the vortices. Subfigure 6.3(b) shows the abosrption image after 2 ms time-of-flight. Several very broad Bragg peaks have developed, each showing a number of low density regions reflecting the square vortex lattice. Again, the vortex structure is lost upon convolution. Subfigure 6.3(c) shows an absorption image after 20 ms TOF where, even after convolution, the Fourier transform of the initial vortex pattern is clearly visible in each of the Bragg peaks. In their investigation of atoms in non-rotating optical lattices, Spielman et. al. [13] allowed their atoms to expand for 20.1 ms before imaging. Subfigure 6.3(d) is a column density calculated in the long-time limit using equation (6.10). Aside from an overal scaling, and a slight rotation of the structure within each Bragg peak, the image after 20 ms is almost identical to the image seen in the long-time limit.

6.6 Summary

We have studied the vortex structures in a harmonically trapped Bose gas in the presence of a rotating optical lattice. We discussed the hysteretic evolution of the vortex structures as the rotation rate is varied. This hysteresis is a signature of the complicated energy landscape. We observed a tendency for the system to find regular lattices configurations when the vortex density is commensurate with the site density. At incommensurate vortex densities we instead see a circular vortex pattern which is robust against changing the aspect ratio of the trap. Finally we analyzed the time-of-flight expansion of one of these condensates. We find that the vortex patterns are readily observed in the structure of the resulting Bragg peaks.

BIBLIOGRAPHY

[1] I. Bloch, J. Dalibard, and W. Zwerger, Rev. Mod. Phys. **80**, 885 (2008).

[2] D. Jaksch and P. Zoller, Ann. Phys. (NY) **315**, 52 (2005).

[3] J. Dunningham, K. Burnett, and W. D. Phillips, Phil. Trans. R. Soc. A **363**, 2165 (2005).

[4] D. Jaksch, H.-J. Briegel, J. I. Cirac, C. W. Gardiner, and P. Zoller, Phys. Rev. Lett. **82**, 1975 (1999).

[5] DARPA – Optical Lattice Emulator project: http://www.darpa.mil/dso/thrusts/physci/funphys/ole/index.htm.

[6] M. Tsubota, K. Kasamatsu, and M. Ueda, Phys. Rev. A **65**, 023603 (2002).

[7] K. Kasamatsu, M. Tsubota, and M. Ueda, Phys. Rev. A **66**, 053606 (2002).

[8] H. Pu, L. O. Baksmaty, S. Yi, and N. P. Bigelow, Phys. Rev. Lett. **94**, 190401 (2005).

[9] D. Jaksch, C. Bruder, J. I. Cirac, C. W. Gardiner, and P. Zoller, Phys. Rev. Lett. **81**, 3108 (1998).

[10] C. J. Pethick and H. Smith, *Bose-Einstein Condensation in Dilute Gases* (Cambridge University Press, Cambridge, UK, 2002).

[11] P. B. Blakie and C. W. Clark, J. Phys. B **37**, 1391 (2004).

[12] M. Greiner, O. Mandel, T. Esslinger, T. W. Hansch, and I. Bloch, Nature **415**, 39 (2002).

[13] I. B. Spielman, W. D. Phillips, and J. V. Porto, Phys. Rev. Lett. **100**, 120402 (2008).

[14] N. W. Ashcroft and N. D. Mermin, *Solid State Physics* (Saunders College Publishing, 1976).

[15] V. A. Kashurnikov, N. V. Prokof'ev, and B. V. Svistunov, Phys. Rev. A **66**, 031601 (2002).

[16] D. J. Griffiths, *Introduction to Quantum Mechanics* (Prentice Hall (NJ), 1995).

[17] G. B. Arfken and H. J. Weber, *Mathematical Methods for Physicists*, 5th edition ed. (Academic Press, 2000).

[18] A. L. Fetter, Annals of Physics **70**, 67 (1972).

[19] L. Pitaevskii and S. Stringari, *Bose-Einstein Condensation* (Oxford University Press, Oxford, UK, 2003).

[20] P. Nozieres and D. Pines*The Theory of Quantum Liquids* Vol. 2 (Perseus Books, Cambridge, MA, 1999).

[21] B. D. Claude Cohen-Tannoudji and F. Laloe*Quantum Mechanics* Vol. 1 (Wiley-Interscience, New York, 1977).

[22] D. B. M. Dickerscheid, D. van Oosten, P. J. H. Denteneer, and H. T. C. Stoof, Phys. Rev. A **68**, 043623 (2003).

[23] M. P. A. Fisher, P. B. Weichman, G. Grinstein, and D. S. Fisher, Phys. Rev. B **40**, 546 (1989).

[24] M. Plischke and B. Bergersen, *Equilibrium Statistical Physics*, 2nd ed. (World Scientific, 1994).

[25] C. Wu, H. dong Chen, J. piang Hu, and S.-C. Zhang, Phys. Rev. A **69**, 043609 (2004).

[26] D. R. Hofstadter, Phys. Rev. B **14**, 2239 (1976).

[27] J. W. Reijnders and R. A. Duine, Phys. Rev. Lett. **93**, 060401 (2004).

[28] S. Tung, V. Schweikhard, and E. A. Cornell, Phys. Rev. Lett. **97**, 240402 (2006).

[29] J. Zak, Phys. Rev. **134**, A1602 (1964).

[30] J. Zak, Phys. Rev. **134**, A1607 (1964).

[31] D. J. Thouless, M. Kohmoto, M. P. Nightingale, and M. den Nijs, Phys. Rev. Lett. **49**, 405 (1982).

[32] K. W. Madison, F. Chevy, W. Wohlleben, and J. Dalibard, Phys. Rev. Lett. **84**, 806 (2000).

[33] J. R. Abo-Shaeer, C. Raman, J. M. Vogels, and W. Ketterle, Science **292**, 476 (2001).

[34] P. Engels, I. Coddington, P. C. Haljan, and E. A. Cornell, Phys. Rev. Lett. **89**, 100403 (2002).

[35] V. Schweikhard, I. Coddington, P. Engels, V. P. Mogendorff, and E. A. Cornell, Phys. Rev. Lett. **92**, 040404 (2004).

[36] N. K. Wilkin and J. M. F. Gunn, Phys. Rev. Lett. **84**, 6 (2000).

[37] N. R. Cooper, N. K. Wilkin, and J. M. F. Gunn, Phys. Rev. Lett. **87**, 120405 (2001).

[38] J. W. Reijnders and R. A. Duine, Phys. Rev. A **71**, 063607 (2005).

[39] Z. Hadzibabic, P. Kruger, M. Cheneau, B. Battelier, and J. Dalibard, Nature **441**, 1118 (2006).

[40] M. O. Oktel, M. Nita, and B. Tanatar, Phys. Rev. B **75**, 045133 (2007).

[41] R. O. Umucalilar and M. O. Oktel, Phys. Rev. A **76**, 055601 (2007).

[42] B. Capogrosso-Sansone, N. V. Prokof'ev, and B. V. Svistunov, Phys. Rev. B **75**, 134302 (2007).

[43] M. P. aand R. Fazio, M. Tosi, J. Sinova, and A. MacDonald, Laser Physics **14**, 603 (2004).

[44] M. Polini, R. Fazio, A. H. MacDonald, and M. P. Tosi, Phys. Rev. Lett. **95**, 010401 (2005).

[45] S. Viefers, J. Phys.: Cond. Matt. **20**, 123202 (14pp) (2008).

[46] D. S. Goldbaum and E. J. Mueller, Phys. Rev. A **77**, 033629 (2008).

[47] D. Jaksch and P. Zoller, New J. Phys. **5**, 56 (2003).

[48] E. J. Mueller, Phys. Rev. A **70**, 041603(R) (2004).

[49] A. S. Sorensen, E. Demler, and M. D. Lukin, Phys. Rev. Lett. **94**, 086803 (2005).

[50] R. N. Palmer, A. Klein, and D. Jaksch, Phys. Rev. A **78**, 013609 (2008).

[51] J. K. Freericks and H. Monien, Phys. Rev. B **53**, 2691 (1996).

[52] S. Folling, A. Widera, T. Muller, F. Gerbier, and I. Bloch, Phys. Rev. Lett. **97**, 060403 (2006).

[53] G. K. Campbell *et al.*, Science **313**, 649 (2006).

[54] V. W. Scarola and S. D. Sarma, Phys. Rev. Lett. **98**, 210403 (2007).

[55] K. W. Madison, F. Chevy, V. Bretin, and J. Dalibard, Phys. Rev. Lett. **86**, 4443 (2001).

[56] F. London, *Superfluids* (Wiley, New York, 1990).

[57] A. J. Leggett, in *Low Temperature Physics*, edited by M. J. R. Hoch and R. H. Lemmer (Springer Verlag, Berlin 1991), Vol. 394, pp. 1–92.

[58] D. S. Rokhsar, Dilute bose gas in a torus: vortices and persistent currents, arXiv:cond-mat/9709212v1.

[59] E. J. Mueller, P. M. Goldbart, and Y. Lyanda-Geller, Phys. Rev. A **57**, R1505 (1998).

[60] C. Ryu *et al.*, Phys. Rev. Lett. **99**, 260401 (2007).

[61] A. D. Jackson, G. M. Kavoulakis, and E. Lundh, Phys. Rev. A **69**, 053619 (2004).

[62] A. Aftalion and I. Danaila, Phys. Rev. A **69**, 033608 (2004).

[63] A. D. Jackson and G. M. Kavoulakis, Phys. Rev. A **70**, 023601 (2004).

[64] S. Bargi, G. M. Kavoulakis, and S. M. Reimann, Phys. Rev. A **73**, 033613 (2006).

[65] F. S. Cataliotti *et al.*, Science **293**, 843 (2001).

[66] D. S. Goldbaum and E. J. Mueller, Vortices near the Mott phase of a trapped Bose-Einstein condensate, arXiv:0808.1548.

[67] R. Bhat, M. Kramer, J. Cooper, and M. J. Holland, Phys. Rev. A **76**, 043601 (2007).

[68] M. Hafezi, A. S. Sorensen, E. Demler, and M. D. Lukin, Phys. Rev. A **76**, 023613 (2007).

[69] G. Baym, C. J. Pethick, S. A. Gifford, and G. Watanabe, Phys. Rev. A **75**, 013602 (2007).

[70] G. Watanabe, G. Baym, and C. J. Pethick, Phys. Rev. Lett. **93**, 190401 (2004).

[71] G. Baym and C. J. Pethick, Phys. Rev. A **69**, 043619 (2004).

[72] A. Aftalion, X. Blanc, and J. Dalibard, Phys. Rev. A **71**, 023611 (2005).

[73] I. Coddington *et al.*, Phys. Rev. A **70**, 063607 (2004).

[74] D. E. Sheehy and L. Radzihovsky, Phys. Rev. A **70**, 063620 (2004).

[75] D. E. Sheehy and L. Radzihovsky, Phys. Rev. A **70**, 051602 (2004).

[76] K. Kasamatsu, J. Low Temp. Phys. **150**, 593 (2007).

[77] T. Sato, T. Ishiyama, and T. Nikuni, Phys. Rev. A **76**, 053628 (2007).

[78] R. A. Williams *et. al.*, Optics Express Vol. 16, 21, 16977-16983 (2008).

[79] L. J. Campbell and R. M. Ziff, Phys. Rev. B **20**, 1886 (1979).

[80] P. Vignolo, R. Fazio, and M. P. Tosi, Phys. Rev. A **76**, 023616 (2007).

[81] T.-L. Ho, Phys. Rev. Lett. **87**, 060403 (2001).